INNOVATIVE ANALYSIS TECHNIQUES FOR CANADIAN SCWR NEUTRONICS

INNOVATIVE ANALYSIS TECHNIQUES FOR CANADIAN SCWR NEUTRONICS

By

Jason R. Sharpe, B. Sc., M. Sc.

A Thesis

Submitted to the School of Graduate Studies

in Partial Fulfilment of the Requirements for the Degree

Doctor of Philosophy

McMaster University

DOCTOR OF PHILOSOPHY (2017) McMaster University

(Department of Engineering Physics) Hamilton, Ontario

TITLE: Innovative Analysis Techniques for Canadian SCWR Neutronics

AUTHOR: Jason R. Sharpe
B. Sc. (University of New Brunswick)
M. Sc. (Saint Mary's University)
Ph. D. Candidate (McMaster University)

SUPERVISOR: Professor Dr. Adriaan Buijs

NUMBER OF PAGES: xiv, 109

Abstract

Knowledge of the effects of nuclear data uncertainties and physics approximations is crucial for the development, design, operation, and accident mitigation, of nuclear power plants. A framework to create a simulated fuel bundle, based on sensitivities and similarities, has been developed. The methodology allows safe-to-handle fuel to be manufactured such that it mimics irradiated fuel and can be used to reduce simulation uncertainties and better predict an application's response. In this work, similarity values of $c_k = 0.967$, $E = 0.992$, and $G = 0.891$ were found between between the irradiated fuel, and non-irradiated simulated fuel. In addition, a set of ZED-2 experiments has been analyzed that are applicable to an SCWR nuclear data adjustment and simulation bias determination. This was shown through high sensitivity coverage of many important nuclides, however, a low completeness value of R=0.24 indicates the set of 39 experiments alone is not sufficient for an accurate bias determination. Lastly, a technique has been presented that reduces diffusion calculation errors through the use of novel and practical mean discontinuity factors. The discontinuity factors have shown to reduce maximum channel power errors by up to 6.7%, and reactivity errors by 2.6 mk, compared to conventional analysis techniques.

Acknowledgements

First and foremost, I'd like to thank my supervisor Dr. Adriaan Buijs. His hands-off but always present approach was fitting to drive me to complete this research and thesis. He is very knowledgeable about the topics of this research, but was always patient and would allow me to come to my own conclusions, which helped me grow as a researcher. In addition he allowed me to try things in a way I saw fit and was never too eager to push his opinions on me but offered advice whenever it was requested. His industry connections helped me to network throughout my years at McMaster which have so far proved invaluable. Also, I must thank him for the many hours he put into reminding me of the English language grammar rules. I will forever be thankful for his wisdom, his positivity, council, and guidance throughout my PhD.

I'd like to thank Dr. Jeremy Pencer for prompting the ideas which lead to my first journal article. Also for his continued support throughout my PhD despite his physical distance from McMaster. His thorough comments were always welcomed and we had many fruitful discussions which led to additional research publications and presentations.

I would sincerely like to send my gratitude to Dr. David Novog who always offered advice from a very practical point of view. His tough love and critical approach during committee meetings forced me to think long and hard about many important details to ensure I was doing things properly, and critically thinking about the problems at hand. His industrial experience was of great value to all of my research.

I would also like to offer my deepest gratitude to my good friend and colleague (hope-

fully future Dr.) Fred Salaun. We shared an office for four years and I can't even begin to guess how many hours we spent discussing each others work, helping to solve each others problems, where it was in the office, at conferences, over Skype, or over a beverage.

Finally, I would like to thank my parents, Anna and Clinton Sharpe. From an early age they always encouraged me to follow my dreams and constantly reminded me I was capable of anything. Without a doubt, it was their confidence in me along with their emotional and financial support that has enabled me to succeed in my educational career.

Contents

List of Figures

List of Tables

Acronyms

AECL	Atomic Energy of Canada Limited
BOC	Beginning-of-cycle
BNA	Burnable neutron absorber
BWR	Boiling water reactor
CANDU	Canadian Deuterium Uranium
CDF	Cumulative distribution function
CMFD	Coarse mesh finite difference
CNSC	Canadian Nuclear Safety Commission
CVR	Coolant void reactivity
DID	Defense-in-depth
ENDF	Evaluated nuclear data file
GET	General equivalence theory
GIF	Generation IV International Forum
GLLS	Generalized linear least squares
IAE	Institute of Applied Energy
HERC	High efficiency re-entrant flow channel
JEFF	Joint evaluated fission and fusion file
JENDL	Japanese evaluated nuclear data library

LHS	Left-hand side
MOC	Method of characteristics
NRCan	Natural Resources Canada
PWR	Pressurized water reactor
PDF	Probability distribution function
R&D	Research and development
RHS	Right-hand side
SAMS	Sensitivity Analysis Module for SCALE
SCM	Step characteristic method (also known as SM)
SCWR	Supercritical Water-cooled Reactor

Symbols

Different subfields of nuclear analysis were used in this thesis and at times symbol meanings overlapped. The context of the symbols should be clear from the descriptions.

Latin Characters

c_k	Similarity index (uncertainties)
f	Flux discontinuity factor
h	Nodal dimension [cm]
k_{eff}	Effective multiplication constant
l	Neutron path length [cm]
q	Neutron source term (Monte Carlo) [neutrons $\cdot$ cm^{-3} $\cdot$ s^{-1}]
r	Position/location [cm]
A	Area [m^2]
$\mathbf{C_{\Omega\Omega}}$	Covariance matrix (nuclear data)
$\mathbf{C_{mm}}$	Covariance matrix (experimental)
D	Diffusion Coefficient [cm]
E	Similarity index (sensitivities)
G	Coverage
G	Total number of energy groups
$\mathbf{J}$	Neutron current [neutrons $\cdot$ cm^{-2} $\cdot$ s^{-1}]

K	Number of neutron histories in a generation
L	Neutron loss operator [cm^{-1}]
N	Number of neutron histories
M	Neutron multiplication operator [cm^{-1}]
P	Pressure [Pa]
R	Completeness
S	Neutron source [$\mathrm{neutrons} \cdot \mathrm{cm}^{-3} \cdot \mathrm{s}^{-1}$]
S	Sensitivity
T	Temperature [k or °C]
V	Volume [cm^3]
Q	Neutron source term (Method of characteristics) [$\mathrm{neutrons} \cdot \mathrm{cm}^{-3} \cdot \mathrm{s}^{-1}$]

Greek Characters

α	Alpha particle (helium nucleus)
β	Simulation bias
η_{th}	Thermal efficiency
λ	Random number used in Monte Carlo methods
λ	$1/k_{\mathrm{eff}}$
$\bar{\mu}$	Average scattering cosine
ν	Number of neutrons emitted per fission
ρ	Reactivity $(1 - 1/k)$ [usually measured in mk]
σ	Microscopic cross section [b]
$\sigma_{\mathrm{stat.}}$	Statistical uncertainty
ϕ	Flux [$\mathrm{neutrons} \cdot \mathrm{cm}^{-2} \cdot \mathrm{s}^{-1}$]
$\phi^{\dagger}$	Adjoint flux [$\mathrm{neutrons} \cdot \mathrm{cm}^{-2} \cdot \mathrm{s}^{-1}$]
χ	Neutron fission spectrum [cm^{-1}]
ψ	Heterogeneous flux [$\mathrm{neutrons} \cdot \mathrm{cm}^{-2} \cdot \mathrm{s}^{-1}$]

Σ	Macroscopic cross section [cm^{-1}]
$\mathbf{\Omega}$	Neutron direction
Ω	Nuclear data (i.e., σ_f, ν, etc.)

Cross Section Labels

a	Absorption
s	Scatter
t	Total
tt	Total-transfer (also referred to as total-scatter)
tr	Transport

Other symbols

($\hat{}$)	Indicates a homogenized parameter
(-)	Indicates an averaged parameter
∇	Vector differential operator

Declaration of Academic Intent

Of the three journal articles included in this sandwich thesis, the author (J. Sharpe), was the main contributor to each article. Ideas for the papers and how they fell in line with the thesis goals were brewed between this thesis' author, his supervisor, Dr. Buijs, and his supervisory committee, which included Dr. Novog and Dr. Pencer. However, all background investigation, simulation preparation, simulation execution, analysis, and writing, were performed either solely or primarily by the author. A more detailed description of the author and co-authors' contributions is given below.

J. Sharpe, A. Buijs, and J. Pencer, "Methodology to design simulated irradiated fuel by maximizing integral indices (c_k, E, G)," *ASME J. Nucl. Eng. and Rad. Sci.*, vol. 2, no. 2, pp. 1-7, April 2016.

Research for this paper began in the fall of 2014 at McMaster University in collaboration with Sharpe (primary author), Buijs (co-author), Pencer (co-author) and Atomic Energy of Canada Limited. The general idea of the paper was decided upon by Sharpe, Buijs, Pencer. Simulation models were developed entirely by Sharpe. Furthermore, the model details were primarily chosen Sharpe, with guidance from the other two co-authors, then models were executed solely Sharpe. All analysis and writing was done solely Sharpe. The preliminary results of the work was completed by January of 2015, at which point a conference paper submission was made, by Sharpe, to the 8th International Symposium on Supercritical Water-cooled Reactors. Sharpe prepared the conference paper and presentation. The paper was modified, through guidance of the co-authors, then written and submitted, by Sharpe, to the Journal of Nuclear Engineering and Radiation Science in May of 2015.

Although all simulations, analysis, and writings were done by the author, the two co-authors contributed significantly through guidance, expertise, and discussion.

J. Sharpe, J. Atfield, J. Chow, L. Yaraskavitch, and A. Buijs, "Sensitivity analysis of ZED-2 experiments using (Pu,Th)O_2 fuel bundles to assess their applicability to the SCWR conceptual design," *CNL Nucl. Rev.*, vol. 5, no. 2, pp. 299-308, Dec. 2016.

In the spring of 2013, a meeting was held at McMaster University between Sharpe (primary author), Buijs (co-author), Pencer, and Colton, to acquire a non-disclosure agreement regarding a number of proprietary reports. Discussion in the summer 2015 between Sharpe and Atfield (co-author) marked the beginning of the research. All simulation models were prepared by Sharpe with heavily involved support from Atfield, Yaraskavitch (co-author), and Chow (co-author). Atfield, Yaraskavitch, and Chow provided value checks for erroneous experimental values, simulation model verification, and software support. Simulation execution, data collection, and analysis were solely performed by Sharpe, with guidance from Buijs. Sharpe wrote the entire manuscript, save the ZED-2 model generator paragraphs, which were written by Chow, the developer of the model generator. Both Atfield and Chow significantly contributed to editing the final manuscript, along with minor input from Buijs and Yaraskavitch. In the summer of 2016 the manuscript was submitted, by Sharpe, to CNL for managerial review, and later to Canadian Nuclear Laboratories Nuclear Review Journal for publication in August 2016.

Although all simulations, analysis, and writings (save some paragraphs) were done by the author, the co-authors lent significant guidance, suggestion, discussion, software support, model verification, and manuscript edits.

J. Sharpe and A. Buijs, "Practical environment-corrected discontinuity factors and homogenized parameters for improved PT-SCWR diffusion solutions," submitted for publication to *Ann. Nucl. Energy* on April 26, 2017 (Manuscript Number: ANUCENE-D-17-00318).

Research began and a literature review was performed by Sharpe (primary author) in the fall of 2016. During the preliminary work Buijs (co-author) was consulted at length many times regarding the usefulness of the results. A methodology and neutron diffusion code were developed by Sharpe. The developed code was tested, by Sharpe, against a National Research Council diffusion code. During late 2016 and early 2017, many simulations were prepared and executed by Sharpe to gather evidence to support the applicability of the method. In February 2017 the results were written-up in a draft, by Sharpe, which was reviewed by Buijs, and a few other colleagues (Pencer and Novog). The manuscript was submitted, by Sharpe, in April 2017.

The methodology and simulations models were developed by Sharpe. Furthermore, simulations were executed and analyzed, the manuscript was written, and submitted all by Sharpe. Significant discussion and guidance was offered by Buijs.

The paper has not yet been accepted, as of the writing of this thesis. It does, however, offer significant improvement over routine calculation methods used in conventional safety analysis and reactor research and development. Typically, improved prediction accuracy comes at the cost of additional computational time, however, this paper offers a practical and novel method to reduce errors, with minimal additional effort, and thus is expected to be well received by the journal and scientific community.

Chapter 1

Introduction

1.1 Background

A fundamental requirement of operating nuclear power stations is their continued safe operation, and in the event of an accident, their safe shutdown. In order to ensure this, a complete understanding of how reactors respond to any set of circumstances or perturbations, deemed important in safety assessments, is required.

Today, the conceptualization and design of new nuclear power reactors are greatly aided by the use of highly accurate neutron transport and thermalhydraulic simulation codes. The codes allow reactor physicists to examine the outcome of a wide range of circumstances, perturbations, and potential accident scenarios, before the nuclear power plant is ever built. However, despite the major progress in the capabilities of nuclear simulation codes, prediction errors, i.e. errors between simulation and experiment still exist.

Prediction errors arise from a number of things, for example, nuclear data uncertainties (i.e., cross sections), physics approximations, model approximations, and statistical uncertainties. These uncertainties and approximations present themselves in calculations at various steps in reactor physics analysis, which are shown in Figure 1.1. Fortunately

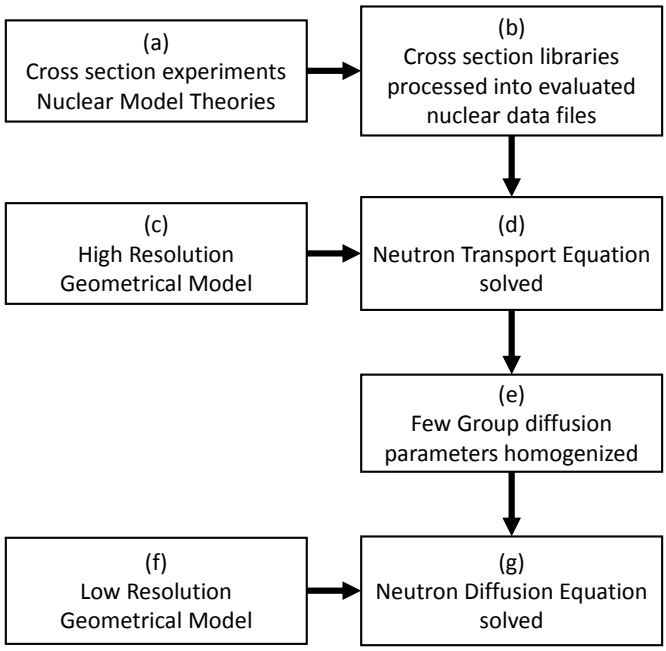

Figure 1.1: A typical reactor physics evaluation procedure.

many of the approximations, such as treating a circle as a polygon with 12 sides (boxes c and f) lead to small uncertainties, while many other uncertainty contributors may cancel out.

At each step, the following uncertainties or approximations, with some examples shown, affect the certainty of calculations:

(a) Measurement uncertainties, physics approximations.

(b) Physics approximations (resolved and unresolved resonance regions).

(c) Model approximations (measurements of nominal model parameters, modelling limitations imposed by simulation codes).

(d) Numerical approximations (rounding, angular discretization), physics approximations (isotropic scattering), statistical uncertainties (Monte Carlo methods).

(e) Numerical approximations (homogenization of cross sections by flux weighting).

(f) Numerical approximations (loss of physical detail).

(g) Physics approximations (absorption cross section is small relative to the scattering cross section), numerical approximations (few energy groups).

Nuclear data libraries have gone through a number of major iterations, and likewise, neutron transport codes have been significantly improved as computation power has increased and allowed for fewer mathematical approximations. Many of the mathematical/numerical approximations that are used in the neutronics codes can be considered as physics approximations. As an example, consider a numerical approximation that is often used in reactor physics codes [6]. The flux, $\phi(\mathbf{r})$, is expanded as a Taylor series about the origin and truncated after the second term [7]:

$$\phi(\mathbf{r}) = \phi(0) + \mathbf{r} \cdot \nabla\phi(0) + \frac{1}{2}[r^2\nabla^2\phi(0)] + \cdots \approx \phi(0) + \mathbf{r} \cdot \nabla\phi(0). \tag{1.1}$$

This approximation holds in many cases, however does not apply near strong neutron sources or absorbers when the flux varies rapidly with space. It is important to understand how approximations like this affect final calculations.

During the design and development of reactors, model approximations do not pose a serious issue in modern transport codes. This is mainly the case because of modern codes being able to deal with complex geometries with relative ease. Statistical uncertainties exist in Monte Carlo type neutron transport codes where many neutrons need to be simulated in order to see how a system behaves. This type of uncertainty still prevents Monte Carlo codes from being used as a rapid analysis tool, because the uncertainty is inversely proportional to the square of neutron histories simulated (e.g., $\sigma_{\text{stat.}} \propto 1/\sqrt{N}$). All the while, typical statistical uncertainties have also been reduced with access to faster processors, parallel computing, and larger banks of memory.

Having identified multiple types of uncertainties as being significant drawbacks and

challenges to accurate conventional neutronics analysis, this thesis presents three closely linked pieces of research that fill gaps in knowledge which lead to improved reactor neutronics simulations, specifically:

1. A new method has been proposed to generate simulated nuclear fuel which can be manufactured for experimentation in order to assess the fuel's neutronic characteristics and reduce nuclear data uncertainties (improve box *b* of Figure 1.1). Not only are improvements in simulation accuracy realized, but a new method to generate fuel for criticality experiments has been presented. If performed, the experiments can be used to further improve simulation accuracy based on modern sensitivity and uncertainty analysis frameworks,

2. A number of ZED-2 criticality experiments[1] have been assessed to determine their applicability to a new power reactor design, and if they are suitable to be used in a nuclear data uncertainty reduction (improve box *b* of Figure 1.1),

3. A practical modification has been made to conventional neutron diffusion that significantly improves its ability to accurately predict fuel channel powers (improve boxes *e* and *f* of Figure 1.1).

The improvements are illustrated by their effect on Canada's Super-Critical Water Reactor (SCWR) design.

Prior to presenting the research articles that are included in this thesis, the context of the work is presented. Many mathematical details have been omitted from the articles in an effort to maintain a concise writing style. Therefore, the theories used within the articles are introduced in the first few chapters of this thesis in greater detail, for improved clarity.

[1]This work was limited to ZED-2 experiments, however, a similar type of analysis can be carried out using OECD's International Criticality Safety Benchmark Evaluation Project's [8] database called DICE [9].

1.2 Motivation

The SCWR, which has been conceptually designed by Canadian Nuclear Laboratories (CNL), formally known as Atomic Energy of Canada Limited (AECL), is one of six generation IV nuclear power reactor type that are currently under development worldwide.

The need for nuclear power in the global energy portfolio is becoming increasingly obvious to governments, industries, companies, scientists and people around the world. Because of this, in January of 2000, a group of senior governmental representatives from nine countries met to form the Generation IV International Forum (GIF). Their goal was to facilitate the collaboration of many signatory nations to develop the next generation of nuclear power reactors. The following excerpt from the Charter of the Generation IV International Forum demonstrates their commitment to a clean, safe and efficient future:

> "Taking into account the expected increase in energy demand worldwide and the growing awareness about global warming, climate change issues and sustainable development, nuclear energy will be needed to meet future global energy demand. However, opportunities for building new nuclear energy systems will depend on their attractiveness and suitability in different countries and situations. Ongoing research and development (R&D) in the areas of economics, safety, waste and proliferation resistance is necessary in order to achieve nuclear energy's potential worldwide." [10]

GIF is composed of 14 signatories[2] which includes Australia, Argentina, Brazil, Canada, China, Euratom, France, Japan, Korea, Russia, South Africa, Switzerland, United Kingdom and the United States. Canada's contribution to GIF is through Natural Resources Canada (NRCan), in collaboration with the Institute of Applied Energy (IAE) of Japan, and many universities across Canada. The research is focused on the development of an SCWR.

[2] As of May 2017.

1.2.1 Canadian SCWR

The Canadian SCWR core concept is shown in Figure 1.2. The concept uses vertical fuel channels, as is used in boiling water reactor (BWR) and pressurized water reactor (PWR) designs, which allow quick and easy refueling. The cycle length between refueling operations is between 400 [11] to 425 days [12], depending on which type of beginning-of-cycle (BOC) reactivity suppression method, and refueling scheme, is selected. Batch refueling is considered an improvement over CANDU®'s online refueling as the need for complex and costly robotic refueling machines is eliminated. A low-pressure and low-temperature moderator, as adopted from CANDU®s, provides a large heat sink when cooling capabilities are lost. Furthermore, overhead inlet and outlet plena eliminate the need for feeder pipes, and reduce the complexity of the design.

The SCWR is being designed to operate at a neutron power of 2540 MW_{th} with a thermal efficiency of $\eta_{th} = 0.48$, thus an electrical power output of 1200 MW_e. The high thermal efficiency is achieved through the use of a supercritical light water coolant with inlet and outlet plena temperatures of $T_{inlet} = 350°C$ and $T_{outlet} = 625°C$, respectively, and pressures of $P_{inlet} = 26$ MPa and $P_{outlet} = 25$ MPa, respectively. The design includes 336 vertical fuel channels which have evolved into high-efficiency re-entrant flow channels (HERC) [13].

A number of fuel iterations took place during the evolution of the SCWR. The earliest development of its fuel channel design began on a CANDU® type fuel bundle with 37 elements containing 4% enriched UO_2 in ThO_2 [14]. The design later evolved into a 54 element channel with 14 wt% PuO_2 in ThO_2 with a ZrO_2 non-fuel central pin [15, 16]. This design didn't allow enough heat transfer from the fuel elements to the coolant, thus, the surface-to-volume ratio of the fuel pins was increased by reducing the size of the pins. To compensate for the lack of fissile material, additional pins were added, which led to a 78-element design [17, 18]. Unfortunately that iteration had a positive coolant void

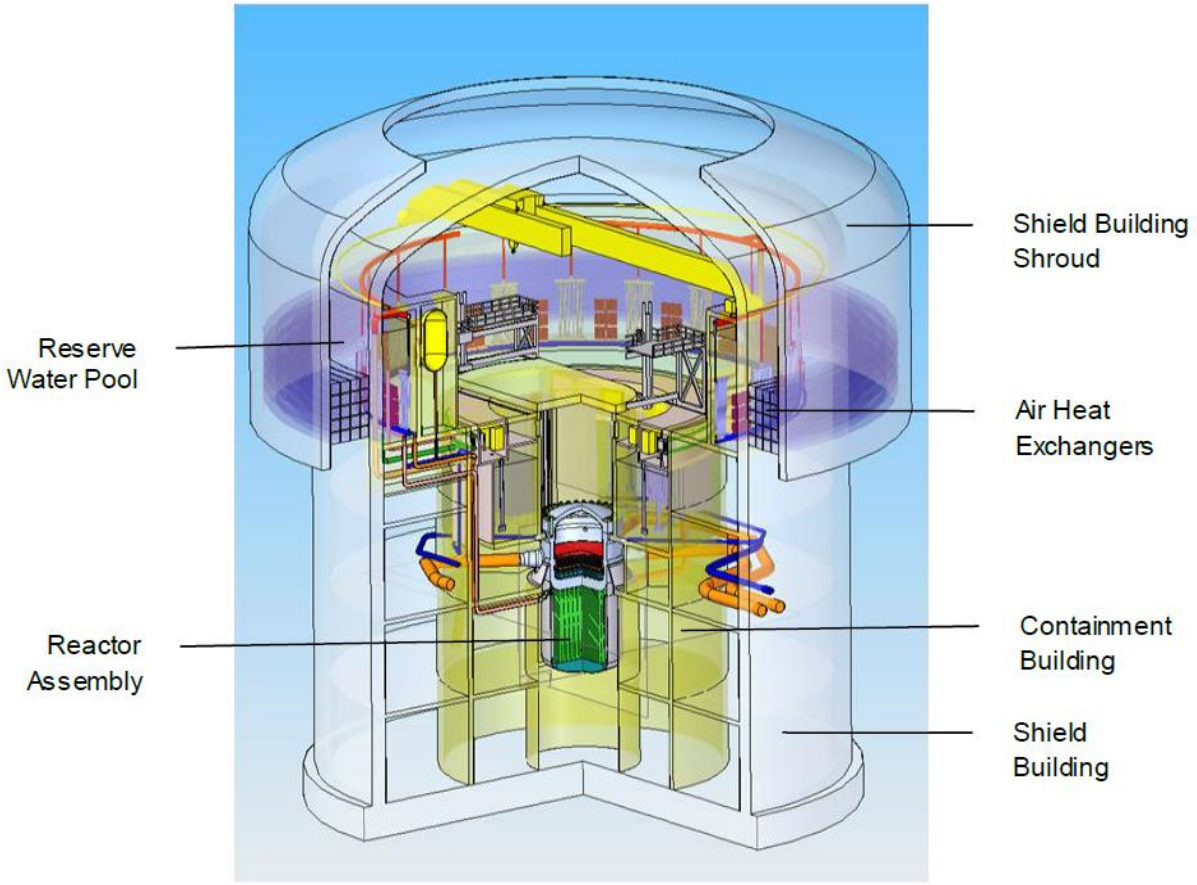

Figure 1.2: Canadian pressure-tube SCWR concept's reactor building (from [1]).

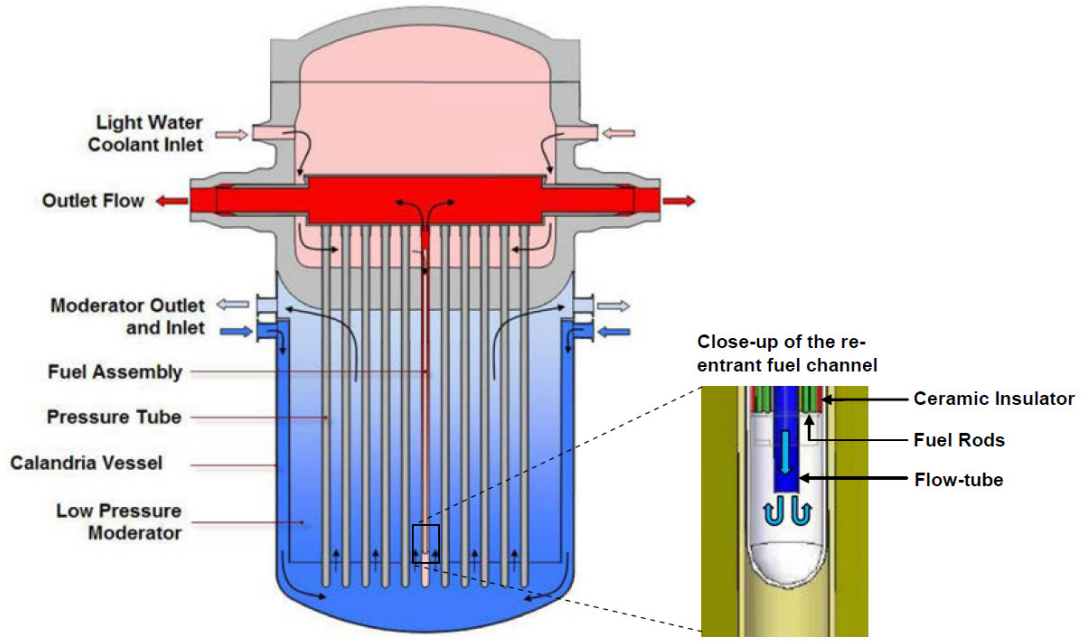

Figure 1.3: Canadian pressure-tube SCWR concept (from [1]).

reactivity (CVR) that varied from the top of the fuel channel (+10 mk) to the bottom (+4 mk) [19]. A negative CVR was desired in the SCWR design so that it would shutoff automatically in the event of coolant voiding, thus making it safer. In order to eliminate piping at the bottom of the channel and so that the channel could be refilled following a LOCA, the central non-fuel pin was replaced by a large coolant flow tube. With this fuel channel design, if the coolant was voided a large amount of negative reactivity would be inserted due to the significant lack of moderation. In order to incorporate the large central flow tube, the number of fuel pins was reduced from 78 (with 15, 21, and 42 fuel pins in the innermost to outermost ring of fuel [20]) to 62 (two concentric rings of 31 fuel pins each) [21, 22], which essentially eliminated the central non-fuel pin, and the innermost ring of fuel pins.

The fuel design used in this thesis was the next step in the development, which consists of two concentric rings of 32 fuel pins each, along with the large central coolant flow tube, as shown in Figure 1.4. The composition and geometry details for the fuel assembly can

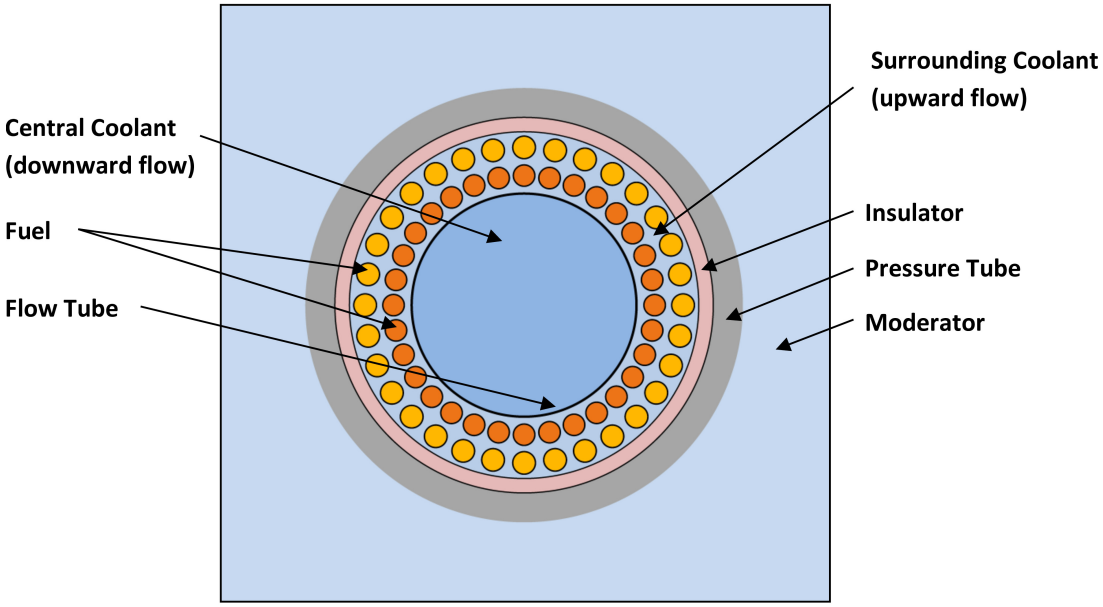

Figure 1.4: Canadian pressure-tube SCWR concept used in this work [2].

be found in [23, 24] which are presented in Chapters 3 and 4 of this thesis, respectively.

Even within this fuel channel design, sub-iterations were tested, for example in [25] a zirconium hydride solid moderator was used to displace coolant in the central flow tube to further reduce CVR. Additionally, the next iteration of the SCWR fuel assembly has gadolinia (Gd_2O_3) burnable neutron absorber (BNA) incorporated into eight of the 32 fuel pins, in each ring of fuel pins [26]. BNA was included to compensate for excess reactivity at the BOC and in order to reduce reliance on mechanically controlled reactivity devices. There has been much discussion regarding the design of reactivity control devices as well [11, 26–30]. However, their specifications have not been set as of the writing of this thesis, and they are outside of the scope of this work.

The SCWR fuel lattice model used throughout this thesis contains 15 wt% and 12 wt% PuO_2 in ThO_2 in the inner and outer ring of fuel pins, respectively. Additionally, as the fuel is irradiated ^{233}U builds in from ^{232}Th, along with ^{240}Pu, and ^{241}Pu. This is problematic from a nuclear data point of view since these isotopes have not been studied

Table 1.1: Relative (n, γ) in inner ring of SCWR fuel [4].

Isotope (i)	n_i/n_{total} (%)	$\sigma_{n,\gamma}$ (b)	$\frac{\Sigma_{(n,\gamma),i}}{\Sigma_{(n,\gamma),\text{total}}}$ (%)
^{232}Th	87.3	5	14.4
^{239}Pu	5.6	221	44.2
^{240}Pu	3.6	197	25.8
^{241}Pu	1.9	210	14.5
^{242}Pu	1.2	14	0.6
^{233}U	0.4	30	0.5

to the same extent as ^{235}U, ^{238}U, and ^{239}Pu. Mainly because Pu is not typically used in such high concentration in nuclear fuel, for example, most nuclear power reactors have a ^{235}U enrichment between 0.7% to 5% [31]. Having such elevated concentrations of Pu isotopes increases their impact on prediction uncertainties. This issue requires additional discussion on the topic of microscopic cross section uncertainties.

1.2.2 Microscopic Cross Section Uncertainties

As an example to illustrate the importance of cross section uncertainties consider the (n, γ) cross section in the thermal range. Table 1.1 shows the relative concentrations of the most important SCWR fuel actinides, at a midburnup of 20.3 MW·d·kg^{-1} [23], and the relative probability of radiative capture in any of those fuel nuclides[3]. The largest contributor to neutron capture in the fuel is ^{239}Pu and, fortunately, the major evaluated libraries ENDF/B-VII.1, JEFF-3.2, and JENDL-4.0 all agree very well (except in the fast neutron range where cross sections are extremely small). However, this is not the case for the ^{232}Th (n,γ) cross section which represents ∼14% of radiative captures in the fuel.

Figure 1.5 shows the ^{232}Th (n, γ) microscopic cross section for various libraries. Inconsistencies can be seen in the epithermal and resonance region from 0.5 eV to 100 eV, where the discrepancies are as large as a factor of 4 and can lead to significantly

[3]More exact uncertainty studies which incorporate fine energy group structure and proper material distributions have been performed ([24, 32, 33]) that mirror the simplistic analysis in Table 1.1.

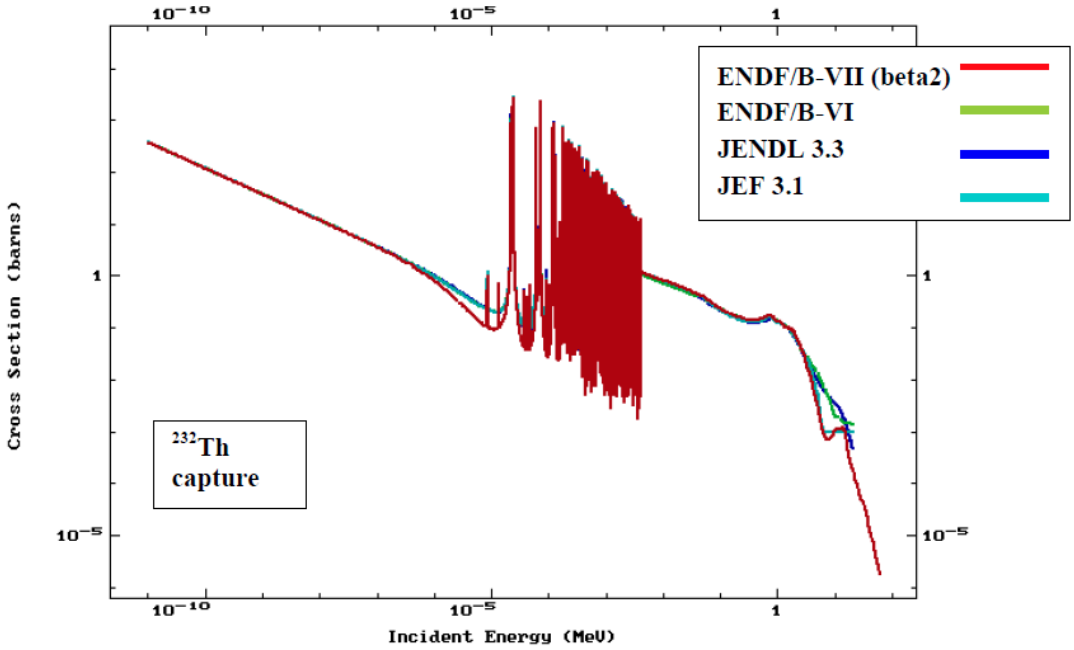

Figure 1.5: ^{232}Th (n, γ) cross section. Adapted from [3].

different simulation predictions. Various evaluated neutron libraries with different fine energy group structures and neutronics solvers have been investigated with SCWR geometry [34] where it was shown that SCWR simulations under a number of conditions are very sensitive to different libraries and neutronics solvers.

Microscopic cross sections can only be improved through further study, experimentation, and understanding of nuclear models. However there exist other methods of improving simulations predictions - even with uncertain, nuclear data.

1.2.3 Nuclear Data Adjustment

There exists a numerical nuclear data adjustment technique which uses generalized linear least squares fitting (GLLS) [35] to fine-tune data, by varying the data within its evaluated uncertainty, in order to produce optimized k_{eff} values for a set of experiments. Conceptually, after simulations are executed, additional information (experimental results) is added, which reduces the uncertainty on integral quantities, such as k_{eff}.

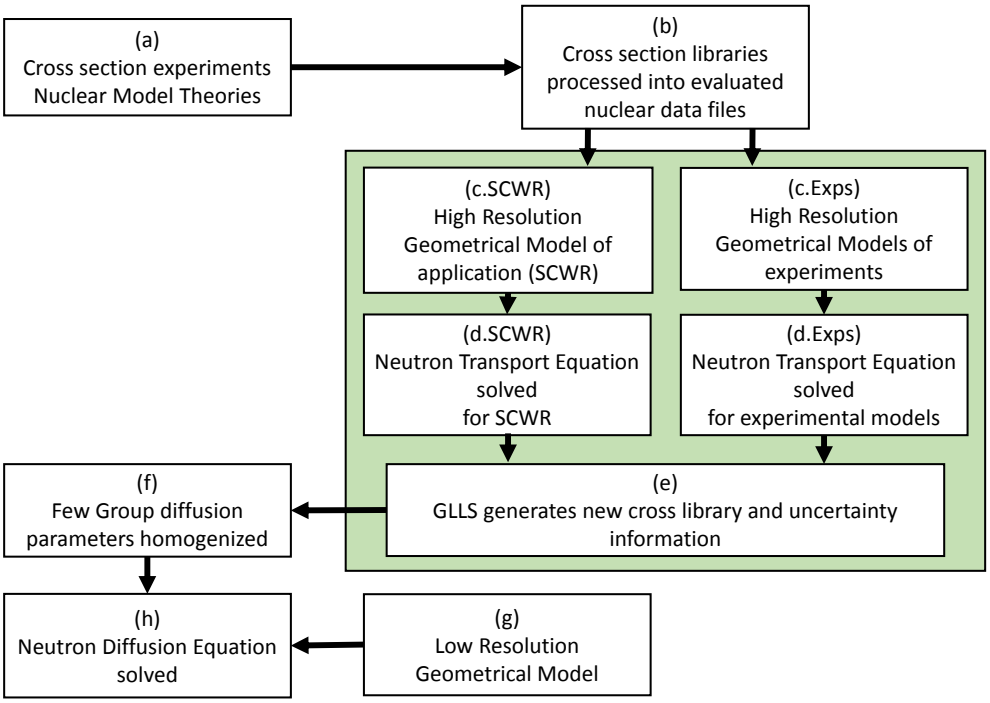

Figure 1.6: Reactor physics evaluation procedure along with a nuclear data adjustment.

Figure 1.6 is a modified version of Figure 1.1 that shows the reactor physics analysis procedure including a nuclear data adjustment. The general idea of this method is to have a large number of experiments that are simulated. Next, the sensitivities of criticality due to cross sections are determined [36–38] for each simulation model. The cross sections are then adjusted, within their established uncertainty, at the isotope, reaction, and group-wise level, including covariances, in order to reduce experimental and simulation k_{eff} discrepancies, for the entire set simultaneously.

In order for this strategy to function properly, a large number of experiments are needed. Certain experiments may be more or less useful to the adjustment procedure depending on how large the nuclear data sensitivities are, relative to the desired application.

GLLS nuclear data adjustment is a very powerful procedure, though it has its limitations. Specifically, it is possible that nuclear data is adjusted in an nonphysical way in order to fit experimental results. Thus, although the adjusted nuclear data may predict

perfect results, that same adjusted nuclear data may produce worse results if applied to alternative conditions, such as an accident scenario. In this case, the accident model should undergo the same procedure to have its own set of nuclear data produced in order to reproduce its experimental result. However, tuning nuclear data over the entire range of evolving conditions of an accident may not be practicable. Therefore, at the very least, caution is warranted if an adjusted nuclear data library is to be used in a different model [39].

In reality, the GLLS nuclear data adjustment method is difficult to implement as "experimental correlations" (or experimental covariances) are required, and are rarely easy to analyze or acquire. Incidentally, this method can be exploited to generate experimental designs which have large enough sensitivities to cover an application's sensitivities, such as was done with the SCWR by Sharpe *et al.* [23]. Thus, not only can experiments be used to better predict the application, existing experiments can be used in order to design and perform new experiments which will lead to further improved application predictions. This has been done through the optimization of a number of parameters (such as G, E, and c_k [40,41]) that determine how similar an application and experiment are, with the specific purpose to predict isotopic concentrations in a simulated irradiated fuel that could be manufactured for experimental reactors [23]. This specifically is one of the motivations for much of the work in this thesis.

1.2.4 Neutron Diffusion

The level of detail and uncertainty involved with microscopic cross sections mentioned above only directly applies to very accurate neutron transport codes. Routine calculations however, are typically performed by neutron diffusion codes which introduce errors based on major physics approximations needed in order to rapidly solve the Boltzmann equation. Improvement of these calculations is another motivation for this work.

In the less accurate neutron diffusion codes, few-group cross section libraries are generated by neutron transport codes, thus are indirectly influenced by microscopic cross section uncertainties. The generated cross section tables are then used to calculate core-wide power and flux distributions. The errors introduced from the physics approximations create much larger errors in calculated fluxes, when compared to measured powers, than do the nuclear data uncertainties. Part of this thesis demonstrates a novel method to reduce predicted power errors between transport calculations and diffusion calculations.

1.3 Objectives

The main motivation for the work in this thesis is to reduce prediction uncertainties in reactor physics calculations. A new experimentation technique is introduced in Chapter 3, the applicability of the ZED-2 experimental reactor to an SCWR bias calculation is presented in Chapter 4, and a novel method to improve diffusion solutions is revealed in Chapter 5; all with an SCWR theme. Before the journal articles in Chapter 3 to 5 are presented, the mathematical framework of reactor physics theories required to explain the work in this thesis is first offered, along with background on the topics, to set the context of the papers for the reader.

Chapter 2

Reactor Physics Theory and Background

This chapter presents the fundamental concepts of reactor physics theory that are used throughout the articles included in this thesis.

2.1 The Neutron Transport Problem

A keystone of reactor physics is the neutron transport problem. It is from the solution of the neutron transport equation that all other branches of reactor physics begin. Once formulated the solution provides details on the neutron flux, and in turn, the power distribution in the reactor. In fact, the power in a reactor core directly stems from fission reaction rate. The neutron flux can also be used to determine other reaction rates, integral responses, and integral response sensitivities.

From an engineering perspective, a knowledge of the flux is important because the flux can be used to determine local fuel powers. The powers in certain regions of the core, such as bundle power in a CANDU® reactor [42], have restrictions which are put forth by the licensee and enforced by the nuclear regulator, in Canada this is the Canadian

Nuclear Safety Commission (CNSC).

The time-independent neutron transport equation describes the balance of the neutron population in a particular region, $\mathbf{r}$, with energy, E, and direction, $\mathbf{\Omega}$, and is written as follows (ignoring delayed neutrons[1]):

$$\nabla \cdot \mathbf{J}(\mathbf{r}, \mathbf{\Omega}, E) + \Big(\Sigma_s(\mathbf{r}, \mathbf{\Omega} \rightarrow \mathbf{\Omega}', E \rightarrow E') + \Sigma_a(\mathbf{r}, E)\Big)\psi(\mathbf{r}, \mathbf{\Omega}, E) = \int_{4\pi}\int_0^\infty \Sigma_s(\mathbf{r}, \mathbf{\Omega}' \rightarrow \mathbf{\Omega}, E' \rightarrow E)\psi(\mathbf{r}, \mathbf{\Omega}', E')dE'd\mathbf{\Omega}' + \frac{\chi(\mathbf{r}, E)}{4\pi}\int_{4\pi}\int_0^\infty \nu(r, E')\Sigma_f(\mathbf{r}, E')\psi(\mathbf{r}, \mathbf{\Omega}', E')dE'd\mathbf{\Omega}' + S(\mathbf{r}, \mathbf{\Omega}, E), \quad (2.1)$$

where:

- $\mathbf{J}(\mathbf{r}, \mathbf{\Omega}, E)$ is the neutron current (bold font indicates a vector),
- $\mathbf{\Omega}$ is the neutron direction,
- $\Sigma_s(\mathbf{r}, \mathbf{\Omega} \rightarrow \mathbf{\Omega}', E \rightarrow E')$ is the macroscopic scattering cross section of neutrons being scattered out of direction $\mathbf{\Omega}$ and energy E, into any other direction $\mathbf{\Omega}'$ and any other energy E', at location $\mathbf{r}$,
- $\Sigma_a(\mathbf{r}, E)$ is the local macroscopic absorption cross section for energy E,
- $\psi(\mathbf{r}, \mathbf{\Omega}, E)$ is the neutron flux at position r, in direction $\mathbf{\Omega}$, with energy E,
- $\Sigma_s(\mathbf{r}, \mathbf{\Omega}' \rightarrow \mathbf{\Omega}, E' \rightarrow E)$ is the macroscopic cross section for a neutron to scatter into direction $\mathbf{\Omega}$ and into energy E (note the prime, $'$, simply indicates the variable which is being integrated), from $\mathbf{\Omega}'$ and energy E', at location $\mathbf{r}$,
- $\chi(\mathbf{r}, E)$ is the fission spectrum and gives the probability a neutron will end up with energy E in region $\mathbf{r}$,

[1] All the work performed in this thesis is static and has no time dependence

- $\nu(r, E)$ is the number of neutrons emitted in region $\mathbf{r}$ at energy E after a fission occurs at the same location,

- $\Sigma_f(\mathbf{r}, E)$ is the macroscopic fission cross section,

- $S(\mathbf{r}, \mathbf{\Omega}, E)$ is a point neutron source[2] producing neutrons at $\mathbf{r}$ in direction $\mathbf{\Omega}$ with an energy E.

In its current form, Equation 2.1 cannot easily be solved except for ideal non-realistic situations [43], such as a homogeneous cylinder or other elementary shapes. In order to reduce its complexity a number of numerical approximations must be made. These approximations can vary significantly depending on the type of solution that is required, or on the specific problem. For example, a common approximation is to split a problem into many regions, and treating the cross sections in each individual region as constant - this is discretization and homogenization of space. Another common approximation is discretizing energy, for both cross sections and the neutron flux, and also the discretization of angular flux. Relevant techniques that approximate and solve Equation 2.1 are described in the following sections.

2.1.1 The Neutron Diffusion Equation

The neutron diffusion equation is an approximation of the neutron transport equation in the sense that their solutions are the flux as a function of energy and position. One major difference between the two solutions is diffusion's lack of an angular component.

Following the simplistic derivation of the neutron diffusion equation from [7], consider neutrons that were scattered from a differential volume element $d^3\mathbf{r} = r^2\, dr\, d\mu\, d\psi$, where $\mu = \cos\theta$ is the scattering cosine, into an area, dA, centered on the origin. The neutron

[2]Not to be confused with the source term, q_g, introduced in Section 2.1.2.

current through the unit area is:

$$j_{r=0}(r,\mu,\phi)\,dr\,dA = \frac{\mu\, e^{-\Sigma_t r}\,\Sigma_s\,\phi(r,\mu,\psi)\,d^3r\,dA}{4\pi\, r^2}, \tag{2.2}$$

where Σ_t is the total scattering cross section defined by $\Sigma_t = \Sigma_s + \Sigma_a$, ϕ is the macroscopic flux, and ψ is azimuthal coordinate. To determine the total current passing downwards through an infinitesimal area on the origin, the above equation must be integrated over all space above the plane.

$$j^-_{r=0}\,dA = \int_0^\infty \int_0^{2\pi} \int_0^1 \frac{\mu\, e^{-\Sigma_t r}\,\Sigma_s\,\phi(r,\mu,\psi)\,dA}{4\pi} d\mu\,d\psi\,dr. \tag{2.3}$$

In order to easily solve this integral, some approximations are commonly made[3]. Firstly, the flux can be expanded as a Taylor series:

$$\phi(\mathbf{r}) = \phi(0) + \mathbf{r}\cdot\nabla\phi(0) + \frac{1}{2}\,r^2\,\nabla^2\phi(0) + \ldots, \tag{2.4}$$

and truncated after the second term, which reduces the complexity of the integral in Equation 2.3. Secondly, by approximating $\Sigma_s \gg \Sigma_a$ the integral's complexity is further reduced, and finally, the neutrons are assumed to scatter isotropically[4]. The spatial variable can be switched from r to x by using a trigonometric identity [7], which is useful considering most simulations are performed using a Cartesian grid. The approximations can then be applied to Equation 2.3 which, after integrating, becomes:

$$j^-_x(0) = \frac{1}{4}\phi(0) + \frac{1}{6\Sigma_s}\frac{d\phi(0)}{dx}. \tag{2.5}$$

[3]The approximations described herein reflect those made in the PARCS diffusion code [6] that was used in this work.

[4]The approximation can be relaxed to include anisotropic scattering

The same can be done for neutrons passing upwards through the plane, which results in:

$$j_x^+(0) = \frac{1}{4}\phi(0) - \frac{1}{6\Sigma_s}\frac{d\phi(0)}{dx}. \tag{2.6}$$

The two above equations can be subtracted from one another to find the total current passing through the plane:

$$J_x(0) = j_x^+(0) - j_x^-(0) = -\frac{1}{3\Sigma_s}\frac{d\phi(0)}{dx} = -D\frac{d\phi(0)}{dx}, \tag{2.7}$$

and finally, if the coordinate system is generalized, along with the location of the plane of interest:

$$J(r) = -D\nabla\phi(r). \tag{2.8}$$

Equation 2.8 is known as Fick's law [7] and indicates that the neutron current flows in the direction that the flux changes most rapidly in space, where D is the diffusion coefficient. In the above derivation, $D = 1/\Sigma_s$ was used, however, in more accurate derivations the diffusion coefficient is defined by:

$$D = \frac{1}{\Sigma_t - \bar{\mu}_0\Sigma_s} = \frac{1}{3\Sigma_{tr}}, \tag{2.9}$$

where $\bar{\mu}_0$ is the average scattering cosine, and Σ_{tr} is the transport cross section.

Now that the Fick's law has been introduced, the derivation of the diffusion equation returns to the transport equation (Equation 2.1). The quantity of interest in a nuclear reactor is the heat generated from the fission process, thus, the reaction rates within a node (spatial region) are desired. In order to arrive at this the transport equation must be integrated over a region of volume V. Furthermore, the angle-integrated flux is needed, and integration over angle is not trivial. However, as mentioned above, for the purpose of diffusion theory, the flux is assumed to be isotropic. Therefore, to determine the reaction

rates, the transport equation must be integrated over angle, energy, and volume.

The neutron leakage term ($\nabla \cdot \mathbf{J}$), also known as the streaming term, cannot be directly integrated since the angular current has no algebraic relationship to the angle-integrated current. Thus, the current is replaced through the use of Fick's Law.

If space and energy are discretized, the integro-differential equation is converted into a set of coupled equations. After the approximations are applied to Equation 2.1, the result is integrated over all angles to remove the Ω component.

$$-D_g \nabla^2 \phi_g(r) + \Big(\Sigma_{s,g\to g'}(r) + \Sigma_{a,g}(r)\Big)\phi_g(r) = \sum_{g'}^{G} \Sigma_{s,g'\to g}(r)\,\phi_{g'}(r) + \chi_g(r) \sum_{g'}^{G} \nu_{g'} \Sigma_{f,g'}(r)\,\phi_{g'}(r) + S_g(r), \qquad \text{for all energy groups } g, \quad (2.10)$$

which is a set of G coupled second-order non-homogeneous differential equations.

For the work done in this thesis a two energy group coarse mesh finite difference (CMFD) form of the diffusion equation was used. In the finite difference method, spatial discretization is achieved through the assumption that all cross sections and diffusion coefficients are constant throughout a homogenized region, thus their r dependence is removed. Furthermore, if spatial dependence is removed from ϕ, and only two energy groups are considered, Equation 2.10 can trivially be integrated over the volume of a node. Thus the CMFD diffusion equation is:

$$J_1 + (\Sigma_{tt1} + \Sigma_{s12} - \nu\Sigma_{f1}/k)h_x h_y \phi_1 + (-\Sigma_{s21} - \nu\Sigma_{f2}/k)h_x h_y \phi_2 = 0 \qquad \text{Fast}, \quad (2.11)$$

$$J_2 + (-\Sigma_{s12})h_x h_y \phi_1 + (\Sigma_{tt2} + \Sigma_{s21})h_x h_y \phi_2 = 0 \qquad \text{Thermal}, \quad (2.12)$$

where h_x and h_y are the nodal dimensions, k is the effective multiplication constant of

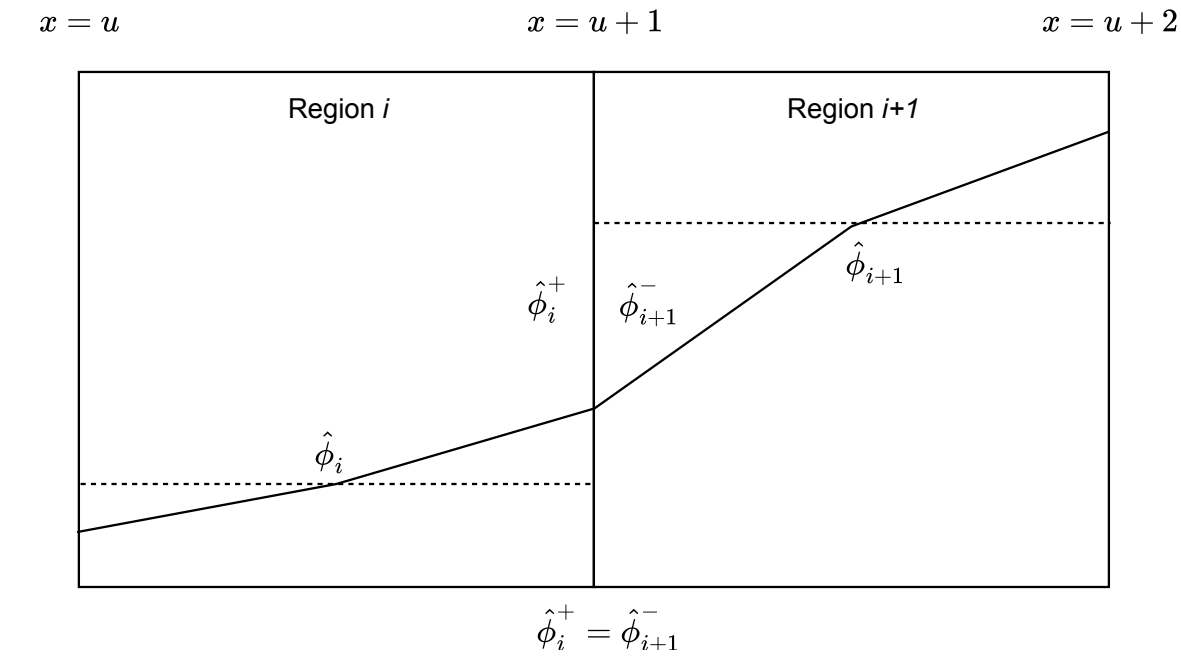

Figure 2.1: CMFD fluxes and currents.

the system, and J is the current which flows out of a node. Σ_{tt} is the total-transfer cross section[5], and is the summation of neutron absorptions and neutrons that have been scattered out of a group but is adjusted by neutron production reactions (n, xn).

The interface-averaged current is the amount of flux that leaks between nodes. Consider Equation 2.8 in 1-D, under the CMFD approximation:

$$J(x) = -D\nabla\phi(x) = -D\frac{d\phi(x)}{dx} = -D\frac{\Delta\phi}{\Delta x}, \tag{2.13}$$

where Newton's difference quotient was used to transition from a derivative to a finite difference. Figure 2.1 shows two adjacent nodes with nodally-averaged fluxes ($\hat{\phi}_i$ and $\hat{\phi}_{i+1}$)[6], and a common interface flux ($\hat{\phi}_i^+ = \hat{\phi}_{i+1}^-$). In this formulation, the continuity of flux and current is maintained.

[5]Also called the total-scatter cross section, which causes confusion because it is not the sum of scatter cross sections.

[6]The hat (ˆ) indicates a homogenized parameter. Macroscopic cross sections are assumed to be homogenized, unless otherwise indicated by an r dependence.

Equation 2.13 can be applied to both nodes in Figure 2.1 which yields:

$$J_i(u+1) = -D_i \frac{\hat{\phi}_i^+ - \hat{\phi}_i}{h_i/2} = -2D_i \frac{\hat{\phi}_i^+ - \hat{\phi}_i}{h_i}, \tag{2.14}$$

$$J_{i+1}(u+1) = -D_{i+1} \frac{\hat{\phi}_{i+1} - \hat{\phi}_{i+1}^-}{h_{i+1}/2} = -2D_{i+1} \frac{\hat{\phi}_{i+1} - \hat{\phi}_{i+1}^-}{h_{i+1}}. \tag{2.15}$$

These two equations can be solved with the elimination of the interface flux, which leaves:

$$\hat{J}_i(u+1) = -2D_i D_{i+1} \frac{\hat{\phi}_{i+1} - \hat{\phi}_i}{D_i h_{i+1} + D_{i+1} h_i}, \tag{2.16}$$

which is the interface-averaged current at the $x = u+1$ nodal interface when the current and flux are continuous. At this point, interface-averaged flux continuity and current continuity on either side of an interface is maintained, because of physical reasoning (i.e., the flux and currents are in reality continuous everywhere). However, the next few sections describe why these continuities can not kept in order be to achieve mathematical equivalence.

Homogenization

It is now important to formally introduce the concept of spatial homogenization and energy condensation (or collapse) of fine energy structure cross sections to produce few-group homogenized[7] cross sections. A node, or homogenization region, is the spatial region over which the homogenization process is performed. A node could be a fuel bundle as shown in Figure 1.4, a fuel pin and surrounding coolant in a pressurized water reactor (PWR), or any other region of interest in a reactor.

The purpose of the homogenization process is to obtain a set of flux-weighted cross sections, such that when multiplied by the flux, they reproduce heterogeneous reaction rates. Likewise, the homogenized interface-averaged interface current should reproduce

[7]Homogenization implies both spatial homogenization and energy collapse throughout this thesis.

the heterogeneous interface-averaged current across the nodal interface. If the diffusion equation (Equation 2.10) is integrated over energy and a node's volume, the first term turns into the nodal leakage at each surface, while the remaining terms are the volume's reaction rates. The reaction rate terms can be written as [7, 44]:

$$\int_{V_i} \hat{\Sigma}_{x,g}(r)\,\hat{\phi}_g(r)\,d^3r = \int_{V_i} \Sigma_{x,g}(r)\,\phi_g(r)\,d^3r, \tag{2.17}$$

and since the parameters we seek are constant over a homogenized region, the homogenized cross sections are:

$$\hat{\Sigma}_{x,g} = \frac{\int_{V_i} \Sigma_{x,g}(r)\,\phi_g(r)\,d^3r}{\int_{V_i} \hat{\phi}_g(r)\,d^3r}. \tag{2.18}$$

Going back to the leakage term, before Fick's Law is applied:

$$\int_{V_i} \nabla\cdot\hat{\mathbf{J}}_\mathbf{g}(\mathbf{r})\,d^3r = \int_{V_i} \nabla\cdot\mathbf{J}_\mathbf{g}(\mathbf{r})\,d^3r, \tag{2.19}$$

and since a node is a closed surface the divergence theorem can be utilized in order to convert the volume integral into a surface integral:

$$\oint_{S_i^k} \hat{\mathbf{J}}_\mathbf{g}(\mathbf{r})\cdot d\mathbf{S} = \oint_{S_i^k} \mathbf{J}_\mathbf{g}(\mathbf{r})\cdot d\mathbf{S}, \tag{2.20}$$

where S_i^k is the k^{th} surface of homogenized region i. Fick's law from Equation 2.8 can now be used in Equation 2.20 to generate surface dependant diffusion coefficients:

$$\hat{D}_g^k = \frac{-\oint_{S_i^k} \hat{\mathbf{J}}_\mathbf{g}(\mathbf{r})\cdot d\mathbf{S}}{\oint_{S_i^k} \nabla\hat{\phi}_g(r)\cdot d\mathbf{S}}. \tag{2.21}$$

It is difficult to satisfy Equations 2.18 and 2.21 as the solutions of the global heterogeneous and homogeneous problems must be known in advance. Specifically, $\phi_g(r)$ from Equation 2.10 depends on the homogenized $\hat{D}_g^k$ from Equation 2.21. Meanwhile, $\hat{D}_g^k$ is

determined by $\nabla\hat{\phi}_g(r)$ in the denominator of Equation 2.21 which is the flux solution from Equation 2.10. The conventional way to circumvent Equation 2.21 is to use the definition of the diffusion coefficient from Equation 2.9. However, this introduces new issues as this definition of D is not surface dependant, thus the heterogeneous and homogeneous interface-averaged currents in Equation 2.19 are not forced to be equal.

The problem was addressed in 1978 when Koebke [45] introduced equivalence theory which hinged on the concept of flux discontinuities between nodes. In reality, the concept of a flux distribution in a node comprised of homogenized cross sections is meaningless as it does not reflect the actual flux shape within a heterogeneous region. This is contrary to the nodally-averaged homogeneous flux, which should be equal to the nodally-averaged heterogeneous flux in order to have equivalence, otherwise solving the diffusion equation is worthless. Thus, continuity of the homogeneous flux was relaxed which gave way to flux discontinuities factors written as:

$$f_{i,g}^k = \frac{\bar{\psi}_{i,g}^k}{\hat{\phi}_{i,g}^k}. \tag{2.22}$$

Koebke realized with additional homogenization parameters any arbitrary diffusion coefficient could be used to force equivalence between the heterogeneous and homogeneous solutions. Furthermore, a set of heterogeneity factors could be found such that the diffusion coefficients ($D_{i,g}^k$) were identical on all sides (i.e., a single $D_{i,g}$). This method produced excellent results if the node was homogenized in a (a)symmetric model, and later used in a (a)symmetric model, however if it was homogenized in a symmetric environment and used in an asymmetric environment, or vice-versa, equivalence was not achieved [44].

Later, in 1986, Smith [44] introduced General Equivalence Theory (GET) which built on Koebke's realization that any arbitrary diffusion coefficient could be used. However, rather than iterating on heterogeneity factors to find a constant $D_{i,g}$, he suggested to fix a $D_{i,g}$ based on Equation 2.9 and calculate discontinuity factors directly. If Equation 2.22

is rearranged for $\hat{\phi}^k_{i,g}$ and substituted into Equations 2.14 and 2.15 (in 1-D):

$$J_i(u+1) = -2D_i \frac{\bar{\psi}^+_i / f^+_i - \hat{\phi}_i}{h_i}, \tag{2.23}$$

$$J_{i+1}(u+1) = -2D_{i+1} \frac{\hat{\phi}_{i+1} - \bar{\psi}^-_{i+1} / f^-_{i+1}}{h_{i+1}}. \tag{2.24}$$

Therefore, exact equivalence can be achieved if discontinuity factors are calculated by:

$$f^k_i = \frac{\bar{\psi}^k_i}{\hat{\phi}_i \mp \dfrac{\bar{J}^k_i h_i}{2D_i}}, \tag{2.25}$$

where $\bar{\psi}^k_i$ and $\bar{J}^k_i$ are acquired from the heterogeneous solution[8] and the $\mp$ is a subtraction at the upper coordinate of a node, and addition at the lower coordinate of a node. Figure 2.2 demonstrates a flux discontinuity between two adjacent nodes, as would be the case when discontinuity factors are used.

To transform Equations 2.23 and 2.24 into a nodally coupled problem, use is made of the fact that $\bar{J}^+_i = \bar{J}^-_{i+1}$, thus:

$$-2D_i \frac{\bar{\psi}^+_i / f^+_i - \hat{\phi}_i}{h_i} = -2D_{i+1} \frac{\bar{\psi}^-_{i+1} / f^-_{i+1} - \hat{\phi}_{i+1}}{h_{i+1}}, \tag{2.26}$$

where a positive current is directed in the $+x$ direction. Now the heterogeneous interface-averaged flux is solved for, recalling that it is continuous (as opposed to the homogeneous interface-averaged flux):

$$\bar{\psi}^+_i = \bar{\psi}^-_{i+1} = f^+_i \, f^-_{i+1} \frac{D_i \, h_{i+1} \, \hat{\phi}_i + D_{i+1} \, h_i \, \hat{\phi}_{i+1}}{D_i \, h_{i+1} \, f^-_{i+1} + D_{i+1} \, h_i \, f^+_i}, \tag{2.27}$$

[8]The bar (-) indicates an averaged parameter.

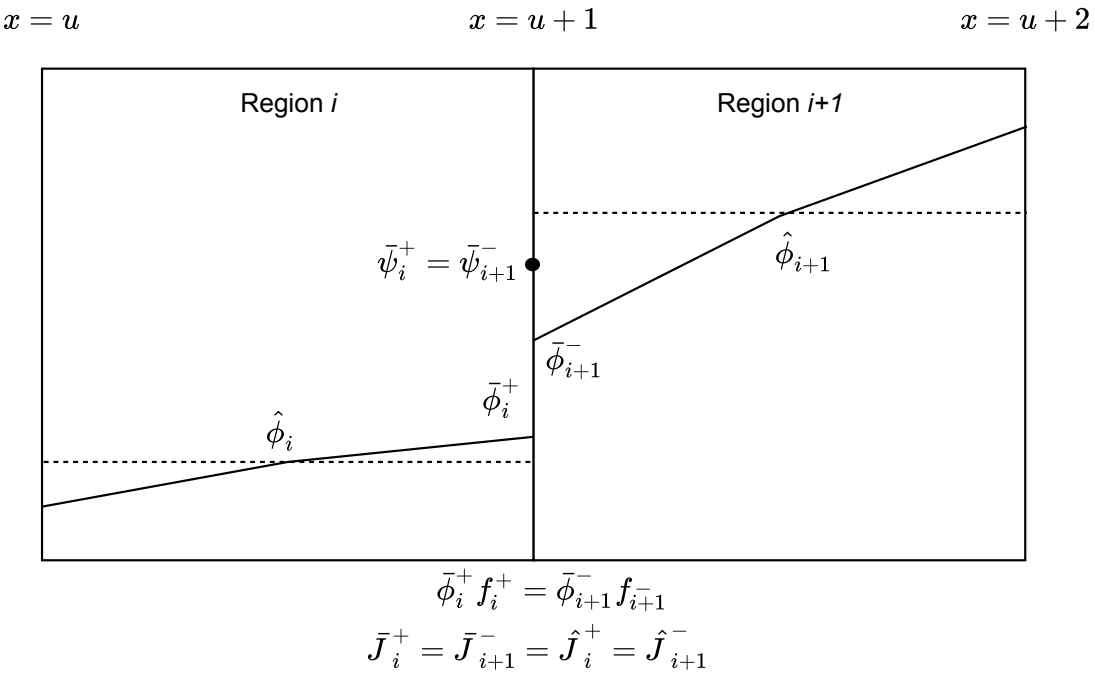

Figure 2.2: General Equivalence Theory CMFD flux discontinuity between nodes.

then Equation 2.27 is substituted back into Equation 2.24:

$$\hat{J}_i(u+1) = -2D_i\, D_{i+1} \frac{f_{i+1}^- \hat{\phi}_{i+1} - f_i^+ \hat{\phi}_i}{D_i\, h_{i+1}\, f_{i+1}^- + D_{i+1}\, h_i\, f_i^+}, \tag{2.28}$$

where $\hat{J}_i(u+1)$ is the interface-averaged current which crosses the nodal boundary at $x = u + 1$ in Figure 2.2. This is the standard nodal coupling equation for GET CMFD problems. Ultimately, a global heterogeneous multi cell that had been homogenized into a number of nodes will result in exact equivalence if Equations 2.9, 2.11, 2.12, 2.23, and 2.24, are satisfied.

The diffusion equation is computationally solved by choosing an arbitrary initial flux shape, then iterating through all nodes in the problem and updating the energy group fluxes at each node. Iterations continue until a convergence criterion is met.

In summary, the diffusion equation is an approximation of the transport equation, and because it's quickly solved, it is commonly used in routine calculations. However, its

use comes with many issues, specifically that it cannot generally reproduce the transport solution. Advanced homogenization techniques can be used to improve equivalence between heterogeneous and homogeneous solutions, and are discussed at length in Section 5.

2.1.2 Random: The Monte Carlo Multigroup Method

One way to accurately solve the Boltzmann transport equation is by using the Monte Carlo method. The method consists of producing (initializing) neutrons with a position, energy, and angular distribution, then following their neutronic interactions through many generations. One benefit of the Monte Carlo method is that essentially no assumptions need to be made to the transport equation itself.

Consider a neutron travelling through a medium with total cross section, $\Sigma_t(r)$. It travels along a straight line until an interaction[9] occurs. The probability of a collision occurring between r and $r + dr$ along a neutron's path is [7]:

$$P(r)dr = \Sigma_t(r)e^{-\int_0^r \Sigma_t(r')dr'}dr. \tag{2.29}$$

Note that the integral of this function over $r = 0 \rightarrow \infty$ is 1. In other words, the neutron must interact at some point (provided it's not in an infinite vacuum). $P(r)$ is the probability distribution function (PDF), of the neutron's interaction. This equation can be manipulated such that if a random number, λ, (hence the name Monte Carlo) is chosen between 0 and 1, that the neutron will travel a distance r which corresponds to that random number, according to the PDF. To do this, Equation 2.29 must be inverted.

If the medium in which the neutron travels is considered to be homogeneous, for

[9]Interactions are commonly referred to as collisions in the literature, but in reality, the neutron's wave function overlaps with that of a nucleus, which allows the interaction to occur. To coincide with other literature, collisions will be used herein.

simplicity, then the exponent becomes:

$$-\int_0^r \Sigma_t \, dr' = -\Sigma_t \Big|_0^r = -\Sigma_t \, r. \tag{2.30}$$

Therefore,

$$P(r)dr = \Sigma_t \, e^{-\Sigma_t \, r}. \tag{2.31}$$

In other words, the chance of having a collision occur at the beginning of the neutron's flight is high, then decreases with distance, solely because the neutron has a lower chance of penetrating to that distance in the first place. Another important distribution is the cumulative distribution function (CDF), $C(r)$, which increases monotonically with distance. Equation 2.29 can't be inverted, in general, because it's possible to have multiple values r for the same value of P(r) in an inhomogenous mixture. The CDF in the case of Equation 2.31 is the cumulative probably for the neutron to penetrate to r:

$$C(r) = \int_0^r P(r')dr' = \int_0^r \Sigma_t \, e^{-\Sigma_t \, r'} dr' = 1 - e^{-\Sigma_t \, r} = \lambda_r. \tag{2.32}$$

The random number, λ_r (the r subscript represents position), is chosen between 0 and 1, which represents C(r) as it increases from 0 to 1, when it's integrated over all space. The above equation can be rearranged and solved for r:

$$r = -\frac{1}{\Sigma_t} \ln(1 - \lambda_r), \tag{2.33}$$

which determines how far a neutron travels before having its first collision, based on a random number chosen, between 0 and 1.

Once the location of the first collision occurs is determined, the type of reaction must then be determined, again based on a random number. Recall that the chance of any type of reaction occurring is simply the total cross section, Σ_t. The addition of all other

reaction cross sections is equal to Σ_t, therefore, if each individual cross section is weighted by Σ_t, then the weighted sum must be equal to 1:

$$\frac{1}{\Sigma_t(r,E)} \sum_x \Sigma_x(r,E) = 1, \tag{2.34}$$

where x is a reaction such as fission, scatter, etc. When a random number, λ_x (x subscript represents a reaction), is chosen between 0 and 1, reaction cross sections beginning with reaction $x = 0$ (zero and other numbers are labels for reactions) are added, until the random number times the total cross section is reached:

$$\sum_{x=0}^{i} \Sigma_x(r,E) \leq \Sigma_t(r,E)\,\lambda_x < \sum_{x=0}^{i+1} \Sigma_x(r,E), \tag{2.35}$$

where the ith reaction occurs. The reactions can be elastic scatter (n,n), inelastic scatter (n,n'), fission (n,f), neutron production such as $(n,2n)$ or $(n,3n)$, neutron disappearance such as (n,p) or (n,α), or radiative capture (n,γ).

Once a reaction is chosen, two things can happen to the neutron, it is either absorbed or scattered. Even if a fission occurs, and neutrons are produced, the neutron that was being tracked is destroyed. Those newly produced neutrons, however, are saved to be simulated in the subsequent generation. Only scattered neutrons continue after a collision and are followed until they are absorbed or reach the boundary of the domain. Absorbed neutrons can create new neutrons if the fission reaction was randomly selected, according to Equation 2.35, for the following generation. Each neutron (also called a history) is followed until all neutrons in a given generation are absorbed.

When a fission reaction is chosen following an absorption, it must be determined which fissionable isotope will cause the fission. This is done in an identical way to Equation 2.35, except that only the isotopes in the mixture where the neutron has landed are considered. After the nuclide is selected, the next generation's neutron energies are chosen from the

fission spectra, $\chi(x, E)$, of the fissioned nuclide.

In multigroup mode, KENO V.a (which is used in the work in this thesis) uses a cumulative transfer probability distribution to randomly select which energy group the neutron is transferred to, after a scatter. Once a new energy group is chosen, the scatter angle is determined from an angular scattering distribution. For additional details about scattering in KENO V.a, see [46]. Other codes, such as MCNP, use a continuous probability distribution since the neutron energies are continuous [47].

The scalar flux[10] is calculated using the track-length estimator, where in a region z in energy group g it is given as [46]:

$$\psi_{z,g} = \frac{\sum_{k=1}^{K} l_{k,z}}{V_z}, \tag{2.36}$$

where $l_{k,z}$ is the path length traversed by neutron k within the region z, K is the total number of histories in the generation; and V_z is the volume of region z. The angular flux, which is introduced in more detail later in the section, has the same form as Equation 2.36 except only neutrons with an angle near Ω are summed in the numerator.

Various Monte Carlo techniques can be used to decrease simulation time, reduce statistical uncertainties, and reduce computational resources. These approaches, such as Russian Roulette, among other rejection techniques, randomly delete neutrons. Other techniques involve weighting, which simulate multiple neutrons travelling along the same path. If correctly used, these techniques can be very powerful in improving the predictive power of Monte Carlo codes. The techniques are code dependent and not described in this thesis. For additional details see [7, 46–49].

[10]Equation 2.36 is true when all Monte Carlo weights are set to 1.

2.1.3 Converting the Transport Equation to Monte Carlo Format

This section presents the connection between the Monte Carlo treatment of individual neutrons and the Boltzmann Transport Equation. To accomplish this, Equation 2.1 must eventually be transformed into an equation that includes neutrons' path lengths, and multiple generations. Starting with Equation 2.1:

$$\nabla \cdot \mathbf{J}(\mathbf{r}, \mathbf{\Omega}, E) + \Big(\Sigma_s(\mathbf{r}, \mathbf{\Omega} \to \mathbf{\Omega}', E \to E') + \Sigma_a(\mathbf{r}, E)\Big)\, \psi(\mathbf{r}, \mathbf{\Omega}, E) = \int_{4\pi}\int_0^\infty \Sigma_s(\mathbf{r}, \mathbf{\Omega}' \to \mathbf{\Omega}, E' \to E)\, \psi(\mathbf{r}, \mathbf{\Omega}', E')\, dE'\, d\mathbf{\Omega}' + \frac{\chi(\mathbf{r}, E)}{4\pi} \int_{4\pi}\int_0^\infty \nu(E')\, \Sigma_f(\mathbf{r}, E')\, \psi(\mathbf{r}, \mathbf{\Omega}', E')\, dE'\, d\mathbf{\Omega}' + S(\mathbf{r}, \mathbf{\Omega}, E),$$

if energy group notation (i.e., $\psi_g = \int_g^{g+1} \psi(E')\, dE'$) is used, the scatter-in source and fission source add to make the source term (assume that S is negligible compared to the other terms):

$$q_g(\mathbf{r}, \mathbf{\Omega}) = \sum_{g'} \int_{4\pi} \Sigma_{s,g'\to g}(\mathbf{r}, \mathbf{\Omega}' \to \mathbf{\Omega})\, \psi_{g'}(\mathbf{r}, \mathbf{\Omega}')\, d\mathbf{\Omega}' + \frac{1}{k_{\text{eff}}} \sum_{g'} \frac{\chi_{g'\to g}(\mathbf{r})}{4\pi} \int_{4\pi} \nu_{g'} \Sigma_{f,g'}(\mathbf{r})\, \psi_{g'}(\mathbf{r}, \mathbf{\Omega}')\, d\mathbf{\Omega}'. \quad (2.37)$$

Equation 2.37 can be used to replace the neutron production terms in Equation 2.1. Also, Σ_t replaces the scatter-out and absorption terms which results in:

$$\nabla \cdot \mathbf{J_g}(\mathbf{r}, \mathbf{\Omega}) + \Sigma_{t,g}(\mathbf{r})\, \psi_g(\mathbf{r}, \mathbf{\Omega}) = q_g(\mathbf{r}, \mathbf{\Omega}). \quad (2.38)$$

The current must be transformed into a flux through: $\mathbf{J} = \psi\, \mathbf{\Omega}$. The product rule can now be used:

$$\nabla \cdot \mathbf{J} = \nabla \cdot (\psi\, \mathbf{\Omega}) = (\nabla \psi) \cdot \mathbf{\Omega} + \psi\, (\nabla \cdot \mathbf{\Omega}) = \mathbf{\Omega} \cdot (\nabla \psi), \quad (2.39)$$

because in the last step, $\mathbf{\Omega}$ does not change with space and its derivative is zero. Therefore, Equation 2.38 becomes:

$$\mathbf{\Omega} \cdot \nabla \psi_g(\mathbf{r}, \mathbf{\Omega}) + \Sigma_{t,g}(\mathbf{r})\, \psi_g(\mathbf{r}, \mathbf{\Omega}) = q_g(\mathbf{r}, \mathbf{\Omega}). \tag{2.40}$$

Equation 2.40 is in the form of $\dfrac{dy}{dx} + a(x)\, y = b(x)$, which is a first-order linear differential equation that can be solved by using an integrating factor of $e^{\int a(x)\, dx}$ [50]. For simplicity, the angular variable and the energy group label are dropped, for now. Furthermore, rather than considering the balance of Equation 2.40 in an infinitesimal volume around r, it is desirable to determine the neutron contribution at $\mathbf{R_0}$, due to another point, $r\,\mathbf{\Omega}$. This is accomplished by changing the variables from $r \Rightarrow \mathbf{R} = \mathbf{R_0} - r\,\mathbf{\Omega}$. Now the integration can be considered along a line from $r\,\mathbf{\Omega} \rightarrow \mathbf{R_0}$, and the ∇ operator becomes $d/d(\mathbf{R_0} - r\,\mathbf{\Omega})$. The new form of Equation 2.40 is:

$$\frac{d\,\psi(\mathbf{R_0} - r\,\mathbf{\Omega})}{d\,(\mathbf{R_0} - r\,\mathbf{\Omega})} + \Sigma_t(\mathbf{R_0} - r\,\mathbf{\Omega})\, \psi(\mathbf{R_0} - r\,\mathbf{\Omega}) = q(\mathbf{R_0} - r\,\mathbf{\Omega}). \tag{2.41}$$

To solve this equation, the integrating factor must be $e^{-T(r)}$, where $T(r)$ is defined as:

$$T(r) = \int_0^{r'} \Sigma_t(\mathbf{R_0} - r\,\mathbf{\Omega}) dr'. \tag{2.42}$$

If the integrating factor is multiplied on both sides of Equation 2.41, and the derivative and integrals are considered along r.

$$e^{-T(r)} \left(\frac{d\psi(\mathbf{R_0} - r\,\mathbf{\Omega})}{d\,(\mathbf{R_0} - r\,\mathbf{\Omega})} + \Sigma_t(\mathbf{R_0} - r\,\mathbf{\Omega})\, \psi(\mathbf{R_0} - r\,\mathbf{\Omega}) \right) = e^{-T(r)}\, q(\mathbf{R_0} - r\,\mathbf{\Omega}). \tag{2.43}$$

The left-hand side (LHS) of the above equation, is the result of a product and chain rule:

$$e^{-T(r)}\left(\frac{d\,\psi(\mathbf{R_0}-r\,\mathbf{\Omega})}{d\,(\mathbf{R_0}-r\,\mathbf{\Omega})}+\Sigma_t(\mathbf{R_0}-r\,\mathbf{\Omega})\,\psi(\mathbf{R_0}-r\,\mathbf{\Omega})\right)= \\ e^{-T(r)}\,\frac{d\,\psi(\mathbf{R_0}-r\,\mathbf{\Omega})}{d\,(\mathbf{R_0}-r\,\mathbf{\Omega})}+\Sigma_t(\mathbf{R_0}-r\,\mathbf{\Omega})\,e^{-T(r)}\,\psi(\mathbf{R_0}-r\,\mathbf{\Omega}), \quad (2.44)$$

Now, the chain rule is applied to the derivative in the first term, in reverse:

$$\frac{d\,\psi(\mathbf{R_0}-r\,\mathbf{\Omega})}{d\,(\mathbf{R_0}-r\,\mathbf{\Omega})}=\frac{d\,\psi(\mathbf{R_0}-r\,\mathbf{\Omega})}{d\,(\mathbf{R_0}-r\,\mathbf{\Omega})}\,(-1)\,(-1), \quad (2.45)$$

$$=\frac{d\,\psi(\mathbf{R_0}-r\,\mathbf{\Omega})}{d\,(\mathbf{R_0}-r\,\mathbf{\Omega})}\left(\frac{d\,(\mathbf{R_0}-r\,\mathbf{\Omega})}{dr}\right)(-1), \quad (2.46)$$

$$=(-1)\,\frac{d}{dr}\big(\psi(\mathbf{R_0}-r\,\mathbf{\Omega})\big), \quad (2.47)$$

and for the second term of Equation 2.44, the derivative of the exponential is worked out, in reverse:

$$\frac{d}{dr}\big(e^{-T(r)}\big)=(-1)\,e^{-T(r)}\,\frac{d}{dr}\big(T(r)\big), \quad (2.48)$$

$$=(-1)\,e^{-T(r)}\,\frac{d}{dr}\Big(\int_0^r\Sigma_t(\mathbf{R_0}-r'\mathbf{\Omega})\,dr'\Big), \quad (2.49)$$

$$=(-1)\,e^{-T(r)}\,\Sigma_t(\mathbf{R_0}-r\,\mathbf{\Omega}), \quad (2.50)$$

where the Fundamental Theorem of Calculus was used between the second and third steps. Using Equations 2.47 and 2.50 in Equation 2.44, and taking the reverse of the product rule:

$$e^{-T(r)}(-1)\frac{d}{dr}\big(\psi(\mathbf{R_0}-r\,\mathbf{\Omega})\big)+(-1)\,\frac{d}{dr}\big(e^{-T(r)}\big)\,\psi(\mathbf{R_0}-r\,\mathbf{\Omega})= \\ -\frac{d}{dr}\big(e^{-T(r)}\,\psi(\mathbf{R_0}-r\,\mathbf{\Omega})\big). \quad (2.51)$$

Now, recall Equation 2.43 and substitute what was found for the LHS in Equation

2.51:

$$-\frac{d}{dr}\Big(e^{-T(r)}\,\psi(\mathbf{R_0}-r\,\mathbf{\Omega})\Big) = e^{-T(r)}\,q(\mathbf{R_0}-r\,\mathbf{\Omega}), \tag{2.52}$$

and integrating on both sides yields:

$$-\int_0^\infty \frac{d}{dr}\Big(e^{-T(r)}\,\psi(\mathbf{R_0}-r\,\mathbf{\Omega})\Big)dr = \int_0^\infty e^{-T(r)}\,q(\mathbf{R_0}-r\,\mathbf{\Omega})dr, \tag{2.53}$$

then, using the Fundamental Theorem of Calculus on the left side of the above equation:

$$-\int_0^\infty \frac{d}{dr}\Big(e^{-T(r)}\,\psi(\mathbf{R_0}-r\,\mathbf{\Omega})\Big)dr = e^{-T(r)}\,\psi(\mathbf{R_0}-r\,\mathbf{\Omega})\Big|_0^\infty = \psi(\mathbf{R_0}), \tag{2.54}$$

where in the last step the first term goes go zero because Equation 2.42 is integrated over all space, resulting in a $-\infty$ in the exponent. The second term's exponential, $e^{-T(0)} = 1$, since the integral's other endpoint is zero. Finally, incorporating Equation 2.54 into Equation 2.51 results in:

$$\psi(\mathbf{R_0}) = \int_0^\infty q(\mathbf{R_0}-r\,\mathbf{\Omega})\,e^{-T(r)}dr. \tag{2.55}$$

Physically, the above equation indicates that the flux at $\mathbf{R_0}$ is the integral of the neutron source term (from Equation 2.37), q, at any point along the line, attenuated by the material the neutrons travel through to get there.

This is the equation used by Monte Carlo codes to solve the transport equation, in fact, this form of the equation works both with continuous energy (with an integral over energy) and multigroup energy formalisms.

Now, the equation must be put into generational form, first, the source term from

Equation 2.37 is put into Equation 2.55 and the energy group indices are reattached:

$$\psi_g(\mathbf{R_0},\mathbf{\Omega}) = \int_0^\infty e^{-T(r)}\Bigg[\sum_{g'}\int_{\Omega'}\Sigma_{s,g'\to g}(\mathbf{R_0}-r\,\mathbf{\Omega},\mathbf{\Omega'}\to\mathbf{\Omega})\,\psi_{g'}(\mathbf{R_0}-r\,\mathbf{\Omega},\mathbf{\Omega'})\,d\mathbf{\Omega'}+ \frac{1}{k_{\text{eff}}}\sum_{g'}\frac{\chi_{g'\to g}(\mathbf{R_0}-r\,\mathbf{\Omega})}{4\pi}\int_{\Omega'}\nu_{g'}\,\Sigma_{f,g'}(\mathbf{R_0}-r\,\mathbf{\Omega})\,\psi_{g'}(\mathbf{R_0}-r\,\mathbf{\Omega},\mathbf{\Omega'})\,d\mathbf{\Omega'}\Bigg]dr. \quad (2.56)$$

Declaring that all neutrons born into generation n are created due to the fission source in generation $n-1$, the generation notation can be added:

$$\psi_{g,n}(\mathbf{R_0},\mathbf{\Omega}) = \int_0^\infty e^{-T(r)}\Bigg[\sum_{g'}\int_{\Omega'}\Sigma_{s,g'\to g}(\mathbf{R_0}-r\,\mathbf{\Omega},\mathbf{\Omega'}\to\mathbf{\Omega})\,\psi_{g',n}(\mathbf{R_0}-r\,\mathbf{\Omega},\mathbf{\Omega'})\,d\mathbf{\Omega'}+ \frac{1}{k_{\text{eff}}}\sum_{g'}\frac{\chi_{g'\to g}(\mathbf{R_0}-r\,\mathbf{\Omega})}{4\pi}\int_{\Omega'}\nu_{g'}\,\Sigma_{f,g'}(\mathbf{R_0}-r\,\mathbf{\Omega})\,\psi_{g',n-1}(\mathbf{R_0}-r\,\mathbf{\Omega},\mathbf{\Omega'})\,d\mathbf{\Omega'}\Bigg]dr, \quad (2.57)$$

where the multiplication constant, k, is defined as the ratio of neutrons born in the n^{th} generation to the $(n-1)^{\text{th}}$ generation. This is the equation that KENO V.a solves to determine angular fluxes, angle-integrated fluxes, reaction rates, and the fission source for the next generation, among many other things, in various sub-regions in the model.

The Monte Carlo method is a very powerful way to solve the neutron transport equation, though accuracy at the cost of speed is its main drawback. The KENO V.a multi-group Monte Carlo code was used in the journal article [24] described in Section 4. Another method of solving the neutron transport equation is now presented.

2.1.4 Method of Characteristics

The method of characteristics (MOC), employed by the deterministic code NEWT included in the SCALE 6.1 package, can be solved without choosing a specific coordinate system (i.e. Cartesian, cylindrical or spherical), which makes it attractive to model and solve complex geometries [43], like Monte Carlo codes. The main advantage over other

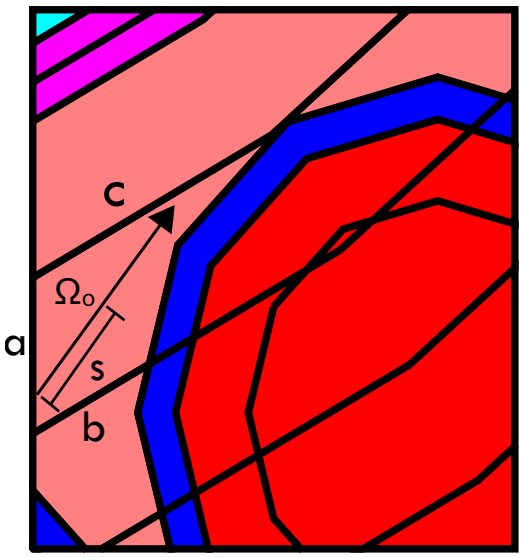

Figure 2.3: A characteristic line near an SCWR fuel pin.

non-Monte Carlo codes is that MOC can solve the transport equation in non-orthogonal geometries. Through cylinders cannot be exactly used, very good approximations can be made when cylinders are replaced by a large number of connected straight sides.

The method used to solve the transport equation shown in Equation 2.1 is through the use of a set of characteristic lines which cross the geometry from one surface to the next. This simplification removes the ∇ operator, which would normally vary depending on the coordinate system, and replaces it by d/ds, the derivative along a characteristic line:

$$\nabla \cdot \mathbf{J}(\mathbf{r}, \mathbf{\Omega}, E) = \nabla \cdot \big(\psi(\mathbf{r}, \mathbf{\Omega}, E)\, \mathbf{\Omega}\big) = \frac{d\psi(s, E)}{ds}, \tag{2.58}$$

where s is the position along a characteristic line, as shown in Figure 2.3, and the first step made use of the product rule, as was done in Equation 2.39).

Since s in Equation 2.58 has a specific direction, the angular dependence of the flux

can be removed and the transport equation, along the characteristic, becomes:

$$\frac{d\psi(s,E)}{ds} + \Sigma_s(s, E \to E')\,\psi(s,E) + \Sigma_a(s,E)\,\psi(s,E) = \int_0^\infty \Sigma_s(s, E' \to E)\,\psi(s,E)\,dE' + \chi(s,E)\int_0^\infty \nu(E')\,\Sigma_f(s,E')\,\psi(s,E')\,dE' + S(s,E). \quad (2.59)$$

The total cross section cleans up Equation 2.59; the neutron source term, Q, similar to that in Equation 2.37, is the RHS of Equation 2.59, which encompasses fission, scattering-in, and any external neutron sources:

$$Q(s,E) = \int_0^\infty \Sigma_s(s, E' \to E)\,\psi(s,E)\,dE' + \chi(s,E)\int_0^\infty \nu(E')\,\Sigma_f(s,E')\,\psi(s,E')\,dE' + S(s,E), \quad (2.60)$$

which leaves:

$$\frac{d\psi(s,E)}{ds} + \Sigma_t(s,E)\,\psi(s,E) = Q(s,E). \quad (2.61)$$

Note that the fluxes in Equation 2.60 can be absorbed into the source term $Q(s,E)$ since they depend on E' rather than E. Equation 2.61 is a linear first-order non-homogeneous differential equation and has the well known solution of [50]:

$$\psi(s,E) = \frac{1}{e^{\int \Sigma_t(s,E)\,ds}}\left[\int e^{\int \Sigma_t(s,E)\,ds}\,Q(s,E)\,ds + C\right]. \quad (2.62)$$

This equation appears complicated, however once an assumption is made that the total cross section does not change significantly over the characteristic, the integrals in

the exponential terms disappear, and the equation is reduced to:

$$\psi(s,E) = C\, e^{-\Sigma_t(E)\, s} + e^{-\Sigma_t(E)\, s} \int e^{\Sigma_t(E)\, s}\, Q(s,E)\, ds, \tag{2.63}$$

where C is dependent on the boundary condition and is replaced by the constant ψ_0 [43, 51]. In order to further simplify the problem, a similar assumption is made that the source $Q(s,E)$ remains constant over the cell in question. In addition, the angular dependence of the flux is also assumed to be constant over the cell. However, the characteristic lines are how the angular flux is tracked, rather than a dependence on Ω. The approximations regarding the cross sections hold as long as material boundaries coincide with computational boundaries. While the angular flux approximation holds providing the computational cells are sufficiently small. At this point, the method being used to solve the transport equation is now considered the step characteristic method (SCM). Returning to Equation 2.63 and integrating with the above defined approximations leads to [43]:

$$\psi(s,E) = \psi_0 e^{-\Sigma_t(E)\, s} + \frac{Q(E)}{\Sigma_t(E)}[1 - e^{-\Sigma_t(E)\, s}], \tag{2.64}$$

which is the flux at any point along a characteristic line.

Choice of Characteristic Lines

As mentioned above, using MOC, the transport equation is solved along lines also known as characteristics. In order to achieve a more accurate flux solution, additional lines and directions must be used. The directions of the lines are based on a quadrature set that discretizes the angular flux.

Figure 2.3 shows a zoomed-in portion of an SCWR fuel lattice cell in which the flux is to be determined. The straight lines in the figure approximate cylinders and make up the radial meshing. Firstly, assume the flux is known on sides a and b, either from an adjacent cell calculation, or from a boundary condition. The known scalar flux is treated

as constant along the length of a. The line denoted Ω_0 is one of many characteristics, has length s, originates on side a, and ends on side c. Equation 2.64 is solved for Ω_0, along with all other characteristics, in all directions, for all cells in the model (not shown in the figure). Once all the fluxes have been solved along the characteristics, the scalar flux for the cell can be used to update the value of the source term, Q, in Equation 2.64. This process is then repeated until all scaler fluxes converge [43].

All characteristics that end on c originating from all other known sides are integrated along the length of c and divided by its length to produce an average angular flux. The components of the angular flux are the contributions from each of the different characteristic line directions. The angular flux along a side can also be integrated to determine the cell boundary's average scalar flux. The same procedure is repeated for the remaining unknown sides. Once all the average angular fluxes on all boundaries of the cell have been determined, the cell's average angular flux can be calculated.

* * *

A number of ways have been presented to solve the Boltzmann neutron transport equation. First, a very approximate and rapid method was introduced and is discussed in further details in Chapter 5. Second, an extremely accurate, but time consuming, Monte Carlo method was derived and is again used in the article presented in Chapter 4. And finally, a deterministic, but still accurate, numerical method of solving a 2-D fuel lattice cell was shown, which was used in the work shown in Chapter 3.

Now that different ways of determining the flux have been explored, the following sections describe how those fluxes can be used to determine sensitivities, similarities, and simulation biases.

2.2 Sensitivity Analysis

In basic terms, sensitivity refers to how much an integral response changes when an individual parameter is perturbed. This definition implies sensitivity is a derivative and if normalized to two variables of interest has the form:

$$S_{a,b} = \frac{b}{a}\frac{\partial a}{\partial b}, \tag{2.65}$$

where a and b are any two variables.

In nuclear engineering, an integral response function that is commonly calculated is k_{eff}. For this reason it is common to determine the sensitivity of k_{eff} to nuclear data, interestingly enough, it is not so common to determine the sensitivity of k_{eff} with respect to a system's model parameters. Model parameters can be anything from wall thickness, moderator temperature, or material composition, and do not directly relate to cross sections or other microscopic nuclear data. Because of the context of this work, nuclear data sensitivities will be discussed in further detail[11], and are defined as [33]:

$$S_{k,\Omega^i_{x,g}} = S^i_{x,g} = \frac{\Omega^i_{x,g}}{k}\frac{\partial k}{\partial \Omega^i_{x,g}}, \tag{2.66}$$

where $\Omega^i_{x,g}$ refers to general nuclear data, not only cross sections (e.g., average fission yield). The variables x, g, and i, refer to reaction type, energy group, and isotope, respectively. For the purposes of clarity, the subscripts k and Ω will be supressed. Furthermore, although all reactions take place a some location r within the model, the variable is dropped.

The SCALE 6.1 simulation suite [3] has been used to perform sensitivity calculations (along with uncertainty, similarity, and bias calculations) in some of the works presented in this thesis. Within SCALE the SAMS module [36] employes the adjoint-based pertur-

[11] With similar treatment the method can be extended to model parameter sensitivities

bation method to calculate nuclear data sensitivities.

2.2.1 Adjoint-Based Perturbation Theory

In perturbation theory, the Boltzmann equation is treated as a linear algebra problem, where the flux is the eigenvector (or eigenstate) and $\lambda = 1/k_{\text{eff}}$ is the eigenvalue. Using this method, sensitivities are found through the derivative of the multiplication and loss operators with respect to nuclear data, rather than their direct perturbation.

Using Bra-Ket notation to express the loss, L, and multiplication, M, operators a balance equation that expresses the transport equation can be written as:

$$|L\psi\rangle = \frac{1}{k} |M\psi\rangle . \tag{2.67}$$

Similarly, the adjoint based equation can be written as:

$$\left|L^{\dagger}\psi^{\dagger}\right\rangle = \frac{1}{k} \left|M^{\dagger}\psi^{\dagger}\right\rangle . \tag{2.68}$$

The following must also be true:

$$|L'\psi'\rangle = \frac{1}{k'} |M'\psi'\rangle , \tag{2.69}$$

where:

$$L' = L + \Delta L,$$

$$M' = M + \Delta M,$$

$$k' = k + \Delta k,$$

$$\psi' = \psi + \Delta\psi.$$

If the perturbations are put into Equation 2.69:

$$|(L+\Delta L)(\psi+\Delta\psi)\rangle = \frac{1}{k'}\,|(M+\Delta M)(\psi+\Delta\psi)\rangle\,, \tag{2.70}$$

the expansion, yields:

$$|L\psi\rangle + |L\Delta\psi\rangle + |\Delta L\psi\rangle + |\Delta L\Delta\psi\rangle = \frac{1}{k'}\big(\,|M\psi\rangle + |M\Delta\psi\rangle + |\Delta M\psi\rangle + |\Delta M\Delta\psi\rangle\,\big). \tag{2.71}$$

Any term with two perturbations can be considered negligible, as they are doubly small, which eliminates the end terms on the RHS and LHS:

$$|L\psi\rangle + |L\Delta\psi\rangle + |\Delta L\psi\rangle = \frac{1}{k'}\big(\,|M\psi\rangle + |M\Delta\psi\rangle + |\Delta M\psi\rangle\,\big). \tag{2.72}$$

The reactivity, ρ, is a measure of how far from critical a system is, and is defined as:

$$\rho = 1 - \frac{1}{k}, \tag{2.73}$$

furthermore, one can find the difference in ρ between two multiplication constants k and k':

$$\Delta\rho = \rho' - \rho = \left(1 - \frac{1}{k'}\right) - \left(1 - \frac{1}{k}\right) = \frac{1}{k} - \frac{1}{k'}, \tag{2.74}$$

therefore,

$$\frac{1}{k'} = \frac{1}{k} - \Delta\rho. \tag{2.75}$$

Now, inserting the above equation into Equation 2.72 and expanding yields:

$$|L\psi\rangle + |L\Delta\psi\rangle + |\Delta L\psi\rangle = \frac{1}{k}|M\psi\rangle + \frac{1}{k}|M\Delta\psi\rangle + \frac{1}{k}|\Delta M\psi\rangle - \Delta\rho\,|M\psi\rangle - \Delta\rho\,|M\Delta\psi\rangle - \Delta\rho\,|\Delta M\psi\rangle\,. \quad (2.76)$$

Immediately it can be seen that the first term on the first and second lines are the equality from Equation 2.67 and can be removed. Additionally, as before the final term on the third line has doubly perturbed quantities and can be neglected. Now, if the adjoint flux is multiplied on the left side, further terms can be reduced.

$$\langle\psi^\dagger|L\Delta\psi\rangle + \langle\psi^\dagger|\Delta L\psi\rangle = \frac{1}{k}\langle\psi^\dagger|M\Delta\psi\rangle + \frac{1}{k}\langle\psi^\dagger|\Delta M\psi\rangle - \Delta\rho\,\langle\psi^\dagger|M\psi\rangle\,. \quad (2.77)$$

$M^\dagger$ and $L^\dagger$ are the Hermitian adjoints of the M and L operators [36] which means the following is true:

$$\langle\psi^\dagger|L\Delta\psi\rangle = \langle L^\dagger\psi^\dagger|\Delta\psi\rangle\,, \quad (2.78)$$

$$\langle\psi^\dagger|M\Delta\psi\rangle = \langle M^\dagger\psi^\dagger|\Delta\psi\rangle\,, \quad (2.79)$$

which turns Equation 2.77 into:

$$\langle L^\dagger\psi^\dagger|\Delta\psi\rangle + \langle\psi^\dagger|\Delta L\psi\rangle = \frac{1}{k}\langle M^\dagger\psi^\dagger|\Delta\psi\rangle + \frac{1}{k}\langle\psi^\dagger|\Delta M\psi\rangle - \Delta\rho\,\langle\psi^\dagger|M\psi\rangle\,, \quad (2.80)$$

then using Equation 2.68 the first term on the LHS and RHS are eliminated, which leaves:

$$\langle\psi^\dagger|\Delta L\psi\rangle = \frac{1}{k}\langle\psi^\dagger|\Delta M\psi\rangle - \Delta\rho\,\langle\psi^\dagger|M\psi\rangle\,. \quad (2.81)$$

The above equation can finally be rearranged to find the change in reactivity, due to a

change in M and L:

$$\Delta\rho = \frac{\left\langle \psi^\dagger \middle| (\frac{\Delta M}{k} - \Delta L)\psi \right\rangle}{\langle \psi^\dagger | M\psi \rangle}. \tag{2.82}$$

2.2.2 Explicit Sensitivity

Now that an equation has been obtained describing the change in reactivity, it is possible to convert Equation 2.82 into a sensitivity, using $\rho = 1 - 1/k$ and $\Delta\rho \approx d\rho = dk/k^2$. Therefore, the sensitivity of k, due to a change in nuclear data Ω is:

$$S_{k,\Omega} = \frac{\Omega}{k}\frac{dk}{\partial\Omega} = \frac{\Omega\, k\, \Delta\rho}{\partial\Omega} = \Omega\, k\, \frac{\left\langle \psi^\dagger \middle| \left(\frac{1}{k}\frac{\Delta M}{\partial\Omega} - \frac{\Delta L}{\partial\Omega} \right)\psi \right\rangle}{\langle \psi^\dagger | M\psi \rangle}. \tag{2.83}$$

and is the method SAMS uses to compute multiplication constant sensitivities. When implementing Equation 2.83 with a specific flux solver additional complications arise because of the need to determine scalar and angular fluxes through the discrete ordinates formulation of flux, however, that discussion is outside the scope of this work (additional details in [36]). The sensitivities discussed up to this point were explicit sensitivities that are due to perturbations of group-wise cross sections and other nuclear data. An additional effect on other cross sections must be considered when a particular cross section is perturbed and is described in the following section.

2.2.3 Implicit Sensitivity

Explicit sensitivities must be accompanied by an implicit component, where the total sensitivity is written as follows [20]:

$$\left(S^i_{x,g}\right)_{\text{total}} = \left(S^i_{x,g}\right)_{\text{explicit}} + \left(S^i_{x,g}\right)_{\text{implicit}}. \tag{2.84}$$

Implicit sensitivities arise from resonance self-shielding effects that occur in group-

wise nuclear data, and simply speaking is the effect of one perturbed cross section on another. This effect can easily be described by the following equation:

$$\left(S^i_{k,\Sigma_{x,g}}\right)_{\text{implicit}} = \sum_j \sum_h S^j_{k,\Sigma_{y,h}} S^i_{\Sigma^j_{y,h},\Sigma_{x,g}}. \tag{2.85}$$

where x and y are reactions, i and j are isotopes, and g and h are energy groups. The equation states that if the cross section in question ($\Sigma^i_{x,g}$) changes as a result of a different cross section ($\Sigma^j_{y,h}$) being varied, then these effects must be summed over all reactions, isotopes, and energy groups.

All cross sections discussed in this section, and used in SCALE 6.1, are derived using Bondarenko's method [36, 52]. This technique accounts for self shielding effects by weighting a nuclide's cross section by a "background" cross section term. The background cross section is the sum of all other macroscopic cross sections in the medium, weighted by the number density of the isotope in question. One can think of the background term as the extent to which an isotope is diluted in a mixture.

Other types of sensitivities can be calculated as well, such as the change in k_{eff} with respect to, for instance, fuel temperature, moderator temperature, or coolant density. These sensitivities are commonly referred to reactivity coefficients and are calculated with respect to model parameters that may change during transients and will also give rise to uncertainties in k_{eff}. In practice, for these types of sensitivities a direct perturbation method is preferred over the adjoint-based perturbation method.

This section has provided an overview of sensitivity analysis and will be used in the following section to calculate the uncertainty in k_{eff}.

2.3 Uncertainty

The importance of uncertainty analysis in the nuclear industry may be somewhat underestimated. Many reports and journal publications do not provide any kind of uncertainty information, unless specifically investigating the effects of uncertain nuclear data on integral responses like k_{eff} (see [53–55]).

This puts into question the accuracy of calculations made by nuclear simulation codes, unless those simulations are directly compared to benchmarks. Uncertainty assessments are extremely important in safety analysis, accident scenario analysis, safety margin assessments, and in the development of new reactors. Knowing the uncertainty in integral responses is also important to minimizing waste and optimizing reactor economics [56].

The different types of uncertainties that affect simulations were touched on in Section 1.1 and are explain in more detail here below. They are classified into types A, B, and C, depending on their nature. Class-A uncertainties are classified as methods uncertainties, Class-B are modelling and experimental uncertainties, and Class-C are specifically nuclear data uncertainties.

1. Numerical Uncertainties (Class-A) - these aleatoric uncertainties are approximations to the numerical methods and theories that are implemented in simulation codes, in order to decrease the requirement for computational resources. This type of uncertainty is very difficult to estimate because they can have a range of effects on different models.

2. Statistical Uncertainties (Class-A) - these types of uncertainties arise when using random numbers to simulate phenomena. For example, Monte Carlo simulations follow a relatively small number of neutrons when compared to a reactor core. The neutrons are subject to random numbers generated in a code to determine how far they will travel, in which direction, and how they will react. Increasing the number of neutrons will decrease the statistical uncertainty in a similar fashion

to the standard deviation of a mean being proportional to $1/\sqrt{N}$ where N is the number of samples.

3. Modelling Uncertainties (Class-B) - these are uncertain geometrical and material composition variables such as fuel thickness, moderator height, pressure tube thickness, and composition uncertainties (e.g., fuel weight percent, moderator purity and boron concentration). These also fall into the epistemic category. Typically, nominal design values are used in simulations during the development phase, however, after operation begins, accurate physical measurements of geometries are difficult to acquire, if not impossible due to radiation fields. Typically, each station has "as built" general arrangement drawings and operational drawings, however these would only include nominal measurements and likely would not have associated uncertainty information.

4. Nuclear Data Uncertainties (Class-C) - these epistemic uncertainties represent the lack of knowledge of nuclear data parameters such as microscopic cross sections $\sigma(E)$, fission energy spectra $\chi(E)$, and reproduction factor η.

2.3.1 Numerical and Statistical Uncertainties (Class-A)

The most obvious uncertainties that arise from calculation methods are the inherent statistical uncertainties that come from sampling random numbers, such as in the Monte Carlo described in Section 2.1.2. Other approximations such as spatial meshing, energy meshing, use of characteristic, the choice of quadrature sets in discrete ordinate methods, etc, are all considered as calculation method uncertainties. These types of uncertainties are difficult to quantify, as they can affect different models in different ways.

Systematic tolerances may be placed on many of the above listed uncertainties [35]. For example, a geometric mesh can be reduced in size until an asymptotic behavior is observed in the output. Then a systematic tolerance (similar to a bias) can be placed on

a specific sized meshing, and as such are considered class-A uncertainties.

2.3.2 Modelling Uncertainties (Class-B)

On top of geometrical and material composition uncertainties listed above, this category also includes uncertainties due to direct computation simplifications such as interpolating between cross section libraries for a specific temperature. Also, uncertainties due to homogenization and energy discretization fall into this class.

The 2011 International Handbook of Evaluated Reactor Physics Benchmark Experiments [57] is an excellent source of finding model parameter uncertainties. A very large number of benchmark experiments are listed, in extremely fine detail. Moreover, since the experiments/simulations were all submitted using the same evaluation guidelines, the information is mostly consistent. Essentially any uncertain model information, their sensitivities, and their uncertainties to k_{eff}, can be found there.

One of the benchmarked reactors in the handbook is the ZED-2 critical facility. By varying only ten parameters, namely: pressure tube composition, fuel cladding composition, fuel composition, ^{235}U abundance, fuel density, pressure tube wall thickness, calandria tube outer diameter and thickness, moderator and coolant purity, and moderator height, a total uncertainty $\delta k_{\text{eff}} = 3.09\,\text{mk}$ was found. Similar results were also found in other reactor benchmarks. This is of high importance because the uncertainty for an accident case may be greater than the delayed neutron fraction, in which case the reactor may become prompt critical.

In another study [58], an uncertainty analysis was performed to determine the confidence of k_{eff} in a cylindrical concrete nuclear materials storage container. Various model parameters such as: ^{235}U enrichment, UF_6 density, cylinder inner diameter, cylinder wall thickness, concrete density and porosity, were varied. All variables were varied within a 5% range, relative to their mean. This resulted in $k_{\text{eff}} = 0.837 \pm 0.028$ ($\Delta k/k = 3.3\%$)

[$\rho = -196 \pm 40$ mk]. These are very large multiplication constant uncertainties and are solely due to model parameters. In this case however, although the uncertainty is large, the system is safely subcritical. On the other hand, if the result yielded a k_{eff} closer to 1, the margin of safety may have been impinged upon. Care should be taken to correctly describe the uncertainties of model parameters as 5% for all of them is an assumption may lead to an underestimation or overestimation of the uncertainty in k_{eff}.

These two examples show the importance of uncertain model parameters. Depending on the type of study being performed for example: criticality safety, approach to criticality, or fuel exit burnup, different levels of uncertainty are required.

2.3.3 Nuclear Data Uncertainty

Evaluated nuclear data, such as cross sections, fission spectra, delayed neutron yields, and neutron emission per fission, all have inherent uncertainties. These uncertainties arise from experimental measurements and the methods used to extract cross sections from those measurements, as do any experimental quantities.

To complicate the matter, neutrons are sensitive to the number of neutrons and protons in a mixture, not only the atomic number. This is an issue for experimentation because it's essentially impossible to completely separate isotopes in samples containing heavy elements, such as U or Pu. Therefore, when an experiment is performed to determine the ^{235}U fission cross section, the uncertainty in the amount of ^{238}U must also be considered. This is one way in which covariances arise.

In nuclear systems, be they lattice cells or full cores, an extremely large number of variables are at play, and many of the input parameters are correlated. In order to perform an uncertainty study using sensitivity data, an uncertainty matrix containing information of the covariance and variance between tabulated nuclear data is needed.

A multi-group cross section covariance library is included with the SCALE 6.1 simu-

lation suite. This evaluated covariance library is a compilation of data from many sources including the ENDF/B-VII, ENDF/B-VI, and JENDL-3.3 libraries, and from a collaborative uncertainty project performed by Brookhaven National Laboratory, Los Alamos National Laboratory and Oak Ridge National Laboratory [59].

The $M \times M$ dimension relative covariance matrix[12] is labelled as $\mathbf{C_{\Omega\Omega}}$, where M is the number of nuclide-reaction pairs[13]. In mathematical form, the elements of the relative covariance matrix $C_{\Omega\Omega}$ are [36]:

$$[\mathbf{C}_{\mathbf{\Omega^i_{x,g}\Omega^i_{y,g'}}}] = \frac{\mathrm{COV}(\Omega^i_{x,g},\, \Omega^i_{y,g'})}{\Omega^i_{x,g}\Omega^i_{y,g'}}, \tag{2.86}$$

where $\Omega^i_{x,g}$ refers to uncertain nuclear data.

A sensitivity vector $\mathbf{S_k}$ with dimensions $1 \times M$ is filled with elements as shown in Equation 2.66. The total variance of k_{eff} can then be calculated as:

$$\sigma_k^2 = \mathbf{S_k C_{\Omega\Omega} S_k^T}, \tag{2.87}$$

where the T superscript indicates the transpose of the $\mathbf{S_k}$ vector.

The entries in of $\mathbf{S_k}$, $\mathbf{C_{\Omega\Omega}}$, and $\mathbf{S_k^T}$ can also be multiplied element-wise to produce the individual uncertainty contributions to k_{eff}. As mentioned before, given proper treatment this method can also be extended to model parameter uncertainties. Additionally, individual reaction variances and reaction-reaction covariances can be determined by doing element-wise multiplication.

Reaction variances and reaction-reaction covariances can be used to determine which isotopes, reactions, and energy groups contribute to the total uncertainty in the system. Since some covariances can be negative, this can provide valuable insight into how to

[12]The relative covariance matrix $\mathbf{C_{\Omega\Omega}}$ is known as $\mathbf{C}_{\alpha\alpha}$ in literature. However, for consistency in notation, Ω is used over α in this thesis.

[13]An example of a nuclide-reaction pair is: $\sigma^i_{f,g} \times \sigma^j_{a,h}$ where the f and a refer to the fission and absorption cross sections of nuclides i and j, in energy groups g and h, respectively.

adjust system components to reduce the total uncertainty. Moreover, the study identifies the largest uncertainty contributors and enables researchers to perform additional experiments to reduce those uncertainties.

2.4 Similarities and Completeness

Similarity studies attempt to quantify how similar a set of systems are, with respect to some calculable value. Since similarity is a general term and has no precise meaning, three main integral indices, c_k, E, and G, all with slightly different definitions, have been developed for the purpose of nuclear systems. Which one to use depends on the context, and each are explained in detail in Chapters 3 and 4. To avoid repetition, the details are not explained here.

Another parameter, called the completeness, provides a measure of how a set of experiment's sensitivities are similar (either equal or larger) to an application's sensitivities. This parameter attempts to quantify how the set of benchmark's sensitivities cover the application's sensitivities [20, 36]. A detailed explanation of the completeness parameter can be found below and a brief description is repeated in Chapter 4.

$$R = \frac{S_a}{S_t}, \tag{2.88}$$

where:

$$S_a = \sum_n \sum_x \sum_j |dS_{x,j}^{a,n}|, \tag{2.89}$$

$$S_t = \sum_n \sum_x \sum_j |S_{x,j}^{a,n}|, \tag{2.90}$$

and

$$d = \begin{cases} 1, & \text{if } N_{x,j}^{n} \geq n_{\text{lim}} \\ 0, & \text{otherwise.} \end{cases} \tag{2.91}$$

An explanation of the variables follows:

e, a - experiment and application.

R - the completeness parameter where $0 \leq R \leq 1$. A value of 1 indicates all sensitivities in the application are covered by *larger*[14] sensitivities in the benchmark experiments.

$N_{x,j}^{n}$ - the number of systems with $S_{x,j}^{e,n} > |f \times S_{x,j}^{a,n}|$. This compares the sensitivities $S_{x,j}^{a,n}$ of the same nuclide n, reaction x and energy group j in all systems involved.

n_{lim} - the minimum number of experiments[15] that have $S_{x,j}^{e,n} > |f \times S_{x,j}^{a,n}|$ before including the sensitivity in the sum for the completeness parameter calculation. This number is an integer.

f - the sensitivity factor[16] is a multiplier used to reduce the sensitivity magnitude required by an experiment in order to be included in calculations of R. Additionally, $0.0 < f < 1.0$.

With a high completeness parameter (and correct factors), one can be sure that the majority of application sensitivities are covered by the sensitivities that arise in the set of benchmark experiments used in the study. This indicates the set of experiments is adequate to perform a simulation bias calculation for the application.

[14] Larger refers to the inequality in the description of $N_{x,j}^{n}$.
[15] n_{lim} is sometimes referred to as *nixlim*.
[16] The sensitivity factor, f, is sometimes referred to as *senfac*.

2.5 Nuclear Data Adjustment: Generalized Least Squares Method

Much of the work performed for this thesis (Chapters 3 and 4) describes methodologies and results that are required prior to determining an application's simulation biases. Although a nuclear data adjustment and bias determination were not performed in any of the work herein, it is considered the next step in the reactor physics evaluation of a new reactor design. Therefore, the data adjustment procedure and bias calculation is introduced and explained below, for thoroughness.

A nuclear data adjustment can be performed by the TSURFER module [35] in the SCALE simulation suite, using the Generalized least squares (GLLS) method. For nuclear applications, it was developed in the 1970s and 1980s based on sensitivity and uncertainty techniques. It was originally intended for applications such as nuclear data evaluation [60], fast reactor design [37, 61], and for the prediction of reactors' pressure vessel damage [35, 62]. More recently the method has been adopted to criticality assessments.

In principle, a set of already performed experimental benchmarks are modelled and simulated in KENO V.a. The TSUNAMI module is used as the driver for the flux solution (KENO), the sensitivity and uncertainty analysis (SAMS), and the similarity study (TSUNAMI-IP). From SAMS, the nuclear data sensitivities for each isotope, reaction, and energy group are calculated using the adjoint-based perturbation method and tabulated. The same is done for the application of interest and in this case is the SCWR. The GLLS procedure then uses the benchmark set's experimental uncertainties, simulation and application sensitivities, and multiplication constants, to perform a χ^2 reduction (equation given below). The reduction is performed by adjusting nuclear data, within uncertainty, simultaneously across all simulations such that their simulation and experimental multiplication constants become the same, within experimental uncertainty. Although this is a powerful procedure, it does not mean that a nuclear data set exists to simultaneously

produce consistency between all simulation and experimental multiplication constants. This common result is the basis of a simulation bias.

Traditionally, validation studies used meaningful benchmarks that were similar in nature to an application (e.g., similar fuel, temperatures, moderator, coolant, etc). Though this method was very useful, it only provided a rough estimation of simulation biases. Nowadays, analysis frameworks, such as the sensitivity and uncertainty framework included in the SCALE package, provide additional details (i.e., nuclear data sensitivities) that can be used to better predict an application's responses. Essentially, rather than only using experimental multiplication constants, use of the simulations' sensitivities allows a much higher degree of freedom, such that the nuclear data can be individually adjusted to replicate experimental results, and in turn the application's responses as well.

Now that sensitivities and uncertainties have been calculated, and the completeness parameter demonstrates a large sensitivity coverage, a bias calculation can be performed. The value of the bias will indicate the difference in an application's simulated response and experimental response (if it were to be built). The numerical recipe for determining the simulation bias and reducing uncertainties due to nuclear data is now presented. The minimization of χ^2 is written as [20, 35]:

$$\chi^2 = \left[\frac{\Omega' - \Omega}{\Omega}\right]^T \mathbf{C_{\Omega\Omega}}^{-1} \left[\frac{\Omega' - \Omega}{\Omega}\right] + \left[\frac{m' - m}{m}\right]^T \mathbf{C_{mm}}^{-1} \left[\frac{m' - m}{m}\right], \tag{2.92}$$

where:

Ω' - the adjusted nuclear cross sections. The brackets around these terms indicate an element-wise calculation which produces a matrix with the same dimensions as the vector $\mathbf{\Omega'}$.

Ω - the original nuclear cross sections used in simulations used in these calculations.

$\mathbf{C_{\Omega\Omega}}$ - the relative covariance matrix as defined in Section 2.3.3.

m' - the adjusted k_{eff}.

m - the measured k_{eff} from experiments used in the calculations.

$\mathbf{C_{mm}}$ - the experimental error matrix[17]. It is similar to $C_{\Omega\Omega}$, however represents variances and covariances between uncertain experimental quantities, such as: fuel enrichment, impurities, densities [35], material temperatures, and critical dimensions [39], that may be common between experiments. These sorts of covariances become significant when one reactor is used to perform multiple experiments with similar components, such as fuels, measurement techniques, structures, and structural materials. There is no generally accepted method to produce C_{mm}, however, one consistent method is presented in [39].

The χ^2 problem as defined above, in the context of criticality safety, presents some issues. Firstly, the number of degrees of freedom that exist in the nuclear data is enormous. TSUNAMI tracks upwards of 400 isotopes, each with many different possible reactions (i.e., (n,f), (n,γ), (n,2n), (n,3n), (n,n), (n,n'), (n, α), (n,p),... etc.) and, in the case of KENO V.a multigroup (SCALE 6.1), 238 energy groups. What was just described was only the material description, however, the KENO model also has a spatial component where the materials are placed in different amounts throughout the model. Even if an extremely large benchmark set is used, say 500 experiments, the adjustment problem is enormously under-constrained. This can present nonphysical nuclear data alterations, thus additional constraints must be imposed [35]. The method used by TSURFER has three constraints:

1. The adjusted experiment and simulation multiplication constants must stay equal (i.e., $k' = m'$).

[17] Sometimes V_e is used over C_{mm}.

2. All adjustments are made within the uncertainty of the parameter (i.e., $(m' - m) \leq \sigma_m$).

3. Adjustments are also constrained by their correlated partners uncertainties.

Once the adjusted cross sections are found, the changes in responses $\Delta k = S_k \Delta\Omega$ can be found. Then the bias between application and experiment can be found as well:

$$\beta_a = k_a - k'_a(\Omega') \approx -(k_a) S_a^T \Delta\Omega. \tag{2.93}$$

This completes the procedure to calculate the bias between an SCWR application and its simulation. In theory, a set of optimized experiments required to perform a suitable bias calculation (high completeness parameter) can be generated by maximizing the completeness parameter. These experiments could potentially be performed at the ZED-2 critical facility. In order to create this optimized set of experiments, a driver code can be used to consecutively perform simulations in order to maximize R (completeness parameter).

The nuclear data adjustment procedure explicitly uses nuclear data uncertainties (type C) uncertainties, as described at the beginning of Section 2.3, however, implicitly treats modelling uncertainties (type B) as well. The method cannot account for statistical or numerical uncertainties (type A).

Chapter 3

Methodology to Design Simulated Irradiated Fuel by Maximizing Integral Indices (c_k, E, G)

Citation:

J. Sharpe, A. Buijs, and J. Pencer, 2016, "Methodology to Design Simulated Irradiated Fuel by Maximizing Integral Indices (c_k, E, G)," Journal of Nuclear Engineering and Radiation Science, 2 (2), pp. 1-7. doi: 10.1115/1.4031074

This paper introduces a novel method of generating simulated irradiated fuel that can be manufactured for experimentation. The method is novel in the sense that it maximizes the neutronic similarity (via nuclear data sensitivities) of truly irradiated and simulated irradiated fuel by altering the the concentration of benign neutron absorbers which replace fission products that would exist in truly irradiated fuel. This makes the simulated fuel able to be manufactured, rather than it being irradiating for years in a power reactor. It is also safe to handle, and suitable for experimentation. These are all ideal qualities for testing experimental fuels under burnup conditions.

The results of this paper show that the replacement of fission products with Dysprosia can lead to high neutronic similarity. This means that experiments can then be performed on the manufactured simulated fuel and results can be used to reduce nuclear data uncertainties, through a data adjustment. This method allows the improvement of prediction capabilities of reactor physics codes, and aides in the accurate development of new reactors.

Methodology to Design Simulated Irradiated Fuel by Maximizing Integral Indices (c_k, E, G)

Jason R. Sharpe[1]
Department of Engineering Physics,
McMaster University,
Hamilton, ON L8S 4L8, Canada
e-mail: sharpejr@mcmaster.ca

Adriaan Buijs
Department of Engineering Physics,
McMaster University,
Hamilton, ON L8S 4L8, Canada
e-mail: buijsa@mcmaster.ca

Jeremy Pencer
Computational Physics Branch,
Canadian Nuclear Laboratories,
Engineering Physics,
McMaster University,
Deep River, ON K0J 1P0, Canada
e-mail: jeremy.pencer@cnl.ca

*Critical experiments are used for validation of reactor physics codes, in particular, to determine the biases and uncertainties in code predictions. To reflect all conditions present in operating reactors, plans for such experiments often require tests involving irradiated fuel. However, it is impractical to use actual irradiated fuel in critical experiments due to hazards associated with handling and transporting the fuel. To overcome this limitation, a simulated irradiated fuel, whose composition mimics the neutronic behavior of the truly irradiated fuel (TRUFUEL), can be used in a critical experiment. Here, we present an optimization method in which the composition of simulated irradiated fuel for the Canadian supercritical water-cooled reactor (SCWR) concept at midburnup (*21.3 $\mathrm{MWd\,kg^{-1}}$ *(IHM)) is varied until the integral indices c_k, E, and G are maximized between the true and simulated irradiated fuel. In the optimization, the simulated irradiated fuel composition is simplified so that only the major actinides (*^{233}U, $^{238\text{-}242}$Pu, *and* ^{232}Th*) remain, while the absorbing fission products are replaced by dysprosia and zirconia. In this method, the integral indices c_k, E, and G are maximized while the buckling, k_∞ and the relative ring-averaged pin fission powers are constrained, within a certain tolerance, to their reference lattice values. Using this method, maximized integral similarity indices of $c_k = 0.967$, $E = 0.992$, and $G = 0.891$ have been obtained.* [DOI: 10.1115/1.4031074]

1 Introduction

Determination of simulation biases and uncertainties is becoming increasingly important in the conceptualization, design, and licensing of new critical assemblies as well as in the continuing operation of existing facilities. For that reason, an understanding of fuel performance at midburnup (or any burnup) is needed; however, difficulties associated with using irradiated fuel, due to restrictions placed by international treaties, transportation issues, and handling hazards, motivate the use of simulated fuel (SIMFUEL) that neutronically mimics the TRUFUEL instead.

When mimicking the TRUFUEL, a number of neutronic responses can be used to describe the similarity of two fuels, i.e., the multiplication constant (k_∞), flux spectra, fission powers, buckling (B^2), nuclear data sensitivities ($S_{k,\alpha}$), reactivity coefficients, and others. Although no SIMFUEL exactly matches a corresponding TRUFUEL without having all the original isotopes included at their respective number densities, its neutronic responses can be approximated by replacing the built-in absorbing fission products with a small number of absorbing (or moderating) isotopes. By using gradually more isotopes, the SIMFUEL's and TRUFUEL's neutronic responses will become increasingly similar. However, the availability of certain isotopes limits the isotopic options; also, by increasing the complexity of the SIMFUEL (i.e., adding more isotopes), finding optimal solutions becomes more computationally expensive, as the optimizing algorithm has a larger parameter space to cover.

Although much research exists in designing SIMFUEL for investigating its chemical properties, there is little literature in the way of designing SIMFUEL for neutronic purposes, most likely because of the low availability and high usage costs of experimental reactors. In this study, a method is introduced to design a SIMFUEL's isotopic composition, which will attempt to spark research regarding SIMFUELs and fill the void in the literature. As the main purpose of this methodology is to select a SIMFUEL for nuclear data adjustment and bias calculation, the similarity of the global integral indices c_k, E, and G is maximized; meanwhile, certain lattice parameters B^2, inner-, and outer-ring-averaged pin fission powers (P_i and P_o, respectively) and k_∞ are constrained to mimic the TRUFUEL's neutronic behavior.

1.1 Sensitivity, Uncertainty, and Similarity.

To determine the three global integral indices c_k, E, and G (defined below), a lattice cell-based calculation to find the cell's nuclear data sensitivities is first required. The Scale 6.1 simulation suite [1], developed at Oak Ridge National Laboratories, includes the Sensitivity Analysis Module for Scale (SAMS) [2] module that calculates the system's nuclear data sensitivities using the adjoint-based perturbation method [3,4]. The adjoint-based method calls for the cell's forward and adjoint fluxes, which is accomplished using the deterministic neutron transport code NEWT [5] (also included in Scale 6.1). SAMS produces explicit sensitivities, which represent the sensitivity of k to the perturbation of resonance self-shielded multigroup nuclear data

$$S_{k,\alpha} = \frac{\alpha}{k}\frac{\partial k}{\partial \alpha} \tag{1}$$

where k is the multiplication constant and α is a nuclear data component (i.e., energy-, reaction-, and nuclide-specific cross sections (Σ_j), fission spectra (χ), and the number of neutrons emitted per fission (ν)). SAMS also produces implicit sensitivities, which arise from changes in k coming from the effect of perturbing one resonance-shielded cross section on another. The explicit and implicit sensitivities are then added to make the complete sensitivity. The complete sensitivity vector, $\mathbf{S_k}$, is of length M, where M is the number of energy groups multiplied by the number of reactions multiplied by the number of nuclides (refer to Refs. [6–8] for a complete

[1]Corresponding author.

Manuscript received May 8, 2015; final manuscript received July 8, 2015; published online February 29, 2016. Assoc. Editor: Thomas Schulenberg.

discussion and derivation of sensitivities). This sensitivity vector is then combined with a 44 energy group nuclear data covariance matrix, $\mathbf{C}_{\alpha\alpha}$, to produce the system variance σ^2 (refer to Ref. [9] for information on the covariance matrix)

$$\sigma^2 = \mathbf{S_k} \mathbf{C}_{\alpha\alpha} \mathbf{S_k^T} \tag{2}$$

where $\mathbf{S_k^T}$ is the transpose of $\mathbf{S_k}$. Individual group-wise, nuclide-, and reaction-specific variances also can be found by performing element-wise multiplication.

The integral similarity index c_k between systems can then be found by computing the sensitivity vectors for each system, then treating $\mathbf{S_k}$ as an $I \times M$ matrix, where I is the number of systems and multiplying as in Eq. (2) [10,11]. The elements of that matrix give the c_k between systems t (TRUFUEL) and s (SIMFUEL)

$$c_k = \frac{\sigma_{ts}^2}{\sigma_t \sigma_s} \tag{3}$$

This similarity index represents the overlap in the contribution to the total system uncertainty from the group- (g), reaction- (x) and nuclide- (n) specific nuclear data. Physically, c_k can be thought of as an overlap in uncertainty contributions, to the multiplication constant k, between two systems.

Another integral index, E, representing a direct comparison of how similar the sensitivity vectors are between two systems, is calculated as [10]

$$E = \frac{\mathbf{S_s^T S_t}}{|\mathbf{S_s}||\mathbf{S_t}|} \tag{4}$$

where S_s and S_t are the SIMFUEL and the TRUFUEL's sensitivities. Physically, this index can be viewed as a projection of the SIMFUEL's sensitivity vector onto the TRUFUELS's sensitivity vector. In the case where the TRUFUEL's and SIMFUEL's sensitivity vectors are the same, an analog can be made to how two directional vectors pointing in the same direction (i.e., all group- (g), reaction- (x) and nuclide- (n) specific sensitivities in two systems are equal) have their dot product equal to 1, or if the vectors are perpendicular (i.e., g-, x-, and n-specific sensitivities in one system have their matching g, x, and n in another system equal to zero), the dot product is equal to zero.

The final integral index, G, also known as the coverage, is a measure of how much one system's sensitivities are covered by another system's sensitivities, for all the nuclides, reactions, and energy groups. G is calculated as follows [10,12]:

$$G = 1 - \frac{\sum_{n,x,g} S_{n,x,g}^s - S_{n,x,g}^{t'}}{\sum_{n,x,g} S_{n,x,g}^s} \tag{5}$$

with the following constraints:

$$S_{x,g}^{t',n} = \begin{cases} 0, & \text{if } S^s \text{ and } S^t \text{ are opposite signs} \\ S_{x,g}^{s,n}, & \text{if } |S_{x,g}^{t,n}| \geq |S_{x,g}^{s,n}| \\ S_{x,g}^{t,n}, & \text{if } |S_{x,g}^{t,n}| < |S_{x,g}^{s,n}| \end{cases}$$

These constraints ensure that as long as the TRUFUEL's sensitivities are larger than the SIMFUEL's sensitivities, the coverage will be maximized.

It is important to have adequate coverage for performing bias calculations. The level of coverage relates directly to the confidence level with which phenomena (such as CVR) in the power reactor can be predicted on the basis of simulations. As a guideline, a coverage of at least 90% is required for the results of a test experiment to be useful in the design of a power reactor.

Figure 1 shows the ^{239}Pu fission sensitivity profiles for SIMFUEL and TRUFUEL. It can be seen that the SIMFUEL sensitivities are consistently larger than the TRUFUEL's, however, by only a small margin. This results in a $G_{^{239}\text{Pu,fission}} = 0.9995$ for these particular sensitivity profiles, meaning that the SIMFUEL is well covered by the TRUFUEL.

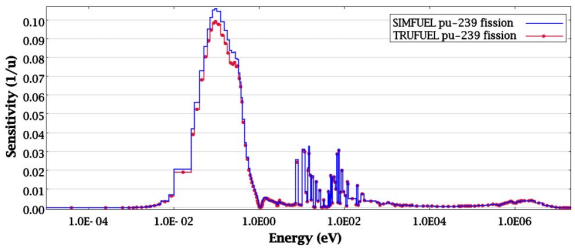

Fig. 1 ^{239}Pu fission sensitivity profiles for SIMFUEL and TRUFUEL. A similarity index of $G_{^{239}\text{Pu,fission}} = 0.9995$ was found between these two profiles

1.2 Model Description. Figure 2 shows the layout of the PT-SCWR fuel lattice cell and was used throughout this study to demonstrate the proposed methodology. Two fuel rings, consisting of 32 pins each, constitute the fissile and breedable materials within the cell. The inner and outer ring of fuel pins have a 15% and a 12% weight PuO_2 in ThO_2 composition, respectively, with a density of 9.91 g/cm^3 and 9.87 g/cm^3, respectively, and radii of 0.415 cm and 0.44 cm, respectively (additional details can be found in Refs. [13–15]). This difference in plutonia content in the inner and outer fuel rings was chosen to balance the radial power profile to provide fairly even power production between the rings (relative ring-averaged fuel pin fission powers of this lattice model as a function of axial height and burnup, for various transport codes, can be found in Ref. [16]). A fuel temperature of 1420.62 K was used for both the inner and outer fuel ring, and the temperature was also uniform across each individual pin.

There are two flows of coolant in this fuel cell: (1) the innermost flow conduit, which consists of light water coolant and flows directly from the inlet plenum at $\rho = \sim$0.62 g/cm^3 and $T = \sim$625 K; and (2) the outer coolant flow conduit, which is composed of the same light water that was in the innermost conduit that has flowed down to the bottom of the 5 m fuel assembly where it is then redirected upward to the outer conduit, which houses the fuel rings. Upon exiting the top of the assembly, in the outer conduit, the light water has $\rho = \sim$0.07 g/cm^3 and $T = \sim$900 K.

A D_2O moderator surrounds the fuel assembly and is held at atmospheric pressure and $T = \sim$342 K with a total cell pitch of 25 cm. Although the principal moderator has just been described, a significant amount of moderation, upscattering, and absorption is also provided by both the upward and downward coolant flow (details of the inner, outer, and total coolant void reactivity for this lattice can be found in Ref. [16]).

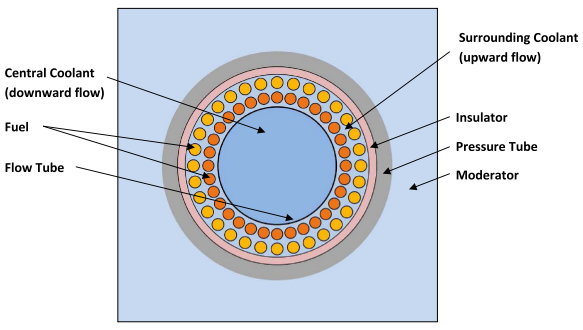

Fig. 2 Cross-sectional view of the 64-element Canadian PT-SCWR fuel bundle concept, channel, and lattice cell

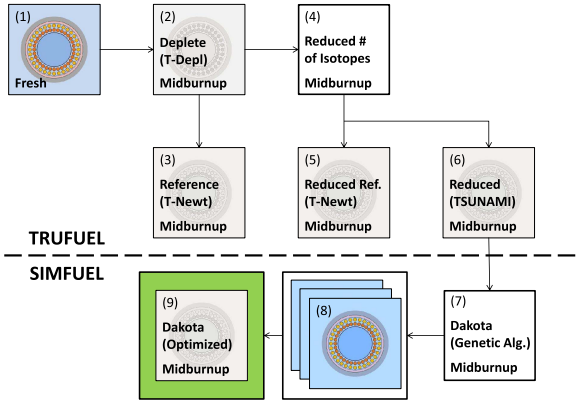

Fig. 3 Methodology used to ensure the validity of comparisons. Above the dashed line indicate TRUFUEL, below the dashed line indicates SIMFUEL

2 Methodology

Before any transport or depletion calculations could be performed, Dancoff factors were needed to properly account for resonance self-shielding effects. Contrary to boiling water and pressurized water reactor designs, which feature a regular geometry of repeating cells [17], the more complicated structure of the SCWR fuel lattice cell (as shown in Fig. 2) is not repeating, nor uniform, thus a 3D Monte Carlo approach was needed to determine the Dancoff factors at midburnup. This was performed using the MCDancoff module [18] within Scale 6.1. For each new calculation within this methodology, new Dancoff factors were found. Due to the similarity of the fuel, and the nature of matching lattice physics parameters, the Dancoff factors for the inner and outer fuel, separately, were found to be identical to nine decimals at each stage of the study. The values determined by MCDancoff were

$$D_{\text{inn.}} = 0.43972 \qquad D_{\text{out.}} = 0.38537 \tag{6}$$

Figure 3 represents the steps used in the determination of the maximized similarity indices and are now described. The deterministic neutron transport code NEWT was used to model the most recent layout of the Canadian PT-SCWR fuel lattice cell and to perform a depletion calculation. A midburnup of 21.3 MWd kg^{-1} (IHM) was chosen to represent a typical midburnup value within a cell. A total of 20 burnup steps were used in the irradiation process for 450 days, with a specific power of 47.3 kW kg^{-1}. The burn-up steps at the beginning of the process were more closely spaced in time as oppose to the end of the irradiation, which were spaced further apart, to capture the effect of short-lived isotopes on burnup. At each burn-up step, NEWT reported the number densities of 388 isotopes, including major and minor actinides, light isotopes, and fission products.

The symmetry of the PT-SCWR fuel lattice cell allowed the use of a one-eighth-cell model, as shown in Fig. 4. The cartesian and radial meshing used to find the forward and adjoint fluxes, needed to calculate the sensitivities in Eq. (1), also can be seen in the figure.

The TSUNAMI-2D code is a driver that uses the SAMS code to calculate sensitivities (i.e., Eq. (1)), which are then sent to TSUNAMI-IP [10] (IP—indices and parameters) to be used in Eqs. (2)–(5) to calculate the similarity indices c_k, E, and G. However, the TSUNAMI-2D sequence cannot accept an input of 388 isotopes; therefore, the isotope list was systematically reduced to adhere to TSUNAMI's constraints: any isotope with a number density below 10^{-9} nuclides $\cdot$ cm^{-1} b^{-1} was excluded, resulting in a reduction in the number of isotopes in the inner and outer fuel rings to 192 each. The list of isotopes along with their respective number densities in the inner and outer fuel rings can be found in

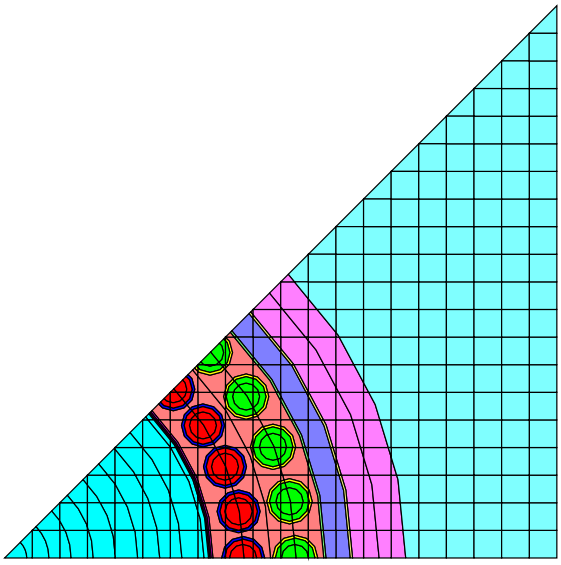

Fig. 4 Radial and Cartesian meshing used in the one-eighth fuel cell modeled with NEWT

Tables 1 and 2. This reduced-reference case of TSUNAMI-2D was compared to the NEWT calculation (using 388 isotopes) to ensure that the removed isotopes did not contribute significantly to important lattice parameters.

To design the SIMFUEL, a number of assumptions were made:

- ^{232}Th would be available.
- ^{233}U would be available by extracting it from irradiated ^{232}Th.
- Only reactor-grade Pu would be available. ^{239}Pu was matched to the number density found in the TRUFUEL, whereas ^{238,240,241,242}Pu were matched to the appropriate reactor-grade Pu weight percentages relative to the ^{239}Pu.
- All other actinides would not be available due to difficulties in acquiring and handling.
- All fission products would be represented by a mixture of dysprosia (Dy_2O_3) and zirconia (ZrO_2).

The SIMFUEL would therefore be composed of ^{232}Th, ^{233}U, reactor-grade Pu, and a mixture of dysprosia and zirconia. The amounts of ^{232}Th and ^{233}U are set to equal those of the TRUFUEL, with the amount of reactor-grade Pu defined as earlier. After accounting for these assumptions, a "missing mass" was found by matching the SIMFUEL's density to that of the TRUFUEL's density. This missing mass was then replaced by varying amounts of dysprosia and zirconia that maximized the integral indices c_k, E, and G, while constraining B^2, P_{i}, and P_{o} to within $\pm 10\%$ and k_∞ to within ± 2 mk of their reference values.

2.1 Optimization. A multiobjective genetic algorithm (MOGA) [19,20] was used to find the appropriate concentrations of dysprosia and zirconia in both the inner and outer fuel rings to maximize the integral indices, while obeying the constraints. The genetic algorithm is included in the computer code Dakota [20], which is an analysis driver code that can interface with any third-party software (in this case TSUNAMI-2D and TSUNAMI-IP). The steps followed in the execution of Dakota are as follows:

1. An initial population of data points (using various concentrations of dysprosia and zirconia) was generated and evaluated (to find the integral indices and constraints).

Table 1 TRUFUEL (reduced) isotopic composition

Isotope	Inner fuel	Outer fuel	Isotope	Inner fuel	Outer fuel	Isotope	Inner fuel	Outer fuel
O-16	4.5034×10^{-02}	4.4889×10^{-02}	Xe-131	1.6147×10^{-05}	1.5662×10^{-05}	Y-91	2.2545×10^{-06}	2.2424×10^{-06}
Th-232	1.9092×10^{-02}	1.9672×10^{-02}	Ru-106	1.5575×10^{-05}	1.5129×10^{-05}	Rb-85	2.2244×10^{-06}	2.2277×10^{-06}
Pu-239	1.2160×10^{-03}	8.9351×10^{-04}	Mo-95	1.5153×10^{-05}	1.4919×10^{-05}	Cm-244	2.1853×10^{-06}	2.2948×10^{-06}
Pu-240	7.9704×10^{-04}	6.3050×10^{-04}	Nd-145	1.4682×10^{-05}	1.4367×10^{-05}	I-127	1.9188×10^{-06}	1.8684×10^{-06}
Pu-241	4.2163×10^{-04}	3.2776×10^{-04}	Zr-92	1.4185×10^{-05}	1.4038×10^{-05}	Sm-151	1.8380×10^{-06}	1.3091×10^{-06}
Pu-242	2.5621×10^{-04}	2.1017×10^{-04}	Nd-146	1.2863×10^{-05}	1.2670×10^{-05}	Cd-111	1.7831×10^{-06}	1.7387×10^{-06}
U-233	9.2642×10^{-05}	1.0585×10^{-04}	Pd-108	1.2355×10^{-05}	1.2050×10^{-05}	Cm-242	1.6674×10^{-06}	1.5475×10^{-06}
Pu-238	8.2436×10^{-05}	6.3350×10^{-05}	Ce-144	1.1654×10^{-05}	1.1432×10^{-05}	Sr-89	1.4145×10^{-06}	1.4281×10^{-06}
Xe-136	4.7599×10^{-05}	5.0105×10^{-05}	Te-130	1.0696×10^{-05}	1.0478×10^{-05}	Sm-154	1.4132×10^{-06}	1.3800×10^{-06}
Xe-134	3.7441×10^{-05}	3.6680×10^{-05}	Pa-233	1.0409×10^{-05}	1.2260×10^{-05}	Kr-83	1.4085×10^{-06}	1.3959×10^{-06}
Mo-100	3.1811×10^{-05}	3.1097×10^{-05}	Sr-90	9.9717×10^{-06}	9.9532×10^{-06}	Pd-104	1.3933×10^{-06}	1.6254×10^{-06}
Cs-133	3.1757×10^{-05}	3.0988×10^{-05}	Zr-91	9.5344×10^{-06}	9.4636×10^{-06}	Gd-156	1.1846×10^{-06}	1.2051×10^{-06}
Cs-137	3.1740×10^{-05}	3.1128×10^{-05}	Nd-148	8.4198×10^{-06}	8.2556×10^{-06}	Sm-147	1.1642×10^{-06}	1.1288×10^{-06}
Ru-104	3.0517×10^{-05}	2.9724×10^{-05}	Pd-106	8.4140×10^{-06}	8.4317×10^{-06}	Sm-148	1.1402×10^{-06}	1.1847×10^{-06}
Ba-138	3.0472×10^{-05}	2.9877×10^{-05}	Nd-144	8.1993×10^{-06}	8.3273×10^{-06}	Ba-140	1.1056×10^{-06}	1.0773×10^{-06}
Ru-102	3.0373×10^{-05}	2.9651×10^{-05}	Ag-109	7.7725×10^{-06}	7.5324×10^{-06}	Se-82	1.0535×10^{-06}	1.0460×10^{-06}
Tc-99	2.8924×10^{-05}	2.8237×10^{-05}	Pm-147	7.0478×10^{-06}	6.7843×10^{-06}	Cs-134	1.0279×10^{-06}	1.0999×10^{-06}
Ru-101	2.8882×10^{-05}	2.8164×10^{-05}	Y-89	6.9621×10^{-06}	6.9600×10^{-06}	Cd-110	1.0186×10^{-06}	1.0748×10^{-06}
La-139	2.8330×10^{-05}	2.7799×10^{-05}	Sr-88	6.6050×10^{-06}	6.6358×10^{-06}	Pr-143	9.6166×10^{-07}	9.3917×10^{-07}
Rh-103	2.7439×10^{-05}	2.6526×10^{-05}	Sm-150	5.9497×10^{-06}	5.9434×10^{-06}	Ru-100	9.3080×10^{-07}	9.9461×10^{-07}
Mo-98	2.7095×10^{-05}	2.6541×10^{-05}	I-129	5.7531×10^{-06}	5.6229×10^{-06}	Pa-231	9.2195×10^{-07}	8.8096×10^{-07}
Ce-140	2.6513×10^{-05}	2.6064×10^{-05}	Rb-87	5.0676×10^{-06}	5.0831×10^{-06}	Sn-126	8.2140×10^{-07}	8.0132×10^{-07}
Pd-105	2.6359×10^{-05}	2.5480×10^{-05}	Nd-150	4.9773×10^{-06}	4.8634×10^{-06}	Cd-112	7.7557×10^{-07}	7.5484×10^{-07}
Xe-132	2.5939×10^{-05}	2.5561×10^{-05}	Zr-95	4.5871×10^{-06}	4.4800×10^{-06}	Cd-114	7.6697×10^{-07}	7.5661×10^{-07}
Mo-97	2.5484×10^{-05}	2.4984×10^{-05}	Sm-152	4.1334×10^{-06}	4.3669×10^{-06}	Br-81	7.4985×10^{-07}	7.4126×10^{-07}
Ce-142	2.4050×10^{-05}	2.3659×10^{-05}	Ru-103	4.0985×10^{-06}	3.9282×10^{-06}	Gd-158	7.1505×10^{-07}	7.0746×10^{-07}
Am-241	2.3361×10^{-05}	1.7818×10^{-05}	Pd-110	4.0304×10^{-06}	3.9350×10^{-06}	Kr-85	6.2502×10^{-07}	6.2836×10^{-07}
Zr-96	2.3182×10^{-05}	2.2755×10^{-05}	Kr-86	3.9188×10^{-06}	3.9215×10^{-06}	Xe-133	5.3372×10^{-07}	5.1632×10^{-07}
Cs-135	2.2773×10^{-05}	1.8937×10^{-05}	U-234	3.3821×10^{-06}	3.9535×10^{-06}	Ba-136	4.7574×10^{-07}	4.6119×10^{-07}
Pr-141	2.2478×10^{-05}	2.2082×10^{-05}	Te-128	3.1527×10^{-06}	3.1001×10^{-06}	Ba-137	4.7360×10^{-07}	4.6639×10^{-07}
Nd-143	2.0172×10^{-05}	1.9601×10^{-05}	Ce-141	2.6375×10^{-06}	2.5694×10^{-06}	I-131	4.5272×10^{-07}	4.3813×10^{-07}
Zr-94	2.0055×10^{-05}	1.9755×10^{-05}	Eu-153	2.5404×10^{-06}	2.6112×10^{-06}	Sm-149	3.9411×10^{-07}	2.8203×10^{-07}
Zr-93	1.7732×10^{-05}	1.7497×10^{-05}	Nb-95	2.4751×10^{-06}	2.4201×10^{-06}	Sb-125	3.9263×10^{-07}	3.8193×10^{-07}
Pd-107	1.7730×10^{-05}	1.7267×10^{-05}	Kr-84	2.4750×10^{-06}	2.4845×10^{-06}	Se-80	3.9031×10^{-07}	3.8746×10^{-07}
Am-243	1.7423×10^{-05}	1.6671×10^{-05}	He-4	2.2961×10^{-06}	1.9933×10^{-06}	Nd-147	3.5658×10^{-07}	3.4508×10^{-07}

Number density in nuclides $cm^{-1}\,b^{-1}$ at a burnup of 21.3 MW d kg^{-1} (IHM). Part 1 of 2. All values represent number densities. Table sorted in descending order by the inner fuel values. Inner fuel mass density: 9.91 g/cm^3 and outer fuel mass density: 9.87 g/cm^3.

2. Some points were chosen as parents, then crossover and mutation operations were performed on these parent points.

   Crossover: A set of parents was chosen to create new individuals (new data points) at some point in space between sets of parents (old data points).

   Mutation: From the cross-overed individuals, some were mutated. A random number was chosen to be added to each of the cross-overed dimensions (i.e., dysprosia and zirconia content)—still within the constraints of the phase space. These random numbers got progressively smaller as a solution was approached, so that initially the mutated individuals could be created over the whole phase space; but near the end of the analysis, they were created near the solution. This functionality was to see if other maxima existed near the solution and to allow for multiple solutions along a Pareto front. The cross-overed and mutated individuals were evaluated.
3. The best individuals were kept for the next generation.
4. Steps 2–5 were repeated until solutions were found. The stop criterion is if there was less than a 0.05% change in function evaluations, over ten generations.

The steps used in the MOGA optimization occur at stage (8) in Fig. 3.

3 Results

3.1 Verification. Table 3 shows the verification of the reduced set of isotopes and a comparison between NEWT and TSUNAMI-2D. Although TSUNAMI-2D uses NEWT to solve the 2D transport problem, the TSUNAMI-2D sequence uses BONAMIST for the unresolved resonance region and NITAWLST for the resolved resonances to process the resonant self-shielded multigroup cross section information, where NEWT uses BONAMI and NITAWL. One difference is that BONAMIST and NITAWLST generate explicit and implicit sensitivity data for the sensitivity and uncertainty analyses, whereas BONAMI and NITAWL do not. Additionally, when introducing Dancoff factors into the self-shielding calculations, TSUNAMI-2D does not accept the "dan2pitch" parameter, which is accepted into the CENTRM module in NEWT. Instead, NEWT provides an adjusted lattice pitch to account for the effect of the Dancoff factors, which is then used in TSUNAMI-2D. The adjusted lattice pitch approach, or the Dancoff approach, will both provide the same set of resonance self-shielded cross sections.

Table 3 shows small deviations from the reference case from various responses using the reduced list of isotopes in NEWT, the reduced list of isotopes in TSUNAMI-2D, and the optimized SIMFUEL responses from Dakota using TSUNAMI-2D and TSUNAMI-IP. Notice that all constraints of 2 mk and ±10% have been met in the optimization. Note that the $\Delta k_\infty = 0.18$ mk under the T-NEWT Ref. column is the difference in k_∞ with respect to T-Delp (450 days). All other differences (Δk_∞, Δ (crit. B^2), Δ (in. ring), and Δ (out. ring)) in the last three columns are with respect to the T-NEWT Ref. column.

3.2 Integral Indices. Table 4 shows the values of the integral indexes that were maximized during the optimization process performed by Dakota (the corresponding k_∞, critical B^2, P_i, and P_o are found in the last column of Table 3).

The results found in Table 4 were obtained using a number density of dysprosia of $n_i = 0.0226$ nuclides $cm^{-1}\,b^{-1}$ in the inner

Table 2 TRUFUEL (reduced) isotopic composition

Isotope	Inner fuel	Outer fuel	Isotope	Inner fuel	Outer fuel	Isotope	Inner fuel	Outer fuel
Eu-155	3.3564×10^{-07}	2.9557×10^{-07}	Te-125	5.8598×10^{-08}	5.7342×10^{-08}	Eu-151	6.0591×10^{-09}	3.8656×10^{-09}
Sn-124	3.2815×10^{-07}	3.1884×10^{-07}	Cd-113	5.4717×10^{-08}	4.2085×10^{-08}	Dy-163	5.1305×10^{-09}	5.0429×10^{-09}
Eu-154	2.7967×10^{-07}	3.0969×10^{-07}	Pm-149	4.8239×10^{-08}	4.7407×10^{-08}	Te-122	3.0919×10^{-09}	3.2252×10^{-09}
Mo-99	2.6066×10^{-07}	2.5194×10^{-07}	Xe-130	4.6951×10^{-08}	5.3369×10^{-08}	Sr-86	3.0300×10^{-09}	3.2016×10^{-09}
Te-132	2.4664×10^{-07}	2.3878×10^{-07}	Ag-111	4.3338×10^{-08}	4.1609×10^{-08}	Dy-160	3.0299×10^{-09}	3.2051×10^{-09}
Am-242m	2.4049×10^{-07}	1.8958×10^{-07}	Ag-110m	3.2963×10^{-08}	3.4705×10^{-08}	Ge-74	2.8853×10^{-09}	2.8690×10^{-09}
Cd-116	2.2324×10^{-07}	2.1599×10^{-07}	Xe-128	3.2766×10^{-08}	3.4192×10^{-08}	Y-90	2.5364×10^{-09}	2.5382×10^{-09}
U-235	2.1267×10^{-07}	2.4047×10^{-07}	Se-77	3.1108×10^{-08}	3.0871×10^{-08}	Eu-152	2.2275×10^{-09}	1.7581×10^{-09}
Sn-122	2.0164×10^{-07}	1.9576×10^{-07}	I-135	2.8117×10^{-08}	2.7173×10^{-08}	Te-124	1.8856×10^{-09}	1.9302×10^{-09}
Sn-117	1.9855×10^{-07}	1.9173×10^{-07}	Np-237	2.8054×10^{-08}	2.1756×10^{-08}	Tb-160	1.8081×10^{-09}	1.9170×10^{-09}
Se-79	1.8606×10^{-07}	1.8489×10^{-07}	Xe-135	2.6369×10^{-08}	2.1237×10^{-08}	O-17	1.8016×10^{-09}	2.4322×10^{-09}
Sb-123	1.8586×10^{-07}	1.8085×10^{-07}	Pm-148	2.5774×10^{-08}	2.7181×10^{-08}	Cd-115m	1.7623×10^{-09}	1.6843×10^{-09}
Mo-96	1.8103×10^{-07}	1.9282×10^{-07}	Dy-161	2.5598×10^{-08}	2.4230×10^{-08}	Dy-164	1.6842×10^{-09}	1.5090×10^{-09}
In-115	1.6034×10^{-07}	1.5137×10^{-07}	Sm-153	2.4986×10^{-08}	2.6754×10^{-08}	Pu-244	1.5378×10^{-09}	1.6665×10^{-09}
Sb-121	1.5872×10^{-07}	1.5339×10^{-07}	Sn-116	2.4337×10^{-08}	2.5730×10^{-08}	Ge-73	1.2207×10^{-09}	1.2138×10^{-09}
Sn-118	1.5686×10^{-07}	1.5153×10^{-07}	Cs-136	2.2688×10^{-08}	2.1649×10^{-08}	Gd-152	1.2067×10^{-09}	1.1549×10^{-09}
Sn-120	1.5344×10^{-07}	1.4854×10^{-07}	Gd-157	2.0050×10^{-08}	1.1186×10^{-08}	Ru-99	1.0157×10^{-09}	$0.0000 \times 10^{+00}$
Sn-119	1.5170×10^{-07}	1.4673×10^{-07}	Sn-123	1.6122×10^{-08}	1.5557×10^{-08}	Cm-246	$0.0000 \times 10^{+00}$	1.5959×10^{-09}
La-140	1.4631×10^{-07}	1.4272×10^{-07}	Ru-105	1.5950×10^{-08}	1.5204×10^{-08}			
Zr-90	1.4523×10^{-07}	1.4493×10^{-07}	Am-242	1.4855×10^{-08}	1.3739×10^{-08}			
Ba-134	1.4340×10^{-07}	1.5370×10^{-07}	Cm-243	1.4468×10^{-08}	1.4663×10^{-08}			
Tb-159	1.3583×10^{-07}	1.3219×10^{-07}	Pu-243	1.4432×10^{-08}	1.4227×10^{-08}			
Rh-105	1.2136×10^{-07}	1.1495×10^{-07}	Pm-151	1.4299×10^{-08}	1.3740×10^{-08}			
U-236	1.0152×10^{-07}	8.2171×10^{-08}	Te-126	1.3699×10^{-08}	1.3376×10^{-08}			
Te-129m	9.8873×10^{-08}	9.4811×10^{-08}	Ge-76	1.3662×10^{-08}	1.3680×10^{-08}			
Ce-143	9.7772×10^{-08}	9.5528×10^{-08}	Gd-155	1.0094×10^{-08}	5.4065×10^{-09}			
Te-127m	9.3177×10^{-08}	8.4783×10^{-08}	Sn-115	1.0059×10^{-08}	9.7102×10^{-09}			
Se-78	8.7566×10^{-08}	8.6968×10^{-08}	Dy-162	9.8137×10^{-09}	9.7176×10^{-09}			
Pm-148m	8.5108×10^{-08}	8.3234×10^{-08}	Gd-154	9.0258×10^{-09}	9.9823×10^{-09}			
U-232	7.9821×10^{-08}	8.8146×10^{-08}	Kr-82	8.9545×10^{-09}	9.1105×10^{-09}			
Eu-156	7.5234×10^{-08}	7.6007×10^{-08}	Th-230	7.8830×10^{-09}	7.5596×10^{-09}			
H-3	6.8547×10^{-08}	6.7177×10^{-08}	Sn-125	6.9672×10^{-09}	6.6865×10^{-09}			
Cm-245	6.5368×10^{-08}	7.3786×10^{-08}	H-1	6.6635×10^{-09}	6.2272×10^{-09}			
Gd-160	6.2449×10^{-08}	6.0667×10^{-08}	As-75	6.2759×10^{-09}	6.3428×10^{-09}			
Nd-142	6.0584×10^{-08}	7.1190×10^{-08}	Th-233	6.1567×10^{-09}	7.2789×10^{-09}			

Number density in nuclides $cm^{-1}\,b^{-1}$ at a burnup of 21.3 MW d kg^{-1} (IHM). Part 2 of 2. All values represent number densities. Table sorted in descending order by the inner fuel values. Inner fuel mass density: 9.91 g/cm^3 and outer fuel mass density: 9.87 g/cm^3

Table 3 Verification of the numerous steps in this evaluation

	Scale 6.1 sequence				
	T-Depl	T-Newt	T-Newt	TSUNAMI-2D	Dakota
Response	(450 days)	Ref. [a]	Reduced[b]	Reduced[b]	Optimized[c]
k_∞	1.14810	1.14833	1.14833	1.14832	1.14900
Δk_∞	–	(0.18 mk)	(~0.00 mk)	(−0.01 mk)	(−0.51 mk)
Crit. B^2 (10^{-3})	–	1.0301	1.0300	1.0301	1.0285
Δ (crit. B^2)	–	–	(−0.01%)	(~0.00%)	(−0.16%)
In. ring[d]	–	0.5095	0.5095	0.5095	0.5218
Δ (in. ring)	–	–	(0.00%)	(0.00%)	(2.41%)
Out. ring[d]	–	0.4905	0.4905	0.4905	0.4782
Δ (out. ring)	–	–	(0.00%)	(0.00%)	(−2.51%)

[a]Reference case of 388 isotopes.
[b]Reduced list of 192 isotopes.
[c]Optimized SIMFUEL results from Dakota's genetic algorithm.
[d]Average relative fission power per fuel ring.

ring and $n_o = 0.0583$ nuclides $cm^{-1}\,b^{-1}$ in the outer ring. The complete list of isotopes in the SIMFUEL along with their respective number densities, for the inner and outer fuel ring, can be found in Table 5.

4 Discussion

This work puts an upper limit on the similarity indices under the prescribed constraints. Thus, by solely replacing fission products and a number of actinides with dysprosia and zirconia, maximum achievable values are found, as reported in Table 4. However, other isotopes may be added in the optimization process to better match the TRUFUEL; this will likely lead to higher similarities and tighter constraints and will be investigated in future works.

In addition, the thermalhydraulic conditions presented here use supercritical water (~625 K, 22 MPa) as a coolant, which likely is not an achievable condition in available test reactors. Deviating from the Canadian PT-SCWR's nominal operating conditions will likely lead to a decrease in integral indices; due to changes in the absorption and moderation of the neutron population by the supercritical water (i.e., density changes), which affects the flux spectra and in turn would change the sensitivities, these considerations should be included in the optimization phase.

Table 4 List of maximized integral indices

Integral index	Value
c_k	0.967
E	0.992
G	0.891

Table 5 Optimized SIMFUEL isotopic composition

Isotope	Inner fuel	Outer fuel
O-16	4.8679×10^{-02}	4.8075×10^{-02}
Th-232	1.9092×10^{-02}	1.9672×10^{-02}
Zr (Natural ab.)	1.7318×10^{-03}	1.3588×10^{-03}
Pu-239	1.2160×10^{-03}	8.9351×10^{-04}
Pu-240	5.3508×10^{-04}	3.9318×10^{-04}
Pu-241	3.5346×10^{-04}	2.5972×10^{-04}
Pu-242	1.6409×10^{-04}	1.2058×10^{-04}
Dy (Natural ab.)	1.2110×10^{-04}	3.1266×10^{-04}
U-233	9.2642×10^{-05}	1.0585×10^{-04}
Pu-238	6.4628×10^{-05}	4.7488×10^{-05}

Number density in nuclides $\mathrm{cm}^{-1}\,\mathrm{b}^{-1}$ at a simulated burnup of 21.3 $\mathrm{MW\,d\,kg}^{-1}$ (IHM). All values represent number densities. Table sorted in descending order by the inner fuel values. Inner fuel mass density: 9.91 $\mathrm{g/cm}^3$ and outer fuel mass density: 9.87 $\mathrm{g/cm}^3$.

Another major factor that would influence the integral indices is the availability of actinides, such as ^{233}U, reactor-grade plutonium, and ^{241}Am (an important absorber that builds up in plutonium stockpiles from ^{241}Pu, with $\tau_{1/2} = 14$ years). Again, these considerations can be accounted for in the optimization process described earlier.

An additional constraint that could be included in the optimization could be the infinite lattice coolant void reactivity. By the same argument as above, this would likely lead to lower integral indices due to changes in the flux's energy spectrum; however, it would provide further critical experiments for data adjustment procedures.

5 Conclusion

This study has demonstrated the use of a new methodology to design SIMFUEL using the sensitivity and uncertainty analyses included in the Scale 6.1 simulation suite and the Dakota analysis suite.

High similarity (c_k and E) and coverage (G) integral indices, as shown in Table 4, have been found after absorbing fission products were replaced with dysprosia and zirconia in the inner and outer fuel rings (separately) of the Canadian PT-SCWR lattice fuel cell. The high-similarity index of $c_k = 0.967$ indicates that many of the contributors to the uncertainty in k_∞ are shared between the TRUFUEL and SIMFUEL. Additionally, the high-similarity index of $E = 0.992$ demonstrates a close match of the nuclear data sensitivity vectors between the two fuels showing the neutronic characteristics and responses will be similar. Finally, the high-coverage index of $G = 0.891$ confirms that the TRUFUEL can be included in a data adjustment and simulation bias determination.

Acknowledgment

The author (J. Sharpe) expressed his thanks to Dr. Alex Trottier of CNL for introducing him to the Dakota analysis software, which was heavily relied upon in this work. The work described in this paper was supported in part by the National Science and Engineering Research Council (NSERC) of Canada, under grant number 125519967 and by the NSERC/NRCan/AECL Generation IV Energy Technologies Program.

Nomenclature

B^2 = critical buckling
$C_{\alpha\alpha}$ = nuclear data covariance matrix
c_k = uncertainty similarity index
$D_{\text{inn.}}$ = inner fuel ring pin's Dancoff factor
$D_{\text{out.}}$ = outer fuel ring pin's Dancoff factor
E = sensitivity similarity index
G = coverage similarity index
I = number of nuclear systems
k = multiplication constant
k_∞ = infinite lattice multiplication constant
M = number of energy groups multiplied by the number of reactions multiplied by the number of nuclides ($g_{\max} \cdot x_{\max} \cdot n_{\max}$)
n_{i} = inner fuel ring pin's number density, $/\mathrm{m}^3$
n_{o} = outer fuel ring pin's number density, $/\mathrm{m}^3$
P_{i} = inner fuel ring-averaged pin fission power, J
P_{o} = outer fuel ring-averaged pin fission power, J
S_k = total sensitivity of k with respect to all nuclear data
$S_{k,\alpha}$ = sensitivity of k with respect to α
$\mathbf{S_k}$ = sensitivity vector of k with respect to nuclear data
T = temperature, K

Greek Symbols

α = nuclear data (general)
$\Delta(i)$ = difference between reference and simulated value for i
ν = neutrons per fission (prompt plus delayed)
ρ = mass density, $\mathrm{kg/m}^3$
σ^2 = nuclear data variance with respect to k
σ_i = standard deviation of nuclear data for system i
Σ_j = macroscopic cross section, $1/\mathrm{m}$
$\tau_{1/2}$ = half-life, s
χ = fission spectra

Subscripts and Superscripts

g = number of energy groups
n = number of nuclides
s = SIMFUEL
t = TRUFUEL
x = number of nuclide specific reactions

Abbreviations and Acronyms

AECL = Atomic Energy of Canada Limited
BONAMI = Bondarenko AMPX interpolator
CENTRM = continuous energy transport module
CNL = Canadian Nuclear Laboratories
IHM = inventory of heavy metal
MOGA = multiple objective genetic algorithm
NEWT = new ESC-based weighting transport code
NITAWL = Nordheim integral treatment and working library production
NRCan = Natural Resources Canada
NSERC = Natural Sciences and Engineering Research Council of Canada
PT = pressure tube
SAMS = sensitivity analysis module for scale
SCWR = supercritical water-cooled reactor
SIMFUEL = simulated irradiated fuel
TRUFUEL = truly irradiated fuel
TSUNAMI = tools for sensitivity and uncertainty analysis methodology implementation

References

[1] Radiation Safety Information Computational Center, 2013.https://rsicc.ornl.gov.
[2] Rearden, B. T., Petrie, L. M., Jessee, M. A., and Williams, M. L., 2011, "SAMS: Sensitivity Analysis Module for SCALE," Oak Ridge National Laboratory, Tech. Rep. ORNL/TM-2005/39 Version 6.1 Sect. F22.

[3] Oblow, E., 1976, "Sensitivity Theory From a Differential Viewpoint," Nucl. Sci. Eng., **59**(2), p. 187.
[4] Gandini, A., 1994, "A Generalized Perturbation Method for Bilinear Functionals of the Real and Adjoint Neutron Fluxes," J. Nucl. Energy, **21**(10), p. 7.
[5] Jessee, M., and DeHart, M., 2011, "NEWT: A New Transport Algorithm for Two-Dimensional Discrete-Ordinates Analysis in Non-Orthogonal Geometries," Oak Ridge National Laboratory, Tech. Rep. ORNL/TM-2005/39 Version 6.1 Sect. F22.
[6] Weisbin, C. R., Marable, J. H., Lucius, J. L., Oblow, E. M., Mynatt, F. R., Peelle, R. W., and Perey, F. G., 1976, "Application of FORSS Sensitivity and Uncertainty Methodology to Fast Reactor Benchmark Analysis," Union Carbide Corp., Oak Ridge National Laboratory, Tech. Rep., ORNL/TM-5563.
[7] Williams, M., Broadhead, B., and Parks, C., 2001, "Eigenvalue Sensitivity Theory for Resonance-Shielded Cross Sections," Nucl. Sci. Eng., **138**(2), pp. 177–191.
[8] Williams, M. L., 1986, "Perturbation Theory for Reactor Analysis," *CRC Handbook of Nuclear Reactors Calculations*, Vol. **3**, CRC Press, West Palm Beach, FL, pp. 63–188.
[9] Dunn, M., 2000, "PUFF-III: A Code for Processing ENDF Uncertainty Data Into Multigroup Covariance Matrices," Oak Ridge National Laboratory, ORNL/TM-1999/235 (NUREG/CR-6650).
[10] Rearden, B. T., and Jessee, M., June 2011, "TSUNAMI Utility Modules," Oak Ridge National Laboratory, Tech. Rep. ORNL/TM-2005/39 Version 6.1 Sect. M18.
[11] Broadhead, B., Rearden, B., Hopper, C., Wagschal, J., and Parks, C., 2004, "Sensitivity- and Uncertainty-Based Criticality Safety Validation Techniques," Nucl. Sci. Eng., **146**(3), pp. 340–366.
[12] Golouglu, S., Hopper, C. M., and Rearden, B. T., 2003, "Extended Interpretation of Sensitivity Data for Benchmark Areas of Applicability," Proceedings of ANS 2003 Annual Meeting, the Nuclear Technology Expansion: Unlimited Opportunities, San Diego, CA, June 1–5.
[13] Nava-Dominquez, A., Onder, E., Pencer, J., and Watts, D., 2013, "Canadian SCWR Bundle Optimization for the new Fuel Channel Design," The 6th International Symposium on Superciritcal Water-Cooled Reactors, Shenzhen, Guangdong, China, Paper No. 22.
[14] Pencer, J., Watts, D., Colton, A., Wang, X., Blomeley, L., Anghel, V., and Yue, S., 2013, "Core Neutronics for the Canadian SCWR Conceptual Design," The 6th International Symposium on Superciritcal Water-Cooled Reactors, Shenzhen, Guangdong, China, Paper No. 21.
[15] Pencer, J., McDonald, M., and Anghel, V., 2014, "Parameters for Transient Response Modeling for the Canadian SCWR," The 19th Pacific Basin Nuclear Conference, Vancouver, BC, Canada, Paper No. 403.
[16] Sharpe, J. R., Salaun, F., Hummel, D., Moghrabi, A., Nowak, M., Pencer, J., Novog, D., and Buijs, A., 2015, "A Benchmark Comparison of the Canadian Supercritical Water-Cooled Reactor (SCWR) 64-Element Fuel Lattice Cell Parameters Using Various Computer Codes," 35th Annual Conference of the Canadian Nuclear Society, Saint John, NB, Canada, Paper No. 33.
[17] Greene, N., 2011, "BONAMI, Resonance Self-Shielding by the Bondarenko Method," Oak Ridge National Laboratory, Tech. Rep. ORNL/TM-2005/39 Version 6.1 Sect. F1.
[18] Petrie, L., and Rearden, B., 2011, "MCDANCOFF Data Guide," Oak Ridge National Laboratory, Tech. Rep. ORNL/TM-2005/39 Version 6.1 Sect. M24.
[19] Chapot, J., Silva, F., and Schirru, M., 1999, "A new Approach to the use of Genetic Algorithms to Solve the Pressurized Water Reactors Fuel Management Optimization Problem," Ann. Nucl. Energy, **26**(7), pp. 641–655.
[20] The Dakota Project, 2014. "Sandia National Laboratories," http://dakota.sandia.gov.

Chapter 4

Sensitivity Analysis of ZED-2 Experiments Using (Pu,Th)O_2 Fuel Bundles to Assess Their Applicability to the SCWR Conceptual Design

Citation:

J. Sharpe, J. Atfield, J. Chow, L. Yaraskavitch, and A. Buijs, 2016, "Sensitivity Analysis of ZED-2 Experiments Using (Pu,Th)O_2 Fuel Bundles to Assess Their Applicability to the SCWR Conceptual Design," Canadian Nuclear Laboratories Nuclear Review, 5 (2), pp. 299 - 308. doi: 10.12943/CNR.2016.00039

This paper determines the applicability of legacy ZED-2 experiments, that used (Pu,Th)O_2 fuel, to the SCWR concept. Thirty-nine experiments were simulated and showed that they alone are not fit for a nuclear data adjustment and uncertainty reduction, however, can be used in conjunction with other data to perform such a task. It as also found that many key isotope sensitivities were covered because of the similar

composition of the test fuel and the SCWR concept's fuel.

FULL ARTICLE

SENSITIVITY ANALYSIS OF ZED-2 EXPERIMENTS USING (PU,TH)O_2 FUEL BUNDLES TO ASSESS THEIR APPLICABILITY TO THE SCWR CONCEPTUAL DESIGN

Jason Ray Sharpe[1]*, Julian Atfield[2], Jimmy Chow[2], Luke Yaraskavitch[2], and Adriaan Buijs[1]

[1]McMaster University, Hamilton, ON L8S 4L8, Canada
[2]Canadian Nuclear Laboratories, 286 Plant Road, Chalk River, ON K0J 1J0, Canada

Article Info
Keywords: SCWR, ZED-2, plutonia, thoria, experiment, sensitivity.
Article History: Received 11 August 2016, Accepted 17 October 2016, Available online 8 December 2016.
DOI: http://dx.doi.org/10.12943/CNR.2016.00039

*Corresponding authors: sharpejr@mcmaster.ca; jason.r.sharpe@gmail.com

The sensitivity of criticality to nuclear data has been investigated using 39 (Pu,Th)O_2 test fuel experiments that were completed in the ZED-2 reactor. Simulations were performed, for all experiments, using the multi-group Monte Carlo neutron transport code KENO V.a. The forward and adjoint fluxes were calculated to determine the sensitivity to all nuclides, reactions, and energy groups in simulations of the 39 experiments. The sensitivities of the experiments were investigated to establish if the set of experiments was suitable for a nuclear data adjustment and simulation bias determination of the Canadian supercritical water-cooled reactor. It was found that a number of important sensitivities, namely those to ^{239}Pu, ^{232}Th, and ^{2}H, were adequately covered by the experiments with G values of 0.67, 0.67, and 0.73, respectively, generated by TSUNAMI, a component of the SCALE code package. Seventeen of the 39 experiments had $0.71 > c_k > 0.6$, where the 3 largest c_k values were found to be 0.71, 0.66, and 0.66. A completeness value of $R = 0.24$ was found for the experimental set, which indicates that these experiments alone are inadequate for an accurate data adjustment and simulation bias determination.

1. Introduction

Generation II and III nuclear power reactors are aging and before long will be shut down and decommissioned, it is apparent that research in a new generation of nuclear power reactors is needed. The Generation IV International Forum (GIF) was formed in 2000 [1] to facilitate collaboration in the development of next generation reactors.

One of the GIF design options, the Canadian pressure-tube supercritical water-cooled reactor (SCWR) [1–3], is currently being developed by Canadian Nuclear Laboratories and Canadian Universities. It is designed to operate at 2540 MW_{th} with an electrical output of 1200 MW_e. The core consists of a heavy-water moderator with 336 vertical high-efficiency re-entrant flow channels [2], with the inlet and outlet plenums located above the core as shown in Figure 1.

The re-entrant flow channels have a central flow tube in which the supercritical light-water coolant enters and flows downwards. Each channel is fueled by 2 concentric rings of fuel elements with 32 elements in each ring. The proposed fuel composition is 15 wt% and 12 wt% reactor grade PuO_2 in ThO_2 in the inner and outer ring of elements, respectively. A cross-section of the SCWR fuel cell model is shown in Figure 2.

It is well known that neutron transport and diffusion codes exhibit criticality biases due to the nuclear data used in the simulations, computational approximations, physics assumptions, and model simplifications. The SCALE 6.1 [4] code package used in this work is a nuclear simulation tool suite capable of performing sensitivity and uncertainty analysis on nuclear systems in general and reactors in particular.

Throughout 1985, experiments were performed at the ZED-2 (Zero Energy Deuterium) experimental reactor operated by Atomic Energy of Canada Limited (now Canadian Nuclear Laboratories) using (Pu,Th)O_2 test fuel. This work addresses the applicability of 39 (Pu,Th)O_2 ZED-2 experiments to an SCWR bias calculation through the sensitivity of

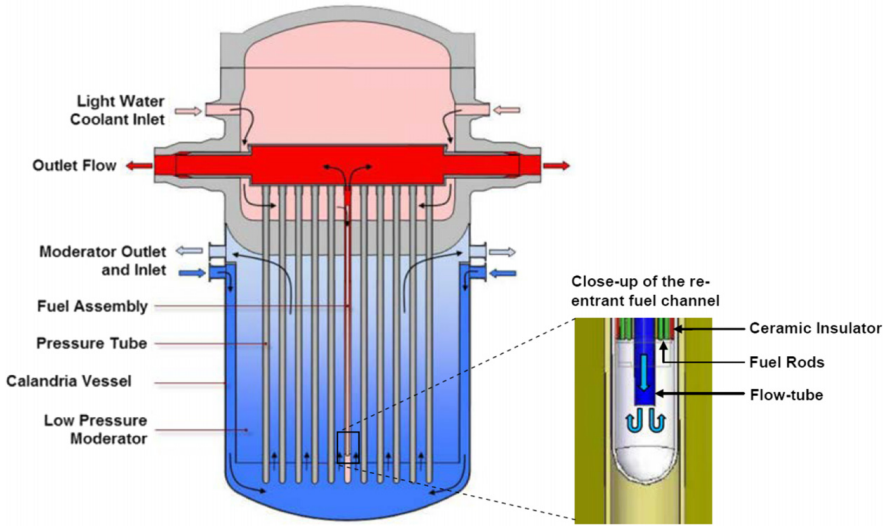

FIGURE 1. Diagram of the Canadian pressure tube SCWR concept [3].

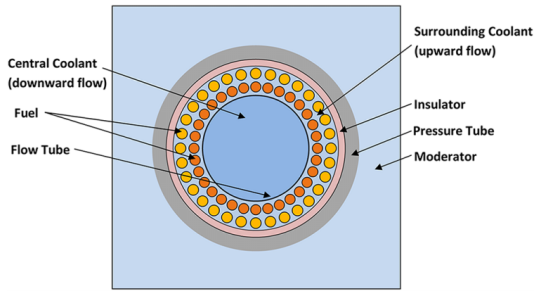

FIGURE 2. Cross-sectional view of the SCWR fuel cell.

criticality to multi-group cross-sections calculated with TSUNAMI [5] (a component of SCALE 6.1). The sensitivities are used to determine the neutronic similarity between a SCWR fuel cell and the ZED-2 experiments. The rationale behind choosing these experiments is their physical similarity to the SCWR in that they are partially fueled by (Pu,Th)O_2 and are heavy-water moderated. In addition, some experiments are light-water cooled at various pressures, albeit lower than those pressures and densities found in the SCWR.

1.1. Calculation methods

Sensitivity is defined as the change in criticality (i.e., k_{eff}) that occurs for a change in any parameter associated with the reactor. In TSUNAMI, the sensitivities ($S_{k,\Sigma}$) are defined with respect to changes in nuclear data and calculated using the adjoint-based perturbation method [6, 7] according to:

$$S_{k,\Sigma} = \frac{\Sigma}{k}\frac{\partial k}{\partial \Sigma} = -\frac{\Sigma}{k}\frac{\left\langle \phi^* \left| \frac{\partial A(\Sigma)}{\partial \Sigma} - \frac{1}{k}\frac{\partial B(\Sigma)}{\partial \Sigma} \right| \phi \right\rangle}{\left\langle \phi^* \left| \frac{B(\Sigma)}{k} \right| \phi \right\rangle} \tag{1}$$

where A is an operator representing all the terms in the transport equation except fission, B represents all the fission terms, Σ is a macroscopic cross-section, k is the multiplication constant, and ϕ and ϕ^* are the forward and adjoint fluxes, respectively. The forward and adjoint fluxes are determined by KENO V.a [8] (a module of SCALE 6.1 for criticality neutron transport calculations).

A system's sensitivities for nuclides (n), reactions (x), and energy groups (g), can be represented as a vector $\boldsymbol{S_k}$ of length M ($n \times x \times g$), which are combined with a 44-group covariance matrix [9] ($\boldsymbol{C_{\alpha\alpha}}$) to determine the system's variance [7]:

$$\sigma^2 = \boldsymbol{S_k C_{\alpha\alpha} S_k^T} \tag{2}$$

where $\boldsymbol{S_k^T}$ is the transpose of $\boldsymbol{S_k}$. Individual n, x, and g, covariances can be found by doing element-wise multiplication of Equation (2).

In this study, the integral similarity index c_k is used to quantify the similarity between 2 systems. It is a measure of the overlap of uncertainty contributions to criticality between an application, i.e., SCWR and an experiment such as ZED-2,

denoted as a and e, respectively. The c_k between systems e and a is written as [7]:

$$c_k = \frac{\sigma_{ea}^2}{\sigma_e \sigma_a} \tag{3}$$

where σ is the square root of the variance (σ^2), from Equation (2). Similarity index c_k can be extended to I systems when the sensitivity vector $\boldsymbol{S_k}$ has dimensions $I \times M$.

The integral coverage index (G) is also used to quantify the similarity between 2 systems. The definition of G is shown below [7]:

$$G = 1 - \frac{\Sigma_{n,x,g}\left(S_{n,x,g}^{a} - S_{n,x,g}^{e'}\right)}{\Sigma_{n,x,g} S_{n,x,g}^{a}} \tag{4}$$

with the constraints:

$$S_{n,x,g}^{e'} = \begin{cases} 0, \text{ if } S^{e} \text{ and } S^{a} \text{ are of opposite signs} \\ S_{n,x,g}^{e}, \text{ if } \left|S_{n,x,g}^{a}\right| \geq \left|S_{n,x,g}^{e}\right| \\ S_{n,x,g}^{a}, \text{ if } \left|S_{n,x,g}^{a}\right| < \left|S_{n,x,g}^{e}\right| \end{cases} \tag{5}$$

where $S_{n,x,g}^{a}$ and $S_{n,x,g}^{e}$ are the sensitivities of the application and experiment, respectively, for n, x, and g. However, unlike c_k, over-coverage is not taken into account with G [10, 11]. The parameter R is a measure of "the completeness of a set of experiments for the code validation of a given application" [7], and is defined as:

$$R = S^{s}/S^{a} \tag{6}$$

where

$$S^{a} = \sum_{n,x,g}\left|S_{n,x,g}^{a}\right|; \; S^{s} = \sum_{n,x,g}\left|d \times S_{n,x,g}^{s}\right|$$

and

$$d\begin{cases} 1, \text{ if } N_{n,x,g} \geq n_{\text{lim}} \\ 0, \text{ if } N_{n,x,g} < n_{\text{lim}} \end{cases}$$

where $N_{n,x,g}$ is the number of experiments with $S_{n,x,g}^{s} > \left|f \times S_{n,x,g}^{a}\right|$, in which f is the sensitivity factor ($0 \leq f \leq 1$), typically set to 0.7, as has been adopted in this study [12]. Also, s represents the composite sensitivity of the set of experiments, a represents the application, and n_{lim} was set to 1 in this work due to the small number of experiments. The completeness parameter, R, the integral coverage index, G, and the integral similarity index, c_k, can be calculated by TSUNAMI-IP, another module of SCALE 6.1.

1.2. SCWR model

In a recent SCWR study [13], the possibility of using fresh test fuel designed to match the macroscopic cross-sections of fuel irradiated in the SCWR was investigated. The SCWR irradiation was simulated using TRITON [14] (another module of SCALE 6.1), to a burnup of 21.3 MW·d·kg^{-1}. The flux and adjoint flux distributions of the SCWR fuel cell were determined by NEWT [15] (a module of SCALE 6.1). NEWT is a 2-D deterministic transport solver that employs the extended step characteristic (ESC) method to calculate fluxes, currents, and reaction rates. Details of the fuel cell model are listed in Table 1 [13, 16], including the most important fuel nuclides, and the geometry is shown in Figure 2. The complete nuclide composition of the fuel can be found in Sharpe et al. [13]. All components listed in Table 1 were included in the SCWR fuel cell model in NEWT. Note that reactivity control devices and flux detectors were omitted from the model, as those details have not yet been disseminated by the SCWR development team. The ESC method used a $s_n = 4$ symmetric quadrature set, and a scattering order of $P_n = 3$ was used for light and heavy water in the SCWR fuel cell, whereas all other materials had a scattering order of $P_n = 1$ (SCALE 6.1 default).

The resulting fission product load, determined by TRITON, was represented in the fresh test fuel by including dysprosia and zirconia. Results of the simulations showed that the fresh test fuel had a very high coverage of the SCWR irradiated fuel sensitivities. In the present study, the set of ZED-2 simulations is compared, as a whole, against the sensitivities of the TRITON-irradiated SCWR fuel from Sharpe et al. [13] to determine its coverage of the sensitivities of the SCWR fuel lattice.

It is particularly important to have a high coverage of sensitivities before a data adjustment can be performed using the GLLS (generalized linear least squares) method [17] which is used by TSURFER [18] (another module of SCALE 6.1) for nuclear data adjustment calculations. Once the data adjustment has been performed, the simulation bias can be determined.

2. Description of Experiments

All the experiments analyzed herein were conducted in ZED-2, a zero-power research reactor designed for reactor physics studies of heavy-water moderated fuel assemblies [19] such as those used in CANDU™. The reactor consists of an aluminum tank, approximately 3.36 m high by 3.36 m in diameter. The tank is open at the top to allow fuel assemblies to be suspended from above while it is void of moderator. Criticality is controlled by pumping heavy water into and out of the reactor tank.

TABLE 1. SCWR fuel cell parameters [13, 16].

Parameter	Dimension	Composition (wt%)	Density, g/cm^3	Temperature (K)
Central coolant	4.6 cm radius	H_2O	0.58756	633.79
Flow tube	4.6 cm inner radius (IR), 0.1 cm thick	C: 0.0034; Si: 0.51; Mn: 0.74; P: 0.016; S: 0.002; Ni: 20.82; Cr: 25.04; Fe: 51.738; Mo: 0.51; Zr: 0.59	7.90	657.79
Inner pins (32)	0.415 cm radius, 5.4 cm pitch circle radius	^{232}Th: 74.0925; ^{16}O: 12.0706; ^{239}Pu: 4.8567; ^{240}Pu: 3.1545; ^{241}Pu: 1.6978; ^{242}Pu: 1.0241; ^{233}U: 0.4744; ^{238}Pu: 0.3274; ^{241}Am: 0.1110; ^{136}Xe: 0.1073; ^{243}Am: 0.0875; Other: 1.9962	9.91	1420.62
Outer pins (32)	0.440 cm radius, 6.575 cm pitch circle radius	^{232}Th: 76.5671; ^{16}O: 12.0792; ^{239}Pu: 3.0037; ^{240}Pu: 2.5365; ^{241}Pu: 1.2551; ^{242}Pu: 0.8926; ^{233}U: 0.5666; ^{238}Pu: 0.2417; ^{136}Xe: 0.1584; ^{134}Xe: 0.1110; ^{137}Cs: 0.0962; Other: 2.4919	9.87	1420.62
Cladding	0.06 cm thick	As flow tube	7.90	756.3
Coolant	—	H_2O	0.14933	681.79
Liner tube	7.20 cm IR, 0.05 cm thick	As flow tube	7.90	671.80
Insulator	7.25 cm IR, 0.55 cm thick	Zr: 66.63; Y: 7.87; O: 25.5	5.83	557.17
Outer liner	7.80 cm IR, 0.05 cm thick	Sn: 3.5; Mo: 0.8; Nb: 0.8; Zr: 94.9	6.52	416.74
Pressure tube	7.85 cm IR, 1.2 cm thick	As outer liner	6.52	416.74
Moderator	25 cm square lattice pitch	D_2O: 99.833; H_2O: 0.167	1.0851	342.16

Three types of fuel assemblies were used for the experiments. The fuel of interest consisted of (Pu,Th)O_2 fuel assembled into 36-element fuel bundles. Nominal dimensions of the bundle are shown in Table 2.

The 36 elements in each bundle contained cylindrical fuel pellets with chamfered edges and a slight concavity at both ends, which are generally not explicitly modelled in reactor physics simulations. To account for this, a reduced ("smeared") density was calculated based on the radius of the pellets and the height of the pellet stack, while conserving the mass of the fuel, according to:

TABLE 2. Nominal dimensions of the 36-element (Pu,Th)O_2 test fuel.

Parameter	Nominal measurement (cm)
Fuel radius	0.6008
Fuel stack length	45.9489
Cladding inner radius	0.608
Cladding outer radius	0.654
Top plenum thickness	1.4614
Top cap thickness	0.8207
Bottom cap thickness	0.4404
Endplate thickness	0.332
Endplate radius	4.093
Bundle length	49.38
Central supp. tube inner radius	0.635
Central supp. tube outer radius	0.725

$$\rho_{\text{smear}} = \frac{m_s}{\pi R_p^2 H_s} \tag{7}$$

where m_s and H_s are the fuel stack mass and height, respectively, and R_p is the fuel pellet radius. A nominal smeared fuel density of 9.3678 g/cm^3 was obtained using Equation (7).

Table 3 shows the composition of the plutonium isotopes in weight percent. The heavy elements ($A > 89$) of the fuel consisted of 2.18 wt% Pu and 97.82 wt% ^{232}Th.

The experiments spanned a period of 215 days, approximately 8 years after the bundles were assembled and the isotopic composition was measured. Due to the decay of ^{241}Pu ($\tau_{1/2}$=14.325 years), ^{241}Am built up in the fuel. This decay over ~8 years was taken into account using the point depletion/decay code ORIGEN-ARP [20]. Differences of up to 4 mk were observed if decay in the fuel was not accounted for.

TABLE 3. Isotopic composition of (Pu,Th)O_2 test fuel, analyzed ~8 years before experiments were initiated.

Pu isotope	Wt%
^{238}Pu	0.15
^{239}Pu	76.55
^{240}Pu	19.91
^{241}Pu	2.79
^{242}Pu	0.60

The 36-element (Pu,Th)O_2 test bundles were inserted into 7 identical "hot channels", filled with D_2O or air as coolant. Each of the hot channels is equipped with a 3.5 kW heating coil at the bottom that allows the contents to be heated to approximately 300 °C. Each channel consists of a Zr + 2.5% Nb pressure tube (inner tube) with an inner and outer radius of 5.18 cm and 5.59 cm, respectively, and a Zircalloy-2 calandria tube (outer tube) with an inner and outer radius of 6.54 cm and 6.695 cm, respectively.

ZEEP rods and 28-element Natural Uranium (NU) were used as driver fuels in the experiments to bring the reactor to criticality. The 28-element (NU) UO_2 fuel bundles were loaded into aluminum channels [19] comprised of a concentric pressure tube and a calandria tube, with caps at both ends. The ZEEP rods [21] consist of uranium metal fuel slugs. Each rod contains a stack of 19 fuel slugs, each ~15 cm long and 3.25 cm in diameter, loaded into a 1 mm thick aluminum sheath with an outer diameter of ~3.5 cm.

Three different core configurations were used among the set of 39 experiments (not counting different lattice pitches). The configurations describe the positions and types of fuel assemblies, as shown in Figure 3.

A sequence of critical moderator height measurements was conducted, first for a core without test fuel (reference case)

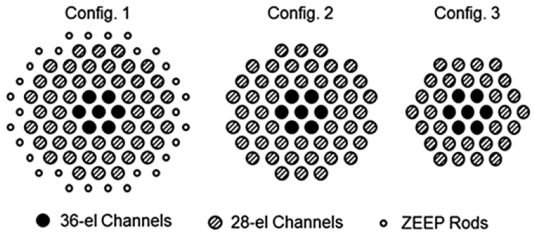

FIGURE 3. Core configurations constituted to the 39 ZED-2 experiments.

and then repeated for 1, 3, 5, and 7 hot channels containing (Pu,Th)O_2 test fuel substituted into the center of the core. With all 7 test fuel assemblies in the core, a heating experiment and detailed flux measurements were performed.

The experiments are summarized in Table 4, where the types of experiment and general core parameters can be found, and in Table 5, which contains more specific core parameters. The critical heights (H_{crit}) listed in Table 5 are the range of values, rounded to the nearest centimetre, obtained for a set of experiments. The last column indicates the time elapsed for that particular experiment since the first experiment was performed. The experiments have been labelled according to:

TABLE 4. ZED-2 core parameters of experiments performed.

Experiment label	Experiment type	# 28-el/ZEEP	Cool	Pitch (cm)	Core	Elapsed time (d)
subs-air-2	Substitution	55/0	Air	31.0	2	179
subs-d2o-2	Substitution	55/0	D_2O	31.0	2	0
subs-d2o-3	Substitution	37/0	D_2O	31.0	3	0
subs-air-1	Substitution	55/30	Air	24.5	1	215–216
subs-d2o-1	Substitution	55/30	D_2O	24.5	1	56–59
heat-d2o-2	Heat	55/0	D_2O	31.0	2	118–119
flux-d2o-2	Flux	55/0	D_2O	31.0	2	130–166
flux-air-2	Flux	55/0	Air	31.0	2	186

TABLE 5. Extended ZED-2 core parameters of experiments performed.

Experiment label	T_{cool} (°C)	T_{mod} (°C)	D_2O purity (wt%)	H_{crit} (cm)	Pitch (cm)
subs-air-2	23.22 ± 0.01	23.22 ± 0.01	99.481 ± 0.01	[178, 239]	31.0
subs-d2o-2	23.22 ± 0.01	23.22 ± 0.01	99.592 ± 0.003	[179, 228]	31.0
subs-d2o-3	23.22 ± 0.01	23.22 ± 0.01	99.591 ± 0.003	[194, 262]	31.0
subs-air-1	23.22 ± 0.01	23.22 ± 0.01	99.459 ± 0.01	[201, 252]	24.5
subs-d2o-1	23.22 ± 0.01	23.22 ± 0.01	99.579 ± 0.003	[198, 242]	24.5
heat-d2o-2	[31.3, 297.0]	23.58 ± 0.33	99.526 ± 0.009	[180, 181]	31.0
flux-d2o-2	[25.4, 300.0]	24.3 ± 1.2	99.502 ± 0.023	[179, 182]	31.0
flux-air-2	$23.1 \pm$ N/A	24.3 ± 1.2	99.502 ± 0.023	[179, 182]	31.0

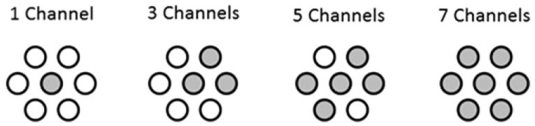

FIGURE 4. Lattice position of substituted channels near the center of the core.

(experiment type)-(coolant type)-(core configuration), for reference throughout this paper. Some specific experiments are referenced as, for example, subs(3)-air-2, which refers to an experiment that contained 3 (Pu,Th)O_2 test channels, cooled by air, and inserted into core configuration 2.

The substitution sequence experiments are labelled in this work as "subs". In each experiment, the substituted test channels were placed into specific lattice positions near the center of the core, as shown in Figure 4. After each substitution, criticality was reached and the critical moderator height was recorded.

In the heating experiment (labelled heat), 7 D_2O cooled hot channels loaded with (Pu,Th)O_2 test fuel were placed at and around the center of the core. A total of 23 critical height measurements were made as the temperature in the hot channels was raised from room temperature up to 297 °C and subsequently allowed to return to room temperature. A helium cover gas was used to suppress boiling of the coolant in the channel.

Three experiments (labelled flux) were performed to study the effect of changing the coolant type, temperature, and density, on the flux distribution around the hot channels (Figure 3). Of the 3 experiments performed: flux(c)-d2o-2 used D_2O coolant at room temperature; flux(h)-d2o-2 used D_2O coolant at 300 °C and 9.8 MPa; and flux-air-2 used air coolant at room temperature in the hot channels.

3. Methodology

A ZED-2 model generator (ZED2KENO) was used to build the KENO V.a/TSUNAMI model for each experiment based on input data describing the reactor configuration. ZED2KENO produces highly accurate models of the ZED-2 reactor, including details of the fuel bundles and channels that constitute the actual reactor core, the graphite reflector, moderator, and the region above the moderator [22].

The fuel bundles are slightly simplified in the axial direction. Firstly, the fuel pellet stacks are modelled as solid cylinders. Secondly, rather than a single plate, the endplate is modelled as small disks extending from the bottom and top of the fuel elements, while conserving the volume and mass of the endplates and nuts. The bundles also contain tie rods which were not explicitly modelled, but the density of the fuel sheath was increased to account for their mass.

The high temperature experiments (heat-d2o-2 and flux-d2o-2) required modelling the D_2O coolant at conditions far removed from SATP. Heavy-water density calculations were performed using a heavy-water table from AECL and Ontario Hydro [23].

The TSUNAMI sequence was then executed on each of the models and a list of sensitivities for each nuclide/reaction pair was produced, according to Equation (1), for each of the 39 experiments.

4. Results

In general, between all the substitution experiments, the sensitivities of criticality to ^{235}U and ^{238}U were found to decrease as the NU fuel bundles were substituted with (Pu,Th)O_2 test fuel. This is due to a reduction in the actual mass of these nuclide species in the core, particularly in the regions of highest flux, which shifts the flux towards the center of the core. In addition, the test bundles are more reactive than the driver fuel, thus the flux shift to the center of the core is amplified. Recall there is no ^{235}U or ^{238}U in the SCWR core. Conversely, the $^{239, 240, 241}Pu$, and ^{232}Th sensitivities (found in the SCWR core) increase as the NU fuel bundles are substituted with (Pu,Th)O_2 test fuel. The sensitivities of ^{239}Pu, ^{232}Th, and ^{235}U are listed in Table 6.

The flux is slightly hardened upon substitution by the test fuel since more neutrons are absorbed in the larger thermal

TABLE 6. Sensitivities for the fuel nuclides in the subs-d20-2 experiments.

Nuclides	Substance	Total	Scatter	Capture	Fission
^{239}Pu	0	0	0	0	0
	1	0.019	*	−0.012	0.031
	3	0.050	*	−0.033	0.083
	5	0.085	*	−0.053	0.138
	7	0.119	*	−0.078	0.197
^{232}Th	0	0	0	0	0
	1	−0.016	*	−0.017	*
	3	−0.044	*	−0.045	0.001
	5	−0.071	0.001	−0.073	0.002
	7	−0.103	0.001	−0.107	0.002
^{235}U	0	0.398	*	−0.082	0.480
	1	0.367	*	−0.078	0.445
	3	0.328	*	−0.069	0.397
	5	0.290	*	−0.060	0.350
	7	0.239	*	−0.051	0.290

*Sensitivity below 0.001.

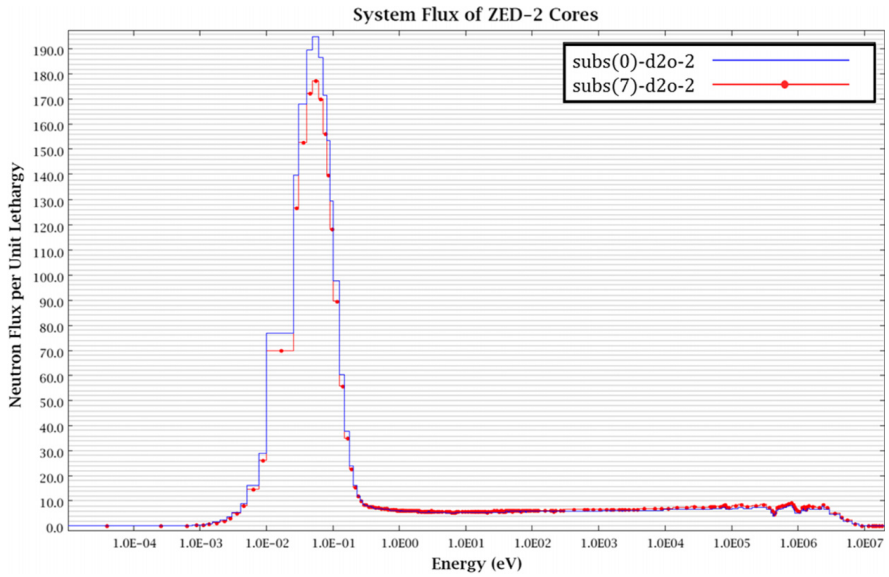

FIGURE 5. Neutron flux per unit lethargy versus energy for 2 ZED-2 experiments: subs(0)-d2o-2 and subs(7)-d2o-2.

fission cross section of ^{239}Pu than of the ^{235}U in the 28-element NU fuel. The large ^{239}Pu fission peak at 0.3 eV further reduces the thermal flux. The hardened flux can be seen in a comparison between the core-averaged flux spectra of subs-d2o-2, with and without the 7 test fuel channels substituted, as shown in Figure 5. The figure shows the thermal flux peak was reduced and redistributed at higher energies for the core substituted with 7 test fuel channels.

A notable change occurs for a few reasons in the scattering and capture sensitivity of ^{2}H and ^{1}H where both of their scattering sensitivities increase whiles their capture sensitivities decrease. Firstly, with an increase in neutron energy, both the ^{2}H and ^{1}H scattering cross-sections remain nearly constant in the thermal and epithermal range whiles the capture cross-sections decrease. As described above, the flux becomes harder as channels containing test fuel are substituted into the core, so the scattering sensitivity remains relatively constant whiles the capture sensitivity decreases. Secondly, the test bundles are more reactive due to the higher fission cross-section of the test fuel, so that the core requires less moderator to achieve criticality. Furthermore, as the critical height is decreased, the flux at the bottom of the core increases since the power of the reactor remains constant. In addition, the first ~15 cm of moderator is not displaced by any fuel so the macroscopic ^{2}H and ^{1}H cross-sections are higher. Thus, the relative increase in flux at the bottom of the core further increases the scattering sensitivity as the test channels are substituted into the core.

Some trends emerge when all results are considered, specifically the following: the effect of the flux shifting to the center of the core away from the outer region can significantly increase the sensitivity of the test fuel's nuclides, and vice versa; and the test fuel is more reactive than the driver fuel in all substitution cases.

4.1. Completeness and similarity indices

The completeness parameter (R) for all the experiments combined is 0.24, indicating that the 39 experiments alone are not adequate for coverage of the SCWR's sensitivities, and therefore, more diverse experiments are required.

The experiments with the highest coverage (integral index G) are subs(7)-d2o-3, numerous heating experiments (heat-d2o-2), and flux(c)-d2o-2; G = 0.35, 0.33, and 0.33, respectively. Similar to the low R value, this suggests that none of these experiments alone can provide enough sensitivity coverage to allow a cross-section adjustment and bias calculation.

Similar to the integral G value, the G value of a particular nuclide between 2 systems is defined as:

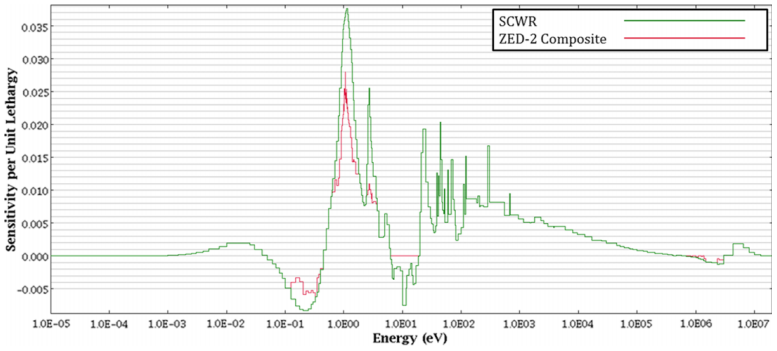

FIGURE 6. Comparison of composite ^{2}H scattering sensitivity profiles between ZED-2 experiments and SCWR.

$$G(^{z}n) = 1 - \frac{\Sigma_{x,g}\left(S^{a}_{n,x,g} - S^{e'}_{n,x,g}\right)}{\Sigma_{x,g}S^{a}_{n,x,g}} \quad (8)$$

The important nuclides of all the experiments with the largest total sensitivities include: $G(^{239}\mathrm{Pu}) = 0.67$, $G(^{232}\mathrm{Th}) = 0.67$, $G(^{2}\mathrm{H}) = 0.73$, and $G(^{91}\mathrm{Zr}) = 0.52$. This demonstrates that a significant amount of energy groups are covered for these specific nuclides.

The extent of coverage to an application by a set of experiments can be visualized in the composite sensitivity profiles for individual nuclide–reactions generated by TSUNAMI-IP. Such a profile is generated by taking the sensitivity for each group from the experiment with the highest sensitivity. Figure 6 shows the composite sensitivity profile of the experiments for ^{2}H scattering compared to that of the SCWR, demonstrating that, when all ZED-2 experiments are combined, a large portion of the ^{2}H scattering sensitivity profile for SCWR is covered. Similar coverage is seen for other important nuclide–reactions. However, a number of important nuclide–reactions, such as $^{240,\ 241}$Pu, ^{58}Ni, and ^{135}Xe, were missing.

Many experiments have individual c_k values of >0.9 for high sensitivity nuclide–reactions such as ^{239}Pu $\bar{\nu}$, ^{239}Pu fission, ^{239}Pu n, γ, and ^{2}H scatter. However, other high sensitivity nuclide–reactions such as ^{232}Th n, γ have an individual $c_k < 0.8$ for all experiments.

The majority of experiments with a high c_k had a relatively high mass of (Pu,Th)O_2 fuel in the core, i.e., subs(7) experiments, heat experiments, and flux experiments. This was also found to be the case for higher reactivity cores, i.e., with voided coolant. Seventeen of the 39 experiments were assessed to have $0.71 > c_k > 0.6$, where the 3 largest c_k values of 0.71, 0.66, and 0.66 belong to subs-d2o-3, heat(c,5)-d2o-2, and flux(c)-d2o-2, respectively.

4.2. Criticality and validation

The KENO V.a code has been extensively verified and validated for a variety of reactor geometries and fuel types. For the experiments used in the study, the k_{eff} values as determined by KENO V.a are listed in Tables 7–9. All criticality experiments in ZED-2 have an experimental $k_{\mathrm{eff}} = 1 \pm 0.07$ pcm [19], where the uncertainty is estimated from the reactor power reading. The entire set of experiments has an average bias of 0.91 ± 1.69 mk and the largest bias was found to be 3.89 mk in subs(7)-air-2, all in good agreement with the experimental k_{eff}.

However, the purpose of the study was not to provide a high-fidelity simulation of the ZED-2 reactor, it was to provide a measure of the coverage and the similarity of the ZED-2 experiments and the SCWR reactor design. This was achieved by a sensitivity and uncertainty study based on nuclear cross-section data.

5. Discussion

The validity of the test fuel model is revealed through simulations of the test lattice. A positive bias was found when (Pu,Th)O_2 test fuel was added to the core. The bias in all cases was significantly larger than the statistical uncertainty of 0.3 mk, which indicates a bias due to the nuclear data,

TABLE 7. Multiplication constant of substitution sequence experiments.

Substitution	-d20-1	-air-2	-d2o-2	-d2o-3	-air-1
0	0.9981	0.9989	0.9987	—	0.9982
1	0.9987	0.9989	0.9995	0.9993	0.9984
3	0.9989	0.9998	1.0005	0.9998	0.9987
5	0.9997	1.0015	1.0008	1.0015	0.9993
7	1.0012	1.0039	1.0030	1.0023	1.0009

TABLE 8. Multiplication constant of heating experiments.

Simulation	Coolant temperature (°C)	Coolant pressure (MPa)	Coolant density (g/cm^3)	k_{eff}
heat(c)-d20-2				
1	31.3	8.36	1.107	1.0024
2	53.9	8.60	1.098	1.0020
3	99.6	9.69	1.069	1.0030
4	152.9	9.24	1.020	1.0022
5	205.1	9.17	0.958	1.0016
6	251.6	8.89	0.887	1.0025
heat(h)-d20-2				
7	297.0	9.04	0.794	1.0026
8	288.2	7.85	0.813	1.0016
9	277.5	6.87	0.835	1.0024
10	272.8	6.47	0.844	1.0021
11	268.9	6.14	0.851	1.0017
12	99.7	6.06	1.067	1.0024

TABLE 9. Multiplication constant of flux measurement experiments.

Case	Coolant type	Coolant temperature (°C)	Coolant density (g/cm^3)	k_{eff}
flux(c)-d2o-2	D_2O	25.4	1.104	1.0026
flux(h)-d2o-2	D_2O	300.0	0.788	1.0023
flux-air-2	Air	23.1	0.001	1.0038

TABLE 10. ^{239}Pu sensitivities.

Experiment	NU assemblies	(Pu,Th)O_2 assemblies	Total	Capture	Fission
subs-d2o-3	36	1	0.039	−0.015	0.024
	34	3	0.067	−0.042	0.109
	32	5	0.100	−0.064	0.164
	30	7	0.139	−0.094	0.232
subs-d2o-2	54	1	0.019	−0.012	0.031
	52	3	0.050	−0.033	0.083
	50	5	0.085	−0.053	0.138
	48	7	0.119	−0.078	0.197

and (or) model simplifications, and (or) physics approximations. The nuclear data component was the most likely source of the discrepancy, as is usually the case when simulations and experiments are compared.

A completeness value of $R = 0.24$ indicates that the set of experiments in this study alone is inadequate for a cross-section adjustment or bias determination. However, the G values greater than 0.67 for ^{239}Pu, ^{232}Th, and ^{2}H, and the c_k values greater than 0.66 for a number of individual experiments, demonstrate that the set of ZED-2 experiments can contribute to partially covering some important sensitivities relevant to the SCWR. Obviously, more experimental data are required for accurate cross-section adjustment or bias determination.

Furthermore, leveraging the variability of the ZED-2 core geometry and composition may increase coverage of the SCWR sensitivities of the ZED-2 experiment. When NU fuel was replaced by (Pu,Th)O_2 test fuel in substitution sequence experiments, the sensitivities to all test fuel related nuclides increased, while those of the natural uranium fuel decreased, some of which are shown in Table 6. Thus, an increase in ^{239}Pu fission sensitivity (and coverage) can be achieved by an increase in Pu mass in the core. Alternatively, when fewer driver fuel channels are used in the core, while the number of test fuel channels in the core remains the same, the sensitivities of fuel nuclides are increased since they are contributing more to maintaining criticality. This is shown in Table 10.

These observations indicate that sensitivities may be enhanced by introducing materials or changing physical parameters beyond simply inserting SCWR-like assemblies into the ZED-2 reactor. For example, variations in lattice pitch, fuel pin-to-pin pitch, or channel diameters can be used to adjust sensitivities to the ^{2}H and ^{1}H scatter and absorption cross-sections. A 24% increase in ^{2}H scatter and 30% decrease in ^{2}H capture sensitivity was experienced when the lattice pitch was changed from 31 cm (subs-d2o-2) to 24.5 cm (subs-d2o-1).

Alternatively, poisons may be introduced into the moderator to adjust the neutron spectrum seen by the test fuel, thereby adjusting sensitivities associated with the fuel materials. Any reduction in the difference between a SCWR and experiment's sensitivity will increase their c_k value, their coverage G, and the set of experiments completeness (provided the SCWR's sensitivity is larger).

In general, a core completely driven by (Pu,Th)O_2 fuel would increase the sensitivity of Pu, Th, and other fuel nuclides. The Pu sensitivity alone could be increased by an increased enrichment of the Pu in the test fuel. A future study could suggest a specific set of experiments to be performed in ZED-2 that optimize the completeness parameter, coverage and c_k given the safety restrictions of the reactor, and the fuel bundles available for testing.

6. Conclusion

This paper describes a study of the sensitivities of 39 ZED-2 experiments using (Pu,Th)O_2 fuel. TSUNAMI was used to calculate the sensitivities. The applicability of the experiments

to a nuclear data adjustment and simulation bias determination for the SCWR was assessed. A completeness of $R = 0.24$ was obtained for the set of 39 experiments included in the study. Although the set of experiments alone is not adequate for a bias determination, they do provide significant coverage of many energy groups for important SCWR nuclides–reactions.

A detailed analysis of the simulation results has been performed, which revealed important physics unique to the ZED-2 core, for example, the importance of a shifting flux shape when the core is not radially uniform. The nonuniformity causes flux shifts to or from the center of the core depending on the relative reactivity of the central fuel channels with respect to the surrounding driver channels.

Acknowledgements

The author (J.S.) thanks Frédéric Salaun for his many insights and their productive discussions. He also extends his thanks to Canadian Nuclear Laboratories for their collaborative effort. The work described in this paper was supported in part by the National Science and Engineering Research Council (NSERC) of Canada, under grant number 125519967 and by the NSERC/NRCan/AECL Generation IV Energy Technologies Program.

REFERENCES

[1] K. Boyle, D. Brady, D. Guzonas, H. Khartabil, L. Leung, J. Lo, et al., 2009, "Canada's Generation-IV National Program—Overview," 4th International Symposium on Supercritical Water-Cooled Reactors, Heidelberg, Germany, 8–11 March 2009.

[2] J. Pencer, B. Bromley, and A. Nava-Dominguez, 2012, "Fuel Channel Assembly and Fuel Bundle for a Nuclear Reactor," Canadian Patent CA 2881784 A1, 13 June 2012.

[3] M. Yetisir, W. Diamond, L. Leung, D. Martin, and R. Duffey, 2011, "Conceptual Mechanical Design for a Pressure-Tube Type Supercritical Water-Cooled Reactor," Proceedings of the 5th International Symposium on Supercritical-Water-Cooled Reactors, Vancouver, BC, Canada, 13–16 March 2016.

[4] Radiation Safety Information Computational Center, 2013, "SCALE 6.1," https://rsicc.ornl.gov/.

[5] B. Rearden, 2011, "TSUNAMI-3D: Control Module for Three-Dimensional Cross-Section Sensitivity and Uncertainty Analysis for Criticality," Technical Report ORNL/TM-2005/39 Version 6.1, Section C9, Oak Ridge National Laboratory, Oak Ridge, TN, USA.

[6] B. Broadhead, B. Rearden, C. Hopper, J. Wagschal, and C.V. Parks, 2004, "Sensitivity- and Uncertainty-Based Criticality Safety Validation Techniques," Journal of Nuclear Science and Engineering, 146(3), pp. 340–366. doi: 10.13182/NSE03-2.

[7] B. Rearden and M.A. Jessee, 2011, "TSUNAMI Utility Modules," Technical Report ORNL/TM-2005/39 Version 6.1, Section M18, Oak Ridge National Laboratory, Oak Ridge, TN, USA.

[8] L. Petrie, N. Landers, D. Hollenbach, B. Readen, M. Dunn, and S. Goluoglu, 2011, "KENO V.a: An Improved Monte Carlo Criticality Program," Technical Report ORNL/TM-2005/39 Version 6.1, Section F11, Oak Ridge National Laboratory, Oak Ridge, TN, USA.

[9] M. Dunn, 2000, "PUFF-III: A Code for Processing ENDF Uncertainty Data into Multigroup Covariance Matrices," Technical Report ORNL/TM-1999/235 (NUREG/CR-6650), Oak Ridge National Laboratory, Oak Ridge, TN, USA.

[10] P. Boczar, B. Hyland, and E. Hagberh, 2010, "Qualification of Reactor Physics Toolset for a Thorium-Fuelled CANDU Reactor," Proceedings of the 18th International Conference on Nuclear Engineering, Xi'an, China, vol. 2, pp. 245–250.

[11] F. Adams and P. Boczar, 2010, "Validation of Reactor Physics Codes for Reactivity Coefficients for CANDU Reactor Applications," Proceedings of the V&V Nuclear Systems Workshop, Beach Cove Resort, North Myrtle Beach, SC.

[12] S. Langton, 2013, "Experiment Design for (Th, Pu)O_2 Power Reactors," Master's Thesis, McMaster University, Hamilton, ON, Canada.

[13] J. Sharpe, A. Buijs, and J. Pencer, 2016, "Methodology to Design Simulated Irradiated Fuel by Maximizing Integral Indices (c_k, E, G)," Journal of Nuclear Engineering and Radiation Science, 2(2), pp. 1–7. doi: 10.1115/1.4031074.

[14] M. Jessee and M. Dehart, 2011, "TRITON: A Multipurpose Transport, Depletion, and Sensitivity and Uncertainty Analysis Module," Technical Report ORNL/TM-2005/39 Version 6.1, Section T1, Oak Ridge National Laboratory, Oak Ridge, TN, USA.

[15] M. Jessee and M. DeHart, 2011, "NEWT: A New Transport Algorithm for Two-Dimensional Discrete-Ordinates Analysis in Non-Orthogonal Geometries," Technical Report ORNL/TM-2005/39 Version 6.1, Section F22, Oak Ridge National Laboratory, Oak Ridge, TN, USA.

[16] M. McDonald, A. Colton, and J. Pencer, 2015, "Power Flattening and Reactivity Suppression Strategies for the Canadian Supercritical Water Reactor Concept," Proceedings of the 35th Annual Conference of the Canadian Nuclear Society, Saint John, NB, Canada, 31 May–3 June 2015.

[17] A. Pazy, G. Rakavy, I. Reiss, J. Wagschal, A. Ya'ari, and Y. Yeivin, 1974, "The Role of Integral Data in Neutron Cross Section Evaluation," Journal of Nuclear Science and Engineering, 55, pp. 280–295. doi: 10.13182/NSE55-280.

[18] M. Williams, B. Broadhead, M. Jessee, J. Wagschal, and R. Lefebvre, 2011, "TSURFER: An Adjustment Code to Determine Biases and Uncertainties in Nuclear System Responses by Consolidating Differential Data and Benchmark Integral Experiments," Technical Report ORNL/TM-2005/39 Version 6.1, Section M21, Oak Ridge National Laboratory, Oak Ridge, TN, USA.

[19] J.E. Atfield, 2011, "28-Element Natural UO2 Fuel Assemblies in ZED-2," ZED2-HWR-EXP-001, In: *International Handbook of Evaluated Reactor Physics Benchmark Experiments*, March 2011 ed., OECD-NEA Nuclear Safety Committee, IRPhEP, OECD-NEA/NSC/DOC(2006)1, ISBN 978-92-64-99141-5, CD ROM.

[20] I. Guald, S. Bowman, and J. Horwedel, 2011, "ORIGEN-ARP: Automatic Rapid Processing for Spent Fuel Depletion, Decay, and Source Term Analysis," Technical Report ORNL/TM-2005/39 Version 6.1, Section D1, Oak Ridge National Laboratory, Oak Ridge, TN, USA.

[21] J.E. Atfield, 2012, "ZED2 Reactor: Natural-Uranium Metal Fuel Assemblies in Heavy-Water," LEU-MET-THERM-003, In: *International Handbook of Evaluated Criticality Safety Benchmark Experiment*, 2012 ed., OECD-NEA Nuclear Safety Committee, OECD Nuclear Energy Agency, NEA/NSC/DOC(95)03.

[22] J.C. Chow, 2012, "The Development of Model Generators for Specific Reactors," 24th Nuclear Simulation Symposium, Ottawa, ON, Canada, 14–16 October 2012.

[23] P. Hill, R. MacMillan, and V. Lee, 1981, "Tables of Thermodynamic Properties of Heavy Water in S.I. Units," Atomic Energy of Canada Limited, Sheridan Park, Mississauga, ON, Canada, AECL 7531.

Chapter 5

Practical Environment-corrected Discontinuity Factors and Homogenized Parameters for Improved PT-SCWR Diffusion Solutions

Submission Details:

J. Sharpe and A. Buijs, 2017, "Practical Environment-corrected Discontinuity Factors and Homogenized Parameters for Improved PT-SCWR Diffusion Solutions," Annals of Nuclear Energy. Submitted April 26, 2017. Manuscript Number: ANUCENE-D-17-00318.

This paper introduces a novel approach to improving neutron diffusion codes through the use of mean discontinuity factors. Use of the unique discontinuity factors improves cell-to-cell leakage which results in better fuel channel powers predictions. This method can be implemented, with ease, in most neutron diffusion codes that are used today as they typically have an input option for discontinuity factors. Furthermore, for the purpose

of this thesis, improved SCWR fuel channel power predictions aid in its development by offering more accurate results for other analysis such as thermalhydraulic simulations, accident scenarios, and material selection.

5.1 Erratum

Section 1: It is stated that Fick's Law is used to convert the time-independent integro-differential neutron transport equation into a second-order heterogeneous differential equation into a second-order heterogeneous differential equation. However, it should be pointed out that the Fick's Law doesn't affect the time dependence of the diffusion equation. Furthermore, the diffusion equation is a partial-differential equation and the integrals are still present after after the use of Fick's Law.

Section 1: Natural Resources Canada is financially supporting the SCWR's development, not performing the development.

Section 1.2: The discontinuity of the flux does not lead to finite difference equations, but rather that the nodal flux is solved with a set a homogenized parameters for that specific node.

Annals of Nuclear Energy 111 (2018) 101–117

Contents lists available at ScienceDirect

Annals of Nuclear Energy

journal homepage: www.elsevier.com/locate/anucene

Practical environment-corrected discontinuity factors and homogenized parameters for improved PT-SCWR neutron diffusion solutions

J.R. Sharpe *, A. Buijs

McMaster University, Hamilton, Ontario, Canada

ARTICLE INFO

Article history:
Received 26 April 2017
Received in revised form 15 August 2017
Accepted 16 August 2017

Keywords:
Discontinuity factors
Homogenization
Diffusion
Neutronics
Reflectorl SCWR

ABSTRACT

A novel application of practical discontinuity factors in coarse-mesh finite-difference solutions of heterogeneous multi cells with Pressure Tube Supercritical Water-cooled Reactor (PT-SCWR) type fuel and moderator cells has been investigated. In addition to discontinuity factors, homogenization schemes have also been studied and applied to reflector-adjacent-fuel cells and reflector cells. A 49 node inner-core multi cell model containing only fuel and a 40 node outer-core multi cell model containing reflector and fuel cells were simulated. In addition to nominal conditions, various discontinuity factors and homogenization techniques, along with conventional techniques, were applied to static beyond-nominal condition scenarios to evaluate the error associated with neutron power changes from nominal conditions, relative to reference transport solutions. The use of novel mean reference discontinuity factors and environment homogenized reflector-adjacent-fuel cells, over conventional methods, reduces core-wide reactivity errors, RMS neutron power errors, and maximum channel specific power errors by up to 2.6 mk, 2.9%, and 6.7%, respectively.

1. Introduction and background

Modern neutron transport codes are capable of accurately simulating neutronic interactions in a critical assembly. Unfortunately, the computational resources required to produce exact solutions restrict their use in routine calculations. For this reason, many approximate techniques have been developed that significantly reduce computation time at the cost of accuracy or generality. The strategy that has dominated rapid algorithms is the use of Fick's Law to convert the time-independent integro-differential neutron transport equation into a second-order heterogeneous differential equation: the neutron diffusion equation (Stacey, 2007). This strategy was met with mixed success due to assumptions made by Fick's law that do not translate well to every situation.

With Natural Resources Canada's development of a new nuclear power reactor, the Pressure Tube Supercritical Water-cooled Reactor (PT-SCWR), in collaboration with Canadian Nuclear Laboratories (CNL) and Canadian universities, the applicability of conventional nuclear simulation codes to the PT-SCWR must be determined. Approximations such as (1) assembly discontinuity factors (ADF) which are used in Pressurized Water Reactor (PWR) analysis, or (2) the non-use of discontinuity factors (equivalent to unitary discontinuity factors - UDF) in pressurized heavy-water reactors (PHWR), may not apply to the PT-SCWR. Thus, a novel approximate method has been developed and is presented in this paper.

1.1. The Canadian Pressure Tube Supercritical Water-cooled Reactor (PT-SCWR)

The PT-SCWR (Boyle et al., 2009) draws upon Canadian expertise through the use of pressure tubes similar to those used in a CANDU™ reactor. The pressure tubes proposed for the PT-SCWR are high-efficiency re-entrant flow channels (Pencer et al., 2012) and are vertically oriented to increase passive safety associated with thermal siphoning. A recent iteration of the PT-SCWR design, used in this work, was designed to operate at 2540 MWth with an electrical output of 1200 MW_e for a thermal efficiency $\eta_{th} = 48\%$.

The PT-SCWR lattice cell shown in Fig. 1 consists of an inner flow channel, two concentric rings of fuel pins with an outer flow channel bounded by insulators and a pressure tube, all of which are surrounded by a low pressure heavy-water moderator. The inner and outer rings of fuel pins are 15 wt% and 12 wt% reactor grade PuO_2 in ThO_2, respectively, with 32 fuel pins per ring. Supercritical light water coolant in the central flow tube descends to the bottom of the 5 m long channel and is subsequently redirected upwards to

* Corresponding author.
E-mail addresses: sharpejr@mcmaster.ca (J.R. Sharpe), buijsa@mcmaster.ca (A. Buijs).

http://dx.doi.org/10.1016/j.anucene.2017.08.044
0306-4549/

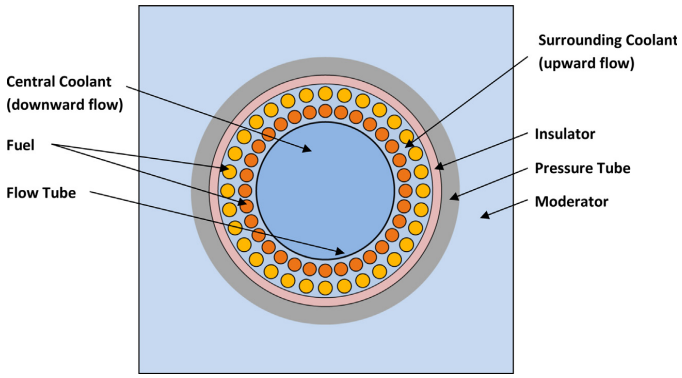

Fig. 1. Cross-sectional view of the PT-SCWR fuel cell.

pass by fuel pins to remove their generated heat. A side view of the PT-SCWR which is comprised of 336 vertical high efficiency re-entrant flow channels with an inlet and outlet plenum both located above the core is shown in Fig. 2.

1.2. Diffusion equation

Development of the PT-SCWR fuel cycle has been performed to date through the use of conventional diffusion codes developed in Canada and the USA. The conventional and modern approaches to solving the diffusion approximation are explained below.

Diffusion methods are based on a second-order heterogeneous differential neutron diffusion equation; however, further approximations can be made. One common approximation is the removal of the spatial continuity of the flux which transforms the diffusion equation into a coarse-mesh finite difference problem. Similarly, the energy dependency is discretized, in this case into two energy groups:

$$J_1 + (\Sigma_{tt1} + \Sigma_{s12} - \nu\Sigma_{f1}/k)h_x h_y \phi_1 + (-\Sigma_{s21} - \nu\Sigma_{f2}/k)h_x h_y \phi_2 = 0, \tag{1}$$

$$J_2 + (-\Sigma_{s12})h_x h_y \phi_1 + (\Sigma_{tt2} + \Sigma_{s21})h_x h_y \phi_2 = 0, \tag{2}$$

where $J = (J_x^+ + J_x^-)h_y + (J_y^+ + J_y^-)h_x$ is the group-wise leakage out of a node[1] and $k = k_{\text{eff}}$ is the effective multiplication constant. The x and y dimensions of each node are h_x and h_y, respectively. In this work, only the x and y directions are considered, however, all calculations can trivially be extended to z. Σ_{tt} is the total-transfer cross section[2] which is the absorption cross section adjusted by the (n, xn) reactions; Σ_f is the fission cross section; ν is the average number of neutrons emitted per fission; and, Σ_{s12} and Σ_{s21} are the down-scatter and up-scatter cross sections, respectively.

In order to generate the cross sections listed in Eqs. (1) and (2), a neutron transport code must be applied to a given homogenization region. The fine-energy-group cross sections are subsequently collapsed in energy, and homogenized in space, into few-group cross sections to be used in Eqs. (1) and (2).

[1] In this convention a positive J is leakage out of a cell, and negative J is leakage into a cell.

[2] Also known as the total-scatter cross section.

1.3. Spatial homogenization and energy collapse

The spatial homogenization and energy collapse problems are conceptually simple: determine homogenized and collapsed cross sections such that a region's reaction rates and interface-averaged currents are identical to those of the heterogeneous solution provided by the transport code. A 1-D representation has been used to reduce the visual complexity of equations, however, they can trivially be extended to more dimensions. If nodally-averaged heterogeneous and homogeneous reactions rates are forced to be identical, then (Smith, 1986):

$$\int_{V_i} \hat{\Sigma}_{x,g}(r)\hat{\phi}_g(r)d^3r = \int_{V_i} \Sigma_{x,g}(r)\phi_g(r)d^3r. \tag{3}$$

Likewise, if the interface-averaged currents are forced to be identical, then:

$$\oint_{S_i^k} \hat{\boldsymbol{J}}_{\boldsymbol{g}}(\boldsymbol{r}) \cdot dbiS = \oint_{S_i^k} \boldsymbol{J}_{\boldsymbol{g}}(\boldsymbol{r}) \cdot d\boldsymbol{S}, \tag{4}$$

where the hat ($\hat{}$) indicates a homogenized parameter, the bold font indicates a vector, S_i^k is the kth surface of homogenized region i, and x represents a particular reaction (not the spatial variable). Since the homogenized parameters are assumed to be constant over a homogenized region, the homogenized cross sections are:

$$\hat{\Sigma}_{x,g}(r) = \frac{\int_{V_i} \Sigma_{x,g}(r)\phi_g(r)d^3r}{\int_{V_i} \hat{\phi}_g(r)d^3r}. \tag{5}$$

If Fick's law (Stacey, 2007) ($J = -D\nabla\phi(r)$) is applied to the RHS of Eq. (4), then:

$$\hat{D}_{i,g}^k = \frac{-\oint_{S_i^k} \boldsymbol{J}_{\boldsymbol{g}}(\boldsymbol{r}) \cdot d\boldsymbol{S}}{\oint_{S_i^k} \nabla\hat{\phi}_g(r) \cdot d\boldsymbol{S}} \tag{6}$$

In the coarse-mesh finite difference (CMFD) approximation, cross sections in a homogenization region (also known as a node) are assumed to be constant, along with the few-group fluxes. The difficulty to exactly satisfy Eqs. (5) and (6) is that the solution to the heterogeneous problem must be known in advance, in addition to the solution of the homogeneous problem. Specifically, the $\hat{\phi}_g(r)$ solution relies on nodal coupling, which depends on the homogenized $\hat{D}_{i,g}^k$; however, $\hat{D}_{i,g}^k$ is also generated from the $\nabla\hat{\phi}_g(r)$ in the denominator of Eq. (6). In practice, various approximation techniques must be used to address the issue of reaction rate and interface-averaged current equivalence between homogenized

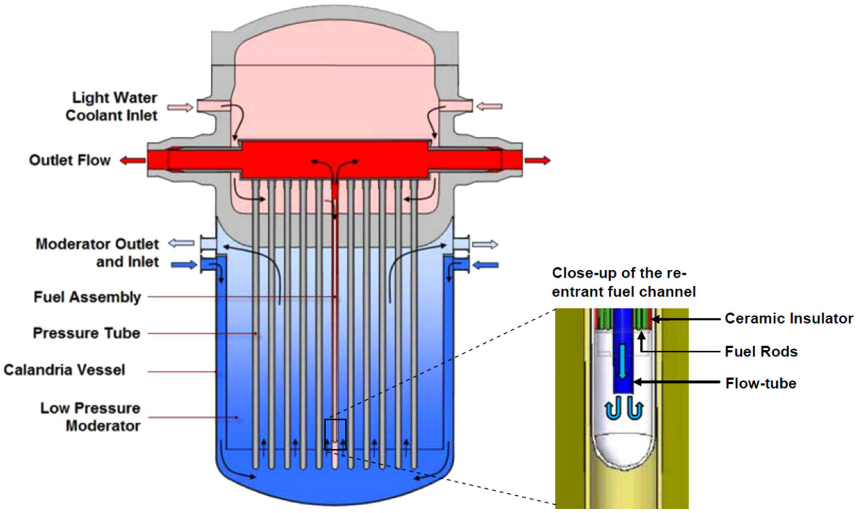

Fig. 2. Cross-sectional side view of the PT-SCWR core (Yetisir et al., 2014).

and heterogeneous parameters. A detailed discussion of why advanced homogenization techniques are needed to preserve interface-averaged currents and nodally-averaged reaction rates is given in Smith (1986). Some of the modern methods are briefly presented in this paper.

1.4. Advanced Homogenization Methods

1.4.1. Equivalence theory

One of the first advances beyond conventional homogenization was "Equivalence Theory", also known as Koebke's homogenization method (Koebke, 1978). Traditionally, homogeneous interface-averaged fluxes were continuous but Koebke proposed the homogeneous flux be discontinuous at the interface of two homogenization regions, where the discontinuities are quantified by equivalence factors. All the while, however, heterogeneous fluxes ($\bar{\psi}_i$) remained continuous at the interface (k):

$$\bar{\psi}_i^{k+} = \bar{\psi}_{i+1}^{k-}, \tag{7}$$

and,

$$f_i^{k+} = \bar{\psi}_i^{k+}/\hat{\phi}_i^{k+} \quad \text{and} \quad f_{i+1}^{k-} = \bar{\psi}_{i+1}^{k-}/\hat{\phi}_{i+1}^{k-}, \tag{8}$$

thus,

$$f_i^{k+}\hat{\phi}_i^{k+} = f_{i+1}^{k-}\hat{\phi}_{i+1}^{k-}, \tag{9}$$

where the bar ($^-$) refers to an averaged quantity.

The diffusion coefficient has no physical meaning based on its definition in Eq. (6), also any choice of diffusion coefficient can reproduce heterogeneous reactions rates and interface-averaged currents provided an additional homogenization parameter was introduced (e.g., equivalence factors). In other words, given any arbitrary diffusion coefficient the interface-averaged current and nodal reaction rates can be preserved by calculating an equivalence factor to force the current to be conserved.

In an additional step, diffusion coefficients on either side of a node (e.g., $\widehat{D}_{i,g}^{k-}$ and $\widehat{D}_{i,g}^{k+}$) can be iterated on until equivalence factors on either side of the node become equal (e.g., $f_i^{k-} = f_i^{k+}$). These specific equivalence factors which are equal on each side are called heterogeneity factors.

Equivalence Theory yields essentially zero assembly neutron power error if heterogeneity factors are generated in symmetric environments and used in symmetric environments (or vice versa), however, produces worse results if heterogeneity factors are generated in symmetric environments and used in antisymmetric environments (or vice versa). Antisymmetric problems are a reality and arise in the first cycle of PWR cores (Smith, 1986). In addition, the method requires iterations on the equivalence factors and diffusion coefficients in order to arrive at the heterogeneity factors. Furthermore, the entire geometry would need to be represented in a transport code, and simulated throughout a cycle, which is impractical.

1.4.2. General Equivalence Theory

Heterogeneity factors from equivalence theory evolved into a simpler type of *reference* discontinuity factor (RDF) which do not rely on an iterative method, nor do they suffer from symmetry problems. For this paper, the RDFs were generated for a CMFD-type problem; however, they can be generalized to any approximation of the neutron transport equation.

Diffusion coefficient(s) can be arbitrarily chosen if additional homogenization parameters are included. As such, in the derivation of RDFs, Smith decided to stay with the conventional diffusion coefficient definition (Smith, 1986):

$$D = \frac{1}{\Sigma_t - \bar{\mu}_0\Sigma_s} = \frac{1}{3\Sigma_{tr}}, \tag{10}$$

where $\bar{\mu}_0$ is the average cosine of the scattering angle. Eq. (10) was then used to determine a set of discontinuity factors that preserve the interface-averaged currents from the heterogeneous solution.

The General Equivalence Theory (GET) procedure to produce RDFs (F_i^k) which preserve the multiplication constant, interface-averaged currents and nodal-averaged reaction rates is as follows (Smith, 1980):

1. Solve the exact global heterogeneous model.
2. Acquire homogenized diffusion parameters (Eqs. (3) and (10)) for each node.

3. Solve the diffusion equation in each node to acquire homogeneous interface-averaged surface fluxes for each interface (this step isn't necessary if CMFD is used).
4. Calculate discontinuity factors for each interface k in each node i through the use of Eq. (11):

$$F_i^k = \frac{\bar{\psi}_i^k}{\hat{\phi}_i \mp \frac{\hat{J}_i^k h_i}{2D_i}}, \tag{11}$$

where the $\mp$ appears in the denominator to account for current direction. A negative is to be used if F_i^k is calculated at the upper coordinate of the node, and positive at the lower coordinate a node.
5. Solve the diffusion equation, with RDFs, for the global model.

The power of GET comes from the fact that a low-order approximation (e.g., CMFD) can be used to determine RDFs which will provide equivalence between the global heterogeneous and global solution. However, the low-order approximation used to compute the RDFs must be the same as the low-order approximation used to solve the global homogeneous solution, or else equivalence is broken. In addition, reference cross sections (RXS) from the global heterogeneous solution are required for equivalence.

GET has proven to eliminate neutron power errors and reactivity errors between the global heterogeneous and global homogeneous solution, however, the global heterogeneous solution must be known a priori.

1.4.3. Assembly discontinuity factors

It is impractical to know the global heterogeneous solution in advance, therefore RDFs aren't directly applicable to realistic situations. To address this, a single assembly homogenization with RBC is typically used to produce an approximate set of assembly cross sections (AXS) and assembly discontinuity factors (ADF):

$$f_i^k = \frac{\bar{\psi}_i^k}{\hat{\phi}_i}. \tag{12}$$

This is the accepted method today when routine calculations are performed on PWRs and BWR, which includes large 3-D reactor core simulations, optimizations, and scoping studies. This strategy works well in PWR/BWR-type problems as ADFs $\approx$ RDFs (see Table 9 in Smith (1986)), thus ADFs are an approximation to RDFs.

The use of ADFs may not be appropriate for heavy-water moderated reactors such as the PT-SCWR (or CANDU) due to the large spectral difference and leakage in fuel channels adjacent to the reflector. In addition, in an SCWR fuel lattice cell, the fuel is concentrated near the center of the lattice and surrounded on all sides by heavy-water moderator. In Section 3 this work shows that RDFs and ADFs are quite different in PT-SCWR multi cells and produce significantly different results.

1.4.4. Leakage-corrected assembly homogenization

A modern version of assembly homogenization with the use of leakage-corrected AXSs and ADFs has been developed by Rahnema and Nichita (1997). The method leverages computational advancements and extends the original method introducing albedos (i.e., leakage) on each side of an assembly to produce leakage-corrected cross sections (LXS) and leakage-corrected discontinuity factors (LDF).

In addition to the ADFs defined above in Eq. (12), the heterogeneous discontinuity factor (χ) was introduced:

$$\chi^k = \frac{\frac{1}{S^k}\int_{S^k}\psi(r)dS}{\frac{1}{V}\int_V \psi(r)dV} = \frac{\bar{\psi}^k}{\hat{\psi}}, \tag{13}$$

where χ is defined only by the heterogeneous calculation, and not by the homogeneous calculation. When Eqs. (12) and (13) are combined:

$$f^k = \frac{\bar{\psi}^k}{\hat{\phi}^k} = \frac{\bar{\psi}^k}{\hat{\psi}}\frac{\hat{\phi}}{\hat{\phi}^k} = \chi^k \frac{\hat{\phi}}{\hat{\phi}^k}, \tag{14}$$

since $\bar{\psi} = \hat{\phi}$. When discontinuity factors are defined this way, they can be calculated by individually determining the heterogeneous flux and homogeneous flux. When assembly calculations are performed, a current-to-flux branch is included for each surface. This contrasts assembly calculations which always have zero net current at the boundaries. The current-to-flux ratio (γ^k) is expressed as:

$$\gamma^k = \frac{\frac{1}{S^k}\int_{S^k} J^k(r)\cdot \mathbf{dS}}{\frac{1}{S^k}\int_{S^k}\psi(r)dS} = \frac{\bar{J}^k}{\bar{\psi}^k}. \tag{15}$$

The procedure is as follows:

1. Perform assembly calculations with γ^k branches.
2. Perform a global homogeneous calculation and determine $\bar{J}^k$ at each nodal interface.
3. Perturb homogenized cross sections and discontinuity factors based on $\bar{J}^k_{\text{Diff}}$, and hence γ^k, determined from previous step.
4. Iterate between steps 2 and 3 until convergence criteria are met in the global homogeneous solution between successive iterations.

This method has been shown to reduce maximum and root-mean-square (RMS) neutron power errors in the HAFAS BWR benchmark problem, as shown in Table 1. In addition, a string of 11 CANDU fuel cells (nine discharge burnup, two fresh) adjacent to a reflector cell, were simulated with this method. With RBC there was a substantial decrease in normalized fission rate errors of 37.2% to 1.6%. With the use of a vacuum boundary on the reflector side, the error was reduced from 40.8% to 27.6% (Usalp et al., 2015).

A similar method (Kim and Cho, 1993) was presented around the same time, which modulated the multiplication constant to adjust cell leakage, rather than a current-to-flux branch. Large improvements in the HAFAS BWR benchmark problem were realized through the use of this method.

1.4.5. Results from literature

Table 1 shows the results of the different methods described above using the HAFAS BWR benchmark (Smith, 1986; Rahnema and Nichita, 1997). The coarse meshing and number of energy groups was the same between the starred cases, thus the results are consistent; this is also true amongst the non-starred cases, however, the absolute values between the starred and non-starred cases should not be compared. Within each of the starred or non-starred cases, a decrease in RMS and maximum neutron power error has been reported when AXS-ADF was used, and a further improvement when LXS-LDF was used.

1.5. Purpose of study

A novel and practical approach to homogenization is proposed to bridge the gap between advanced methods such as those described in Section 1.4.4, which are computationally expensive but can be implemented, and those explained in Sections 1.4.2 and 1.4.1 which are essentially impossible to apply in any practical situation.

Evidently a new technique was required to accurately model the PT-SCWR while at the same time avoiding the necessity of transforming modern day simulation codes. Thus, a novel and

Table 1
HAFAS BWR results from methods described in Section 1.4.

Neutron power	AXS-UDF*	RXS-UDF*	AXS-ADF*	AXS-ADF	LXS-LDF
RMS Error	5.5%	4.1%	0.9%	1.8%	1.3%
Max Error	12.8%	11.2%	3.9%	4.8%	3.2%

AXS, RXS, LXS – Assembly, Reference, and Leakage-corrected Cross Section.
UDF, ADF, LDF – Unitary, Assembly, and Leakage-corrected Discontinuity Factors.

practical method that combines cross section and discontinuity factor preparation, and considers the fuel cell's local environment, was developed and can be implemented with existing codes.

2. Methodology

2.1. Description of multi cell reference models

Two reference models were used to explore the methods presented herein. The first model represented the inner-core region (ICRM) of the PT-SCWR reactor and consisted of only fuel cells. The second model represented the PT-SCWR's outer-core region (OCRM) and consisted of both fuel and reflector cells. Fig. 3 shows the PT-SCWR quarter core, along with the locations of its three batches of fuel (see Pencer et al., 2013 for more details).

The ICRM had reflective boundary conditions on all exterior sides, while the OCRM had a zero incoming current boundary condition on west side and reflective boundaries on all other sides. The neutron transport code NEWT (Jessee and DeHart, 2016) (part of the SCALE 6.2 Package), which employs the extended step characteristic (ESC) method, was used to simulate these large models. Unfortunately, the entire quarter PT-SCWR core could not be simulated in one execution of NEWT due to the size of the model, as NEWT was developed primarily for assembly - and not large, multi cell calculations. A 252 energy group (252 g) cross section library based on ENDF/B-VII.1 is generally used for assembly calculations; however, there was a trade-off between the maximum number of fuel lattice cells in the models and the complexity of the energy group structure. Thus, a 56 energy group (56 g) library was considered for this study, which is also based on ENDF/B-VII.1 (Williams et al., 2016).

The 56 g library was checked against the 252 g library to ensure it was suitable for this study. Specifically, both libraries were used to solve a 4×5 multi cell (K6 - G10 with reference to Fig. 3), and assembly models for each of the three different fuel types. The reactivity, RMS and maximum channel neutron power errors between the 252 g and 56 g library transport solutions are shown in the first row of Table 2. The last four rows represent the difference between diffusion solutions when 2 g cross sections are collapsed from the 252 g or 56 g solutions.

The small differences in Table 2 indicate that similar neutron power distributions are found in the diffusion solutions when 2 g diffusion parameters are homogenized from either 252 g or 56 g reference solutions (and assemblies). For this reason, heterogeneous 56 g neutron transport solutions were considered exact solutions throughout this work, which allowed for the use of larger multi cells, and hence more realistic core models.

2.2. Description of the SCWR fuel cell model

TRITON (Jessee et al., 2016) (included in the SCALE 6.2 package) was used to deplete the fuel cell shown in Fig. 1 with a specific neutron power of 47.3 $kW \cdot kg^{-1}$ (IHM) for 1500 days (103 non-uniform steps). First-cycle fuel was considered to have a burnup of 0.59 $MW \cdot d \cdot kg^{-1}$ (IHM) to allow some fission products to build

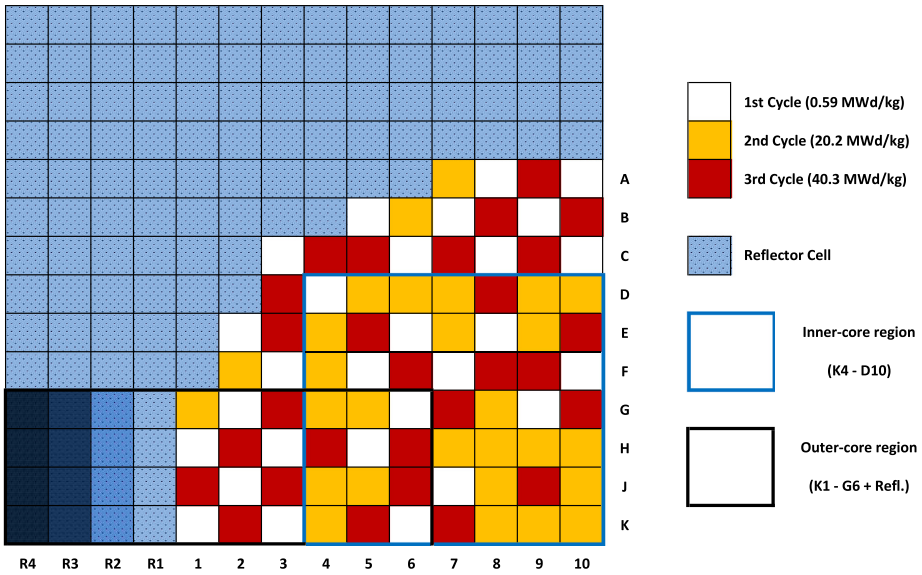

Fig. 3. Cross-sectional view of the PT-SCWR quarter core and reference model regions.

Table 2
Difference in diffusion errors which arise from homogenized 252 g and 56 g reference and assembly solutions.

Calc. Type	$\Delta\rho$ (mk)	P_{RMS} (% Err.)	P_{Max} (% Err.)
Transport	−8.34	0.04	0.08
RXS-RDF	−0.01	−0.04	−0.08
RXS-UDF	0.05	0.12	0.24
AXS-UDF	−0.04	−0.08	−0.16
AXS-ADF	−0.04	−0.07	−0.15

RXS, AXS – Reference and Assembly Cross Section.
RDF, UDF, ADF – Reference, Unitary and Assembly Discontinuity Factors.
P_{RMS} – Root-mean-squared neutron power error.
P_{Max} – Channel specific max neutron power error.

in. Second and third-cycle fuel have burnups of 20.2 and 40.3 MW·d·kg^{-1} (IHM), respectively.

To maximize the size of the multi cells, fuel isotopes with a number density below 10^{-9} nuclides · cm^{-1} b^{-1} were excluded from the ICRM and OCRM material inputs. The removal of nuclides with low number densities has been shown to not significantly impact the k_∞, critical buckling, or the inner/outer fuel ring neutron power ratio in a fuel cell (Sharpe et al., 2016).

All xenon and samarium isotopes were removed from the material inputs due to a complication that arose in the Σ_{tt} that could not be corrected without their removal. Ideally, Xe and Sm would be included in this study, but their exclusion is believed to have an insignificant impact on the conclusions of this paper. Xe and Sm concentrations would be at saturated levels, according to the neutron power level in each channel (relatively flat with control devices). In addition, Xe or Sm transients do not arise in this work as all calculations are static.

Table 3 shows the SCWR fuel cell parameters which includes materials, densities, and temperatures (further composition details can be found in Sharpe et al. (2016) and Sharpe et al. (2016)). The values in Table 3 represent a cross-section of the fuel channel at an elevation of 2.5 metres. At the nominal conditions listed in the table, only the fuel composition in each fuel cell differs, which depends on burnups, as listed in Fig. 3.

2.3. Description of diffusion code

An in–house diffusion code was developed for this study, mainly because commercial based codes, such as PARCS (Downar et al., 2012), do not have comprehensive outputs for detailed analysis (e.g., nodal current). The code can perform static calculations with vacuum or reflective boundary conditions, in addition, discontinuity factors can be used. Nodal coupling was performed with the use of Eq. (16).

$$\widehat{J}_i = -2D_iD_{i+1}\frac{f_{i+1}^{k-}\hat{\phi}_{i+1} - f_i^{k+}\hat{\phi}_i}{D_ih_{i+1}f_{i+1}^{k-} + D_{i+1}h_if_i^{k+}}, \quad (16)$$

where $\widehat{J}_i$ is the nodal current which flows from node i to $i+1$. Eq. (16) is the CMFD form of GET nodal coupling (Smith, 1986).

The in–house diffusion code was checked against the commonly used PARCS (Downar et al., 2012) diffusion code to ensure correctness of nodal coupling and the correct use of discontinuity factors and cross sections. The 2×9 reflected multi cell shown in Fig. 4 was used for verification and results were found to be essentially identical, as seen in Table 4. To ensure proper execution of the in–house code, PARCS and the in–house diffusion code were simulated with and without discontinuity factors, and with different boundary conditions. In the VBC (void boundary condition) case, only the west side of the model was void (zero incoming current), while all other sides were reflective (zero net current). Both codes were in excellent agreement, and any differences were attributed to rounding errors.

Single mesh nodes of 25×25 cm^2, matching the SCWR fuel cell square lattice pitch, were used for the diffusion calculations throughout the study. A single nodal mesh rather than a mesh study was chosen for homogenization and diffusion calculations to focus on the effect of cross sections and discontinuity factors homogenized in various environments. The vacuum boundary condition $D_{extrap.} = h_x/4 = 6.25$ cm was used in order to maintain a constant cell side length of $h_x = 25$ cm. This is mathematically equivalent to setting the extrapolation distance $h_{extrap.} = D/2$ based on the D of the vacuum boundary cell.

2.4. Description of simulated beyond-nominal condition cases

A number of beyond-nominal conditions (BNC) were evaluated to determine how well various diffusion calculation schemes predicted the neutron power changes in affected channels. The simulated BNCs were limited to coolant density reductions in the inner and outer flow tubes, individually and simultaneously. Dancoff factors were calculated for the inner and outer fuel pins (D_{inner} and D_{outer}) at each of the unique coolant density combinations through the use of the MCDancoff module (Petrie and Rearden, 2016) in SCALE 6.2. MCDancoff is a simplified Monte Carlo code capable of calculating Dancoff factors for fuel pins in complex 3-D geometries, such as PT-SCWR fuel cells.

Dancoff factors associated with the inner and outer ring of fuel pins, and coolant densities (OC = Outer Coolant, IC = Inner Coolant), are used in NEWT's "dan2pitch" card to calculate an effective pitch for a square lattice, such that a neutron's first interaction in fuel is the same in both the PT-SCWR and square lattice pin geometries. Previous work has shown (Moghrabi and Novog, 2016) the "dan2pitch" calculation to be limited by dancoff factors associated with small outer coolant densities ($\rho_{OC} < 0.4$ g·cm^{-3}) and that resonance self-shielding calculations are adversely affected. Therefore, it has been suggested that $\rho_{OC} = 0.4$ g·cm^{-3} be used for the resonance self-shielding calculations. In this work, a 0.59 MW·d·kg^{-1} fuel cell was simulated to determine the self-

Table 3
PT-SCWR fuel cell parameters (Sharpe et al., 2016; Macdonald et al., 2015).

Parameter	Dimension	Material	Density (g/cm^3)	Temp. (K)
Central coolant	4.6 cm radius	H_2O	0.58756	633.79
Flow tube	4.6 cm radius (IR), 0.1 cm thick	Zr-modified 310 Stainless Steel (Zr-mod SS)	7.90	657.79
Inner pins (32)	0.415 cm radius, 5.4 cm pitch circle radius	Variable	9.91	1593.95
Outer pins (32)	0.440 cm radius, 6.575 cm pitch circle radius	Variable	9.87	1593.95
Cladding	0.06 cm thick	Zr-mod SS	7.90	756.30
Coolant	–	H_2O	0.14933	681.79
Liner tube	7.20 IR, 0.05 cm thick	Zr-mod SS	7.90	671.80
Insulator	7.25 IR, 0.55 cm thick	Zirconia	5.83	557.17
Outer liner	7.80 IR, 0.05 cm thick	Excel (Zirconium Alloy)	6.52	416.74
Pressure tube	7.85 IR, 1.2 cm thick	Excel (Zirconium Alloy)	6.52	416.74
Moderator	25 cm square lattice pitch	D_2O: 99.833; H_2O: 0.167	1.0851	342.16

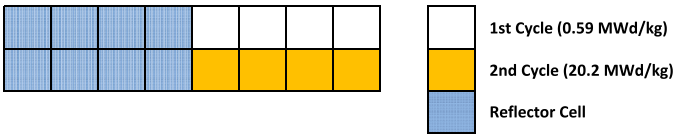

Fig. 4. Multi cell used to verify in–house diffusion code.

Table 4
Differences between PARCS and in-house diffusion code.

Discontinuity Factor	Boundary Condition	$\Delta\rho$ (pcm)	ΔP_{RMS} (%)
Unitary	Reflective	0.05	1.9×10^{-3}
Assembly	Reflective	0.05	1.8×10^{-3}
Unitary	Void	0.10	1.4×10^{-3}
Assembly	Void	0.07	1.5×10^{-3}

shielding effects between an altered $\rho_{OC} = 0.001$ g·cm^{-3} and $\rho_{OC} = 0.4$ g·cm^{-3}. A comparison between the two simulations yielded $\Delta\rho = -0.38$ mk and all cross sections to be within 0.03%, except for $\Sigma_{tt,1}$ which was within 0.14%. The differences are negligible when compared to the differences between cross sections in Table 7, thus the correction was not made.

It was shown in Sharpe et al. (2015) that the inner coolant void and outer coolant void reactivities of the PT-SCWR fuel cell change with burnup. To capture the effect of coolant density reductions on neutron power errors, various fuel channels in the ICRM and OCRM were simulated, as shown in Table 5, where the reduced coolant densities are listed in Table 6. The OCRM could not include a second-cycle fuel cell due to size limitations if all adjacent reflector cells were to be included. In addition, cells on a reflective boundary were not studied in beyond-nominal condition cases since there was no current loss on one side, which was expected to skew results in favor of assembly cross sections.

2.5. Preparation of cross sections

The ICRM is made up of only fuel cells, whereas the OCRM has fuel cells, reflector cells, and reflector-adjacent fuel cells, which can have their cross sections generated a number of ways. Although reflector cells were homogenized in this work, a single method was employed (described below), as a study of homogenization techniques is a major undertaking and was not the focus of this work. However, the use of reflector-adjacent-fuel cells (side cells) homogenized in local environments was tested.

Within the NEWT ICRM and OCRM multi cell models, each 25×25 cm^2 fuel cell had a 10×10 Cartesian mesh. Fuel cell components, such as fuel pins and the pressure tube, were comprised of single cylindrical meshes, with the exception of the outer coolant which had five concentric cylindrical meshes cutting through the fuel pins. The 25×25 cm^2 reflector cells used a 6×6 Cartesian mesh.

All simulations in this work used the 56 g ENDF/B-VII.1-based SCALE 6.2 library (as discussed in Section 2.1), with a fast-to-thermal cutoff of 0.625 eV. In addition, a flux convergence criterion of $\epsilon_\phi = 10^{-7}$ was used in all simulations, where this criterion needed to be met in each individual mesh rather than each mixture. The ESC method used an $s_n = 4$ quadrature set with a scattering order of $P_n = 3$ for light and heavy-water materials in the fuel cell and reflector to better capture directional scattering, and $P_n = 1$ for all other materials (SCALE 6.2 default).

The preparation of homogenized diffusion parameters for each type of cross section is explained below, followed by an explanation of the various diffusion calculation schemes used in this work.

Table 5
Simulated beyond-nominal condition channels.

Channel	Model	Cycle	Burnup (MW·d·kg)
F7	Inner Core Region	1	0.59
H7	Inner Core Region	2	20.2
G7	Inner Core Region	3	40.3
H1	Outer Core Region	1	0.59
J1	Outer Core Region	3	40.3

Table 6
Coolant densities and Dancoff factors of simulated nominal and beyond-nominal conditions.

Coolant Density (g·cm^{-3})		Dancoff Factors	
ρ_{OC}	ρ_{IC}	D_{inner}	D_{outer}
0.149	0.588	0.440	0.367
0.149	0.500	0.441	0.385
0.149	0.300	0.448	0.386
0.149	0.100	0.481	0.387
0.149	0.050	0.513	0.389
0.149	0.010	0.560	0.391
0.149	0.005	0.568	0.392
0.149	0.001	0.574	0.392
0.050	0.588	0.479	0.428
0.010	0.588	0.497	0.448
0.005	0.588	0.499	0.450
0.001	0.588	0.501	0.452
0.050	0.050	0.564	0.432
0.010	0.010	0.646	0.457
0.005	0.005	0.660	0.480
0.001	0.001	0.671	0.463

2.5.1. Reference cross sections

In all nominal and beyond-nominal condition cases listed in Table 6, cross sections were generated for each fuel and reflector cell. NEWT was executed at nominal and beyond-nominal conditions followed by a homogenization of diffusion parameters in each fuel and reflector cell (node). The homogenized diffusion parameters were later used in diffusion calculation schemes which involved RXSs and RDFs.

2.5.2. Assembly cross sections

Assembly cross sections were prepared using reflective boundary conditions for all sides of a single fuel cell. Since there is net zero current at the cell boundaries Eq. (11) reduces and rearranges to Eq. (12), to calculate the ADFs. An assembly calculation was performed for each unique fuel cell (i.e. varied coolant densities under BNC, and fuel composition) and finally used in diffusion calculation schemes which involved AXSs and ADFs.

2.5.3. Reflector cross sections

A practical reflector homogenization method was followed for consistency. Reflector cross sections from the OCRM showed that reflector cells in the x-direction (i.e., R1, R2, R3, and R4 from Fig. 3) had sufficiently different cross sections for them to remain unique. However, in the y-direction the relative deviations in $\Sigma_{tt,1}$ were: 1.1%, 0.2%, 1.2% and, 0.9% for R1, R2, R3 and R4, respectively,

Table 7
Reflector-adjacent-fuel cell's reference, strip, and assembly homogenized cross sections.

Cell	XS Type	RXS	SXS ($\times 10^{-2}$)	Error (%)	AXS ($\times 10^{-2}$)	Error (%)
G1	$\nu\Sigma_{f,1}$	0.293	0.293	0.15	0.294	0.50
	$\nu\Sigma_{f,2}$	2.638	2.635	−0.09	2.711	2.77
	$\Sigma_{tt,1}$	0.322	0.322	0.04	0.328	1.79
	$\Sigma_{tt,2}$	2.011	2.007	−0.20	2.120	5.39
	Σ_{s12}	0.983	0.984	0.12	1.049	6.75
H1	$\nu\Sigma_{f,1}$	0.339	0.338	−0.20	0.340	0.18
	$\nu\Sigma_{f,2}$	2.853	2.837	−0.54	2.916	2.22
	$\Sigma_{tt,1}$	0.333	0.334	0.33	0.340	2.02
	$\Sigma_{tt,2}$	2.038	2.027	−0.56	2.135	4.78
	Σ_{s12}	0.962	0.977	1.60	1.041	8.29
J1	$\nu\Sigma_{f,1}$	0.247	0.248	0.38	0.249	0.63
	$\nu\Sigma_{f,2}$	2.364	2.382	0.76	2.453	3.78
	$\Sigma_{tt,1}$	0.310	0.309	−0.31	0.314	1.44
	$\Sigma_{tt,2}$	1.945	1.959	0.75	2.070	6.43
	Σ_{s12}	1.008	0.993	−1.45	1.058	5.05

RXS, SXS, AXS – Reference, Strip, and Assembly Cross Section.

while for $\Sigma_{tt,2}$, all relative deviations were $< 0.1\%$. Thus, a flux weighted average was taken from the OCRM reflector cells, under nominal conditions, to establish the four unique reflector cell cross sections, i.e.:

$$\hat{\Sigma}_{x,g} = \frac{\sum_{y=1}^{4} \hat{\Sigma}_{x,y,g}\hat{\phi}_{x,y,g}}{\sum_{y=1}^{4} \hat{\phi}_{x,y,g}},$$
$$\text{for } x = 1,\ldots,4; g = 1,2; \text{and all diffusion parameters.} \quad (17)$$

Where x and y refer to cell location, and g the energy group. It was practical enough to perform a single multi cell calculation to acquire those reflector cross sections. However, discontinuity factors were not treated in the same fashion as cross sections in Eq. (17), due the interface currents between cells being directional, and also reflective boundaries having a net zero current.

2.5.4. Reflector-adjacent fuel cross sections (side cells)

Reflector-adjacent fuel cells, called side cells herein, have homogenized diffusion parameters which differ significantly from interior fuel cells. The presence of a nearby heavy-water reflector appreciably alters the flux spectrum in side cells compared to inner fuel cells. For this reason, to correctly predict the neutron power in side cells, cross sections need to be homogenized with the presence of the reflector, rather than the direct use of assembly cross sections, which is more suited for the inner core fuel.

One practical method of homogenizing side cells in their local environment, without adding too much complication, is to perform a small single row multi cell calculation. The single row multi cell includes a west side vacuum boundary followed by four reflector cells (as the OCRM has in a single row) and four identical fuel cells, with the remaining boundaries being reflective. These single-row multi cells are referred to as strips herein and are shown in Fig. 5. This type of practical homogenization is a novel contribution to the homogenization of side cells which also provides discontinuity factors for reflector and side cells.

Table 7 shows the homogenized RXS, side cell cross sections (SXS), and AXS for the two side cells (channels H1 and J1). It can be seen that the strip-homogenized cross sections agree much better with the RXS than the AXS, since assembly calculations do not account for local environment effects such as nodal leakage.

For practical purposes, side cells BNC cases were only simulated at three sets of conditions, namely:

- $\rho_{OC} = 0.149$ g·cm^{-3} and $\rho_{IC} = 0.001$ g·cm^{-3};
- $\rho_{OC} = 0.001$ g·cm^{-3} and $\rho_{IC} = 0.588$ g·cm^{-3};
- $\rho_{OC} = 0.001$ g·cm^{-3} and $\rho_{IC} = 0.001$ g·cm^{-3}.

For BNC densities between any of these cases a bilinear interpolation method was used to acquire new cross sections.

2.6. Preparation of discontinuity factors

Five different types of discontinuity factors were studied in this work and their preparation is described here.

Unitary Discontinuity Factors. UDFs are simply discontinuity factors which are set to $f = 1$.

Reference Discontinuity Factors. RDFs were generated based on the heterogeneous interface-averaged flux ($\bar{\psi}_i^k$), heterogeneous interface-averaged current ($\bar{J}_i^k$), and homogenized nodal flux ($\hat{\phi}_i$), by Eq. (11). Those parameters were extracted from the ICRM and OCRM solutions at under various coolant density conditions.

Assembly Discontinuity Factors. ADFs were generated by single fuel assembly simulations with reflective boundary conditions on all sides, and calculated by Eq. (12).

Strip Discontinuity Factors (R$_x$DF). The strip multi cells, defined in Fig. 5, provide the x-direction reference discontinuity factors (R$_x$DF) for the reflector cells and side cells. They were calculated through Eq. (11), as RDFs were, however, the heterogeneous interface-averaged flux ($\bar{\psi}_i^k$), heterogeneous interface-averaged current ($\bar{J}_i^k$), and homogenized nodal flux ($\hat{\phi}_i$) were taken from the strips rather than the reference model.

Mean Reference Discontinuity Factors. Mean Reference Discontinuity Factors R$_m$DFs provide a novel and practical approach to the application of discontinuity factors that are based on RDFs grouped together and averaged depending on local conditions. The steps used to calculate R$_m$DFs are shown in Fig. 6. First a lattice cell calculation is performed where the lattice is depleted and homogenized at each step (step 1 in the figure). This produces 2 group cross section files as a function of burnup, and also isotopic densities in the lattice as a function of burnup (step 3). The homogenized assembly cross sections (AXS) are used in a diffusion code to produce an equilibrium core (step 2). Meanwhile, the isotopic densities are used in conjunction with the burnup distribution from the equilibrium core to determine the fluxes ($\hat{\phi}$), side-averaged fluxes ($\bar{\psi}^k$), side averaged currents (J^k), and diffusion coefficients (D) from each node, after a transport solution is performed (step 4). This allows RDFs to be calculated (step 5) which are then grouped and averaged according to each cell's burnup, and each cell's neighbor's burnup (step 6). The grouped and averaged discontinuity factors are called mean discontinuity factors (R$_m$DF). Then, back in the diffusion code, the R$_m$DFs are entered along with AXSs, and an improved flux solution is found. This process can be

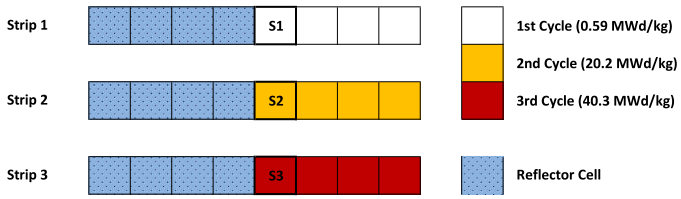

Fig. 5. Multi cells (strips) used to homogenize reflector-adjacent fuel cells (side cells).

performed multiple times for along a core's cycle to improve the solution at those points.

Fig. 7 shows the spread of RDFs as a function of the burnup difference between nodes, at the beginning-of-cycle. Other than a few outliers, most DFs fall into tight groups; DFs within a group were averaged. The same calculation was performed for end-of-cycle, and another layer of interpolation performed for models throughout a cycle. End-of-cycle R_mDFs improve max channel neutron power errors by $\sim 0.5\%$ when used instead of beginning-of-cycle R_mDFs.

Table 8 shows the R_mDFs and ADFs that were calculated as described above. More discussion on how R_mDFs can be generated and applied is provided in Section 4.

2.7. Description of equations

The conclusions drawn in this paper are based on the calculation of a number of different neutron power and reactivity errors that are defined below; an illustrative example is also provided for clarity. Consider two adjacent fuel cells with reactivity and channel powers as defined in Table 9. The values provided were hypothetically calculated by diffusion and transport codes. The equations explained below were applied to the hypothetical values and also included in Table 9.

The reactivity error between the transport (trans.) and diffusion (diff.) solutions is defined as:

$$\Delta\rho = \frac{1}{k_{\text{trans.}}} - \frac{1}{k_{\text{diff.}}}. \tag{18}$$

Whereas the neutron power error of channel i is defined as:

$$E_{P_i}(\%) = \frac{P_{i,\text{diff.}} - P_{i,\text{trans.}}}{P_{i,\text{trans.}}} \times 100, \tag{19}$$

This means the root-mean-square neutron power error can be defined as:

$$E_{P_{\text{RMS}}}(\%) = \sqrt{\frac{1}{N}\sum_i (E_{P_i})^2}, \qquad \text{where } i = 1, 2, 3, \ldots, N \tag{20}$$

and N is the total number of fuel channels in the model. The channel-specific maximum neutron power error, also known as the maximum neutron power shape error, is defined as:

$$E_{P_{\text{Max}}^{\text{Channel}}} = \max\left(\frac{P_{i,\text{diff.}} - P_{i,\text{trans.}}}{P_{i,\text{trans.}}}\right) \qquad \text{for all } i. \tag{21}$$

Eqs. (20) and (21) are the basis for this academic study, in the sense that the transport solution represents reality, and the diffusion solution represents the approximation, which is commonly used in the nuclear industry's safety analysis. If uncertainties in channel power predictions from diffusion codes can be reduced, the utility owner is left with additional margins.

Finally, the model-wide maximum neutron power error is defined as:

$$E_{P_{\text{Max}}^{\text{Model}}} = \frac{\max(P_{i,\text{diff.}}) - \max(P_{j,\text{trans.}})}{\max(P_{j,\text{trans.}})} \qquad \text{for all } i \text{ and } j. \tag{22}$$

The $E_{P_{\text{Max}}^{\text{Model}}}$ metric is another parameter that is used in nuclear power generating stations to determine the power operating margin.

A number of cells of interest were also compared to determine the difference between a nominal condition (NC) and beyond-nominal condition (BNC) solution. Simulations were performed with the transport code in both NC and BNC, and similarly, the diffusion code was simulated in BNC and NC. In order to see how well diffusion calculation schemes capture a channel neutron power change between two pseudo-static cases (i.e. NC and BNC), the transport and diffusion solutions were individually compared, to determine the channel power ratios. The BNC-to-NC channel neutron power ratio is defined as the neutron power change in a given channel under BNC relative to NC:

$$R_P^{\text{diff.}}(\rho_{\text{NC}} \rightarrow \rho_{\text{BNC}}) = \frac{P_{\text{BNC,diff.}}}{P_{\text{NC,diff.}}}, \tag{23}$$

where the same calculation is performed to determine the reference transport BNC-to-NC channel power ratio ($R_P^{\text{trans.}}$). If $R_P^{\text{diff.}} > 1$, it indicates a power increase in BNC compared to NC. Alternatively, a $R_P^{\text{diff.}} < 1$ indicates a decrease in power when going to BNC. Again, the same applies for the transport $R_P^{\text{trans.}}$.

The BNC-to-NC channel power ratio error is defined as the relative difference between the diffusion power ratio and transport power ratio from Eq. (23) for a given BNC:

$$R_P^{\text{diff.}}(\rho_{\text{NC}} \rightarrow \rho_{\text{BNC}})\text{Error}(\%) = \frac{R_P^{\text{diff.}} - R_P^{\text{trans.}}}{R_P^{\text{trans.}}}. \tag{24}$$

The BNC-to-NC channel power ratio error ($R_P^{\text{diff.}}$Error) is only a comparison of the error between the diffusion and transport power ratios when going from NC to BNC. Therefore, a negative number represents that diffusion has a smaller change than expected from transport, and a positive number indicates a larger change than expected. It does not indicate whether the diffusion and transport channel powers change in the same or opposite directions. In the few cases in this study where diffusion and transport predict opposite power changes, it is noted in the text.

3. Results

Global results are presented for nominal conditions; afterward, the predicted power ratio error between beyond-nominal conditions (BNC) and nominal conditions (NC) are presented for various diffusion calculation schemes. Both global and BNC scenario results are shown for the ICRM and OCRM.

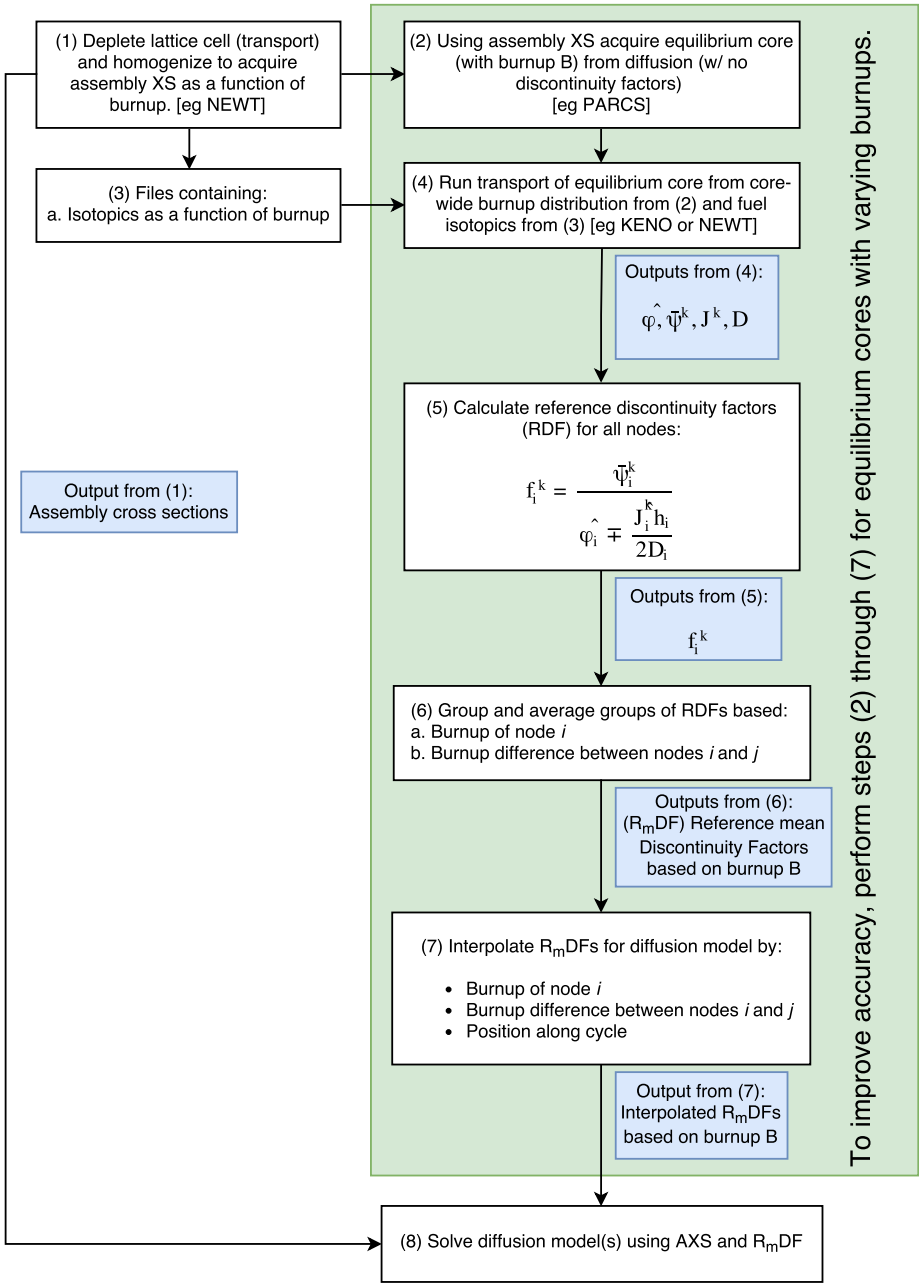

Fig. 6. Method to calculate and implement mean reference discontinuity factors.

3.1. Inner core region model results

The Table 10 shows global results under nominal conditions for the ICRM. The AXS-R_mDF scheme shows a reduction in errors compared to conventional schemes which is credited to improved neutron currents between nodes that more closely match the transport solution. The improvement is significant, but large maximum neutron power errors remain due to the spread of DFs as shown in Fig. 7.

Fig. 8 shows the BNC-to-NC channel neutron power ratio error, compared to the transport solution, when F7, G7, and H7 have their outer coolant densities reduced (individually).

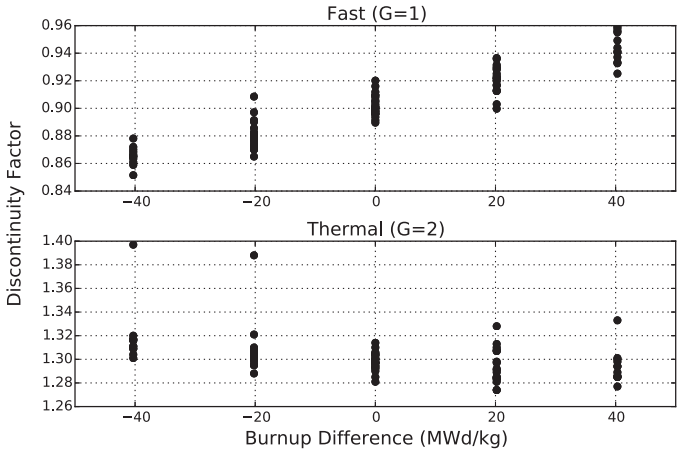

Fig. 7. Reference discontinuity factors from ICRM plotted as a function of burnup difference between adjacent nodes.

Table 8
Mean reference discontinuity factors based on the inner core region model.

B_i (MW·d·kg^{-1})	B_j (MW·d·kg^{-1})	R_mDF (G = 1)	R_mDF (G = 2)	ADF (G = 1)	ADF (G = 2)
	0.59	–	–	0.904	1.304
0.59	20.2	0.921	1.303		
	40.3	0.945	1.291		
	0.59	0.887	1.305	0.903	1.301
20.2	20.2	0.903	1.300		
	40.3	0.922	1.284		
	0.59	0.866	1.311	0.901	1.292
40.3	20.2	0.877	1.301		
	40.3	0.895	1.283		

B – Fuel cell burnup.
R_mDF, ADF – Mean reference and assembly Discontinuity Factors.

Table 9
Hypothetical Example – Results of two adjacent fuel cells.

Calc. Scheme	k_{eff}	Power Cell 1	Power Cell 2	$\Delta\rho$	E_{P_1}	E_{P_2}	$E_{P_{RMS}}$	$E_{P^{Channel}_{Max}}$	$E_{P^{Model}_{Max}}$
trans. NC	1.333	0.55	0.45	–	–	–	–	–	–
diff. NC	1.318	0.47	0.53	−8.5	−14.5	17.8	16.2	17.8	−3.6
trans. BNC	1.342	0.48	0.52	–	–	–	–	–	–
diff. BNC	1.324	0.46	0.54	−10.1	−4.2	3.8	4.0	−4.2	3.8
$R_P^{trans.}(\rho_{NC} \rightarrow \rho_{BNC})$	0.87								
$R_P^{diff.}(\rho_{NC} \rightarrow \rho_{BNC})$	0.98	→	Error (%)	12.1					

NC, BNC – Normal and Beyond Normal Conditions.
All power errors (E) are in percentage.
All reactivity errors ($\Delta\rho$) are in mk.

Fig. 9 shows results for when inner coolant densities were reduced. The G7 subplot in Fig. 9 does not show the RXS-UDF line, however, it does not exceed +0.3% power ratio error at any inner coolant density. This was done to keep the y-axis limits the same between subplots in individual figures, for ease of comparison.

Fig. 10 shows the neutron power ratio error when inner and outer coolant densities were simultaneously reduced. At nominal conditions ($\rho_{IC} = 0.58756\ \text{g·cm}^{-3}$ and $\rho_{OC} = 0.14933\ \text{g·cm}^{-3}$) the inner and outer coolant densities differ, however, they are plotted as a single point on the subplots.

Inspection of Figs. 8–10 shows that the AXS-ADF solution performed worse than AXS-UDF and AXS-R_mDF, in every situation. Additionally, all AXS cases resulted in a negative neutron power error ratio, which can be explained by a comparison of RXS and AXS at nominal and beyond-nominal conditions. At nominal conditions cross section differences between RXS and AXS were ∼0.2%-0.7% for Σ_{tt} and $\nu\Sigma_f$, and ∼1.5% for Σ_{s12}. However, at beyond-nominal conditions (i.e. $\rho_{IC} = 0.01\ \text{g·cm}^{-3}$ in channel F7) the RXS and AXS differed by 3.8%, 1.8%, and 3.2% for $\Sigma_{tt,1}$, $\nu\Sigma_{f,1}$, and Σ_{s12}, respectively. The increased assembly $\Sigma_{tt,1}$ resulted in a higher

Table 10
Inner-core-region model nominal condition's global results.

Cycle	Calc. Type	$\Delta\rho$ (mk)	Neutron Power Error (%)		
			P_{RMS}	$P_{Max}^{Channel}$	P_{Max}^{Model}
BOC	RXS-RDF	−0.22	0.03	0.07	−0.01
	RXS-UDF	0.95	4.05	11.31	11.31
	AXS-UDF	1.20	4.89	13.91	13.91
	AXS-ADF	1.12	4.80	13.77	13.77
	AXS-R_mDF	0.34	3.93	10.98	10.98
EOC	RXS-RDF	−0.23	0.04	0.10	0.05
	RXS-UDF	1.52	4.92	13.44	13.44
	AXS-UDF	1.87	6.01	16.74	16.74
	AXS-ADF	1.72	5.88	16.51	16.51
	AXS-R_mDF	1.59	5.39	11.29	11.29

RXS, AXS – Reference and assembly cross sections.
RDF, UDF - Reference and unitary discontinuity factors.
R_mDF, ADF – Mean reference and assembly discontinuity factors.
BOC, EOC – Beginning and End-of-Cycle.

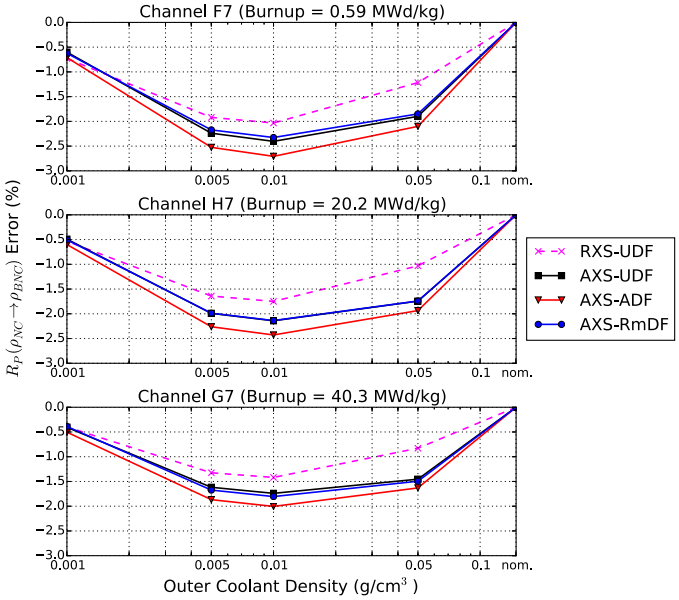

Fig. 8. Neutron power ratio error in ICRM beyond-nominal condition channels when outer coolant densities were reduced.

absorption rate and lower flux when compared to RXS, which in turn led to a smaller neutron power ratio for AXS than RXS predicted by transport. In each AXS beyond-nominal case a lower flux was found than predicted by RXS, whereas in the nominal case AXS and RXS were similar, which resulted in negative neutron power ratio errors for AXS cases. Finally, Figs. 8–10 show that errors are largest with first-cycle fuel, and lessen as the fuel ages.

3.2. Outer core region model results

Global OCRM results under nominal conditions are shown in Table 11. Consider that different types of discontinuity factors can be used in different directions. R_xDFs were acquired from the strip calculations as described in Section 2.5.4, however, there is no way to acquire the y-direction reflector cell DFs in a practical way, thus UDFs were used. In addition, R_mDFs were used for side cells in the y-direction.

In Table 11, the first two rows represent standard homogenization and diffusion calculation techniques, where row 3, 4, and 5 are for comparison between SXS and AXS use. The sixth row is the novel and practical method proposed in this work, which is a combination of mean reference discontinuity factors extracted from ICRM, and the strip discontinuity factors for the reflector and side cell. A significant reduction in RMS and channel specific max neutron power errors was achieved, along with a reduction in reactivity error.

Fig. 11 shows the neutron power error ratio, compared to the transport solution, when H1 and J1 had their outer coolant densities reduced. Similarly, Fig. 12 shows H1 and J1 with reduced inner coolant densities and Fig. 13 with both inner and outer coolant densities reduced.

The collection of results shows the use of AXS, SXS, and R_mDFs in a single calculation scheme generally improves upon reactivity and neutron power errors, in both the inner and outer core regions,

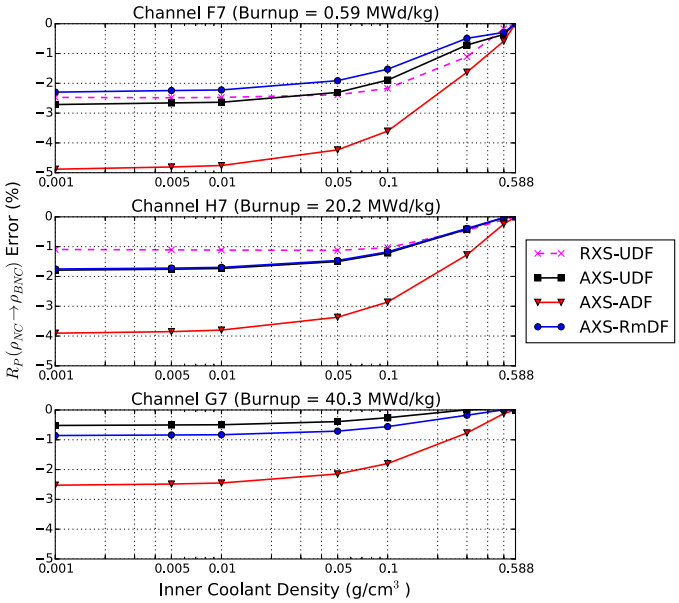

Fig. 9. Neutron power ratio error in ICRM beyond-nominal condition channels when inner coolant densities were reduced.

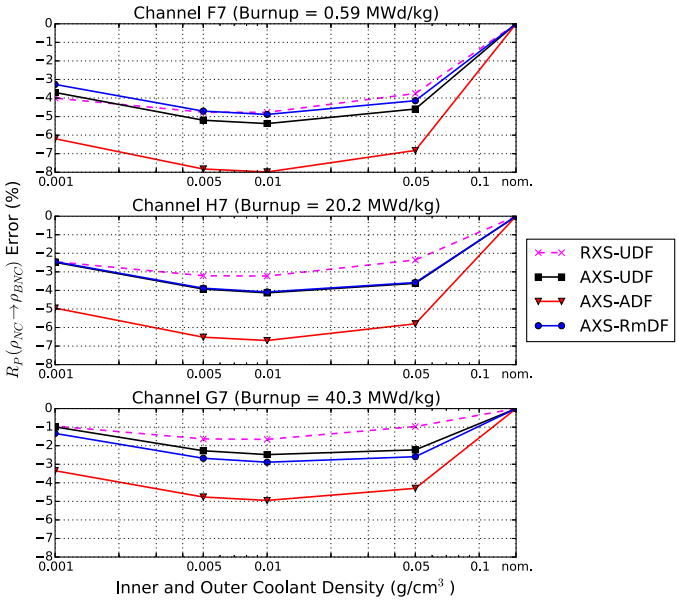

Fig. 10. Neutron power ratio error in ICRM beyond-nominal condition channels when outer and inner coolant densities were reduced.

under nominal conditions. In addition, in the inner core beyond-nominal condition cases, AXS-R$_m$DF dramatically improves upon AXS-ADF calculations, and offers similar performance to AXS-UDF calculations, however, in the outer core region improvements were substantial over AXS-UDF calculations as shown in Table 11.

Table 11
Outer-core-region model nominal condition's global results.

Discontinuity Factor			Cross section	$\Delta\rho$	Neutron Power Error (%)		
Refl.	Side	Inner	Side/Inner	(mk)	P_{RMS}	$P_{Max}^{Channel}$	P_{Max}^{Model}
U	U	U	A/A	1.01	4.77	10.71	10.71
U	U	A	A/A	0.96	4.76	10.57	10.57
U_yR_x	$R_{m,y}R_x$	R_m	A/A	-1.33	6.77	13.92	11.74
U	U	U	Side/A	3.29	4.63	8.63	2.34
U	U	A	Side/A	3.25	4.38	7.89	2.22
U_yR_x	$R_{m,y}R_x$	R_m	Side/A	0.67	1.87	4.06	4.06

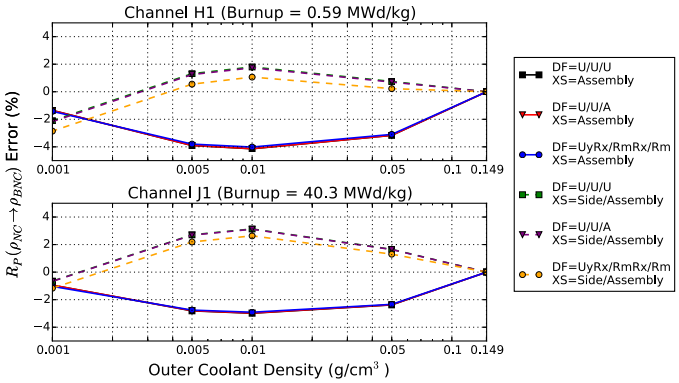

Fig. 11. Neutron power ratio error in beyond-nominal condition channels during a loss of outer coolant event in the OCRM.

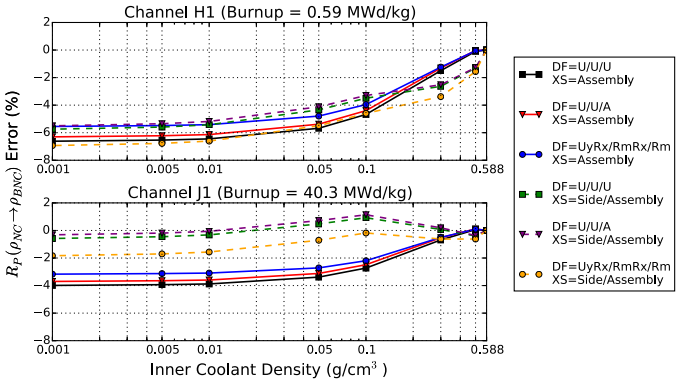

Fig. 12. Neutron power ratio error in beyond-nominal condition channels during a loss of inner coolant event in the OCRM.

4. Discussion

4.1. Small power increases

Figs. 8–10 show that neutron power ratio errors were always negative. When these values are used in safety analysis, such as a coupled neutronics and thermalhydraulics simulation, at each iteration, beyond-nominal condition channel results are under-predicted. This causes a number of potential problems in a reactor's design and development phase:

1. If beyond-nominal condition channel neutron powers truly decrease (i.e. transport prediction), diffusion predicts a smaller neutron power, which results in a more rapid neutron power reduction.
2. If beyond-nominal condition channel neutron powers truly increase, diffusion predicts a smaller neutron power increase, which results in a slower transient.
3. If beyond-nominal condition channel neutron powers truly increase, but only by a small amount (e.g. $R = \sim 1.00 - 1.03$), diffusion theory predicts an $R < 1$, which indicates a neutron power decrease, rather than an increase.

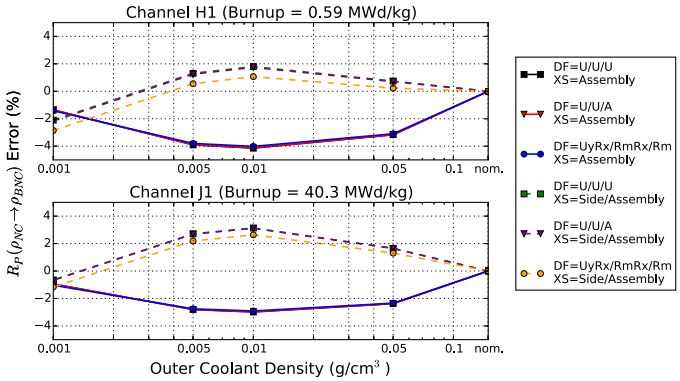

Fig. 13. Neutron power ratio error in beyond-nominal channels during a loss of inner and outer coolant event in the OCRM.

The latter is indeed the case with a void of outer coolant in the side cell, where the transport neutron power ratio in the beyond-nominal condition channels increases, however, all diffusion models without the use of SXS predict a neutron power decrease. This presents problems in transients that start with a slow neutron power increase due to a slow outer coolant density reduction, as when the neutron power is truly increasing the whole time, further reducing the coolant density, the safety analysis would show a neutron power decrease which results in a coolant density increase, further reducing the neutron power. Fortunately, inclusion of SXS fixes the issue, and allows for a more accurate diffusion prediction of small positive reactivity transients.

4.2. Side cell beyond-nominal conditions

A number of beyond-nominal conditions were simulated in strip models, and compared to the reference cases, and only small cross section differences ($< 4\%$) were found. This method is flexible however, as any number of beyond-nominal condition strip calculations can be added to the interpolation table to improve results. This is expected to reduce the error of the $U_yR_x/R_{m,y}R_x/R_m$-S/AXS cases in Figs. 11–13 near the middle of the plots where no interpolation points were added.

The use of beyond-nominal condition cross sections which are not environmentally corrected increases the neutron power ratio error, since the flux ratio is not correct. This was tested as well through equation:

$$\Sigma^{side}_{x,BNC} = \Sigma^{side}_{x,NC} + (\Sigma^{ass.}_{x,BNC} - \Sigma^{ass.}_{x,NC}). \quad (25)$$

The change in cross section calculated by Eq. (25) between beyond-nominal and nominal conditions had errors up to 81%. In addition, under some conditions, max channel specific neutron power errors were calculated to be greater than 6% and RMS neutron power errors $\sim 1\%$; thus this method is not recommended. Rather, the strip calculation method discussed in Section 2.5.4 is recommended for side cell nominal and beyond-nominal condition cross section preperation.

4.3. Conservativeness

It is important in safety analysis to consider which calculations result in more conservative predictions. For BNC channels in Figs. 8–13, a more positive error translates into a more conservative result. For example in Fig. 13, the J1 AXS and SXS lines have similar errors in magnitude, however, AXS lines have negatve error and SXS lines have positive error. The positive SXS errors indicate a neutron power increase is over predicted, thus more conservative. Meanwhile, a true neutron power decrease is calculated to have a smaller power decrease, thus more conservative.

For inner core channels with BNCs, UDF and R_mDF results are similar and the most conservative, while ADFs are the least conservative. For outer core channels, calculations which include SXS are more conservative than those without (in most cases presented in this paper).

4.4. Transport cross section libraries

The use of a 56 g library reduces accuracy of transport results, and perhaps beyond-nominal condition cases are not predicted with high fidelity. This was addressed in Table 2, however, note the difference in transport reactivity between the 252 g and 56 g was -8.34 mk. Thus it's not inconceivable that beyond-nominal conditions were improperly predicted. However, the authors are confident that the trends presented in this paper are correct.

Use of a more accurate cross section library can be implemented through a transport code that's not limited by the number of meshes, total number of isotopes, or number of energy groups. It is suggested that a follow-up study be conducted with the use of SERPENT, which has been used for large multi cell homogenization studies (i.e., Shen, 2012), however DFs and side cell cross sections were not considered.

4.5. Nodal meshing and coarse energy groups

The effects of different nodal meshing, and the effect of adding coarse energy groups, on diffusion neutron power errors has previously been assessed (Smith, 1986; Smith, 1980; Shen, 2012; Lee et al., 2015). These techniques generally improve neutron power and reactivity predictions dependant upon on fuel cell geometry and reactor type. However, the use of discontinuity factors is not limited to any mesh size or number of energy groups. Thus, when techniques developed in this work are applied to a finer-meshes or finer-energy group structures, improvements are expected, however, the magnitude of improvements cannot be estimated.

4.6. Applicability to corner cells

Although no simulations were performed in this work regarding corner cells[3] (i.e. a fuel cell surrounded by two reflector cells and two fuel cells), they are of importance. Corner cells represent $\sim 6\%$

[3] e.g. cells G1, E2, C3, B5 and A7 in Fig. 3.

Table 12
Improvements from R_mDF-AXS in the inner core, and $U_yR_x/R_{m,y}R_x/R_m$-S/AXS in the outer core.

Discontinuity Factor			Cross section	$\Delta\rho$	P_{RMS}	$P^{Channel}_{Max}$	P^{Model}_{Max}
Refl.	Side	Inner	Side/Inner	(mk)	(% Err.)	(% Err.)	
–	–	U	A	0.9	1.0	2.9	2.9
–	–	A	A	0.8	0.9	2.8	2.8
U	U	U	A/A	0.3	2.9	6.7	6.7
U	U	A	A/A	0.3	2.9	6.5	6.5
U	U	U	Side/A	2.6	2.8	4.6	(−1.7)
U	U	A	Side/A	2.6	2.5	3.8	(−1.8)

of the cells (20/336) in a horizontal cross section of the Canadian SCWR core. On the other hand, side cells, which were researched extensively in this work represent ∼12% of the cells (40/336) in the SCWR core. According to Salaun and Novog (2016), corner cells have an average power that is ∼7% high than those of side cells, when control devices and reactivity hold down strategies are implemented. Thus, side cells constitute 1.87× more total power worth than corner cells. Unfortunately, corner cells are more difficult to accurately homogenize, since they are affected on two sides by reflector properties. Side cells on the other hand are bordered only by one reflector cell, and three fuel cells.

An argument can be made that the cross sections will be shift, in the appropriate direction, towards the reference cross sections of corner cells if the 1D strip method presented herein is used, however, this strategy is not recommended. Based on lessons learned within this work, a 2D multi cell that includes a number of fuel and reflector cells in the appropriate configuration, would be ideal for this task. To support this, a similar strategy was used in Hummel and Novog (2016) where a 4 × 4 multi cell, with 2x2 fuel cells in the bottom right corner and reflect cells to the north, west, and north-west. Another study (Salaun et al., 2014) shows the impact of the reflector on corner cells compared to the infinite lattice. The study presents cross section discrepancies which show the corner cell 8-group cross sections are more similar to side cell cross sections, produced in a 1D strip, than assembly cross sections, which further support this study.

With these findings in mind, the 1D strip method which was developed in this work for side cells, is not expected to produce accurate channel powers in corner cells, however, is expected to be an improvement over assembly cross sections. However, to properly homogenize corner cells they should be treated as a special case and homogenized in an appropriate multi cell.

5. Conclusion

This work presented a number of practical methods that can be readily applied to reactor physics evaluations which use transport and diffusion codes. The use of mean reference discontinuity factors has been demonstrated and improvements over traditional methods are shown in Table 12, in addition to side cell cross sections, under nominal conditions.

In the inner core, AXS-R_mDF beyond-nominal condition cases performed more or less the same as AXS-UDF cases (burnup dependent); however, they consistently performed better than AXS-ADF. However, in terms of global errors, performed consistently better than both AXS-UDF and AXS-ADF.

In the outer core beyond-nominal condition cases, the suggested method of $U_yR_x/R_{m,y}R_x/R_m$-S/AXS performed better than conventional methods by 0.5% to 3.5%. The global improvements were significant as well and are listed in Table 12.

The method proposed in this work, when applied to PT-SCWR simulations, with the use of mean reference discontinuity factors, and side cell cross sections offers a major improvement over conventional methods under nominal conditions, and significant improvements over conventional methods in beyond-nominal condition channels.

Acknowledgement

The author (J.S.) thanks Frédéric Salaun for his endless suggestions and sincere interest in this research. He also extends his appreciation to Rian Prinsloo and Francois van Heerden for their expertise on the subject and valuable discussions. The author is also extremely grateful to David Novog for his many helpful recommendations after reviewing this document. The work described in this paper was supported in part by the National Science and Engineering Research Council (NSERC) of Canada, under Grant No. 125519967 and by the NSERC/NRCan/AECL Generation IV Energy Technologies Program.

References

Boyle, K., Brady, D., Guzonas, D., Khartabil, H., Leung, L., Lo, J., et al. 2009. Canada's Generation-IV National Program – Overview. In: 4th International Symposium on Supercritical Water-Cooled Reactors, Heidelberg, Germany, 8–11 March 2009.

Downar, T., Xu, Y., Seker, V., 2012. Theory Manual for the PARCS Kinectics Core Simulator Module, January 2012.

Hummel, D., Novog, D., 2016. Coupled 3D neutron kinetics and thermalhydraulic characteristics of the Canadian supercritical water reactor. Nucl. Eng. Des. 298, 78–89. http://dx.doi.org/10.1016/j.nucengdes.2015.12.008.

Jessee, M., DeHart, M., 2016. NEWT: A New Transport Algorithm for Two-Dimensional Discrete-Ordinates Analysis in Non-Orthogonal Geometries, tech. Rep. ORNL/TM-2005/39 Version 6.2, April 2016.

Jessee, M., Wiarda, D., Clarno, K.T., Mertyurek, U., Bekar, K., 2016. TRITON: A Multipurpose Transport, Depletion, and Sensitivity and Uncertainty Analysis Module, tech. Rep. ORNL/TM-2005/39 Version 6.2, April 2016.

Kim, H., Cho, N., 1993. Global/local iterative methods for equivalent diffusion theory parameters in nodal calculation. Ann. Nucl. Energy 20 (11), 767–783. http://dx.doi.org/10.1016/0306-4549(93)90095-7.

Koebke, K., 1978. A new approach to homogenization and group condensation. In: Specialists' Meeting on Homogenization Methods in Reactor Physics, Lugano, Switzerland. pp. 303–322.

Lee, D., Kozlowski, T., Downar, T.J., 2015. Multi-group SP3 approximation for simulation of a three-dimensional PWR rod ejection accident. Ann. Nucl. Energy 77, 94–100. http://dx.doi.org/10.1016/j.anucene.2014.10.019.

Macdonald, M., Colton, A., Pencer, J., 2015. Power flattening and reactivity suppression strategies for the canadian supercritical water reactor concept. In: 35th Annual Conference of the Canadian Nuclear Society, Saint John, NB, Canada, 1–14, 2015.

Moghrabi, A., Novog, D.R., 2016. Investigation of reactor physics phenomena in the canadian pressure tube supercritical-water reactor. Can. Nucl. Lab. Nucl. Rev. 5 (2), 253–268. http://dx.doi.org/10.12943/CNR.2016.00031.

Pencer, J., Bromley, B., Nava-Dominquez, A., 2012. Fuel Channel Assembly and Fuel Bundle for a Nuclear Reactor, canadian Patent CA 2881784 A1, June 2012.

Pencer, J., Colton, A., Watts, D., Blomeley, L., Wang, X., Anghel, V., Yue, S., 2013. Core neutronics for the Canadian SCWR conceptual design. In: The 6th International Symposium on Supercritical Water-Cooled Reactors, Shenzhen, Guangdong, China. pp. 1–15.

Petrie, B.T., Rearden, L.M., 2016. MCDANCOFF Data Guide, tech. Rep. ORNL/TM-2005/39 Version 6.2, April 2016.

Rahnema, F., Nichita, E., 1997. Leakage corrected spatial (assembly) homogenization technique. Ann. Nucl. Energy 24 (6), 477–488. http://dx.doi.org/10.1016/s0306-4549(96)00084-9.

Salaun, F., Novog, D., 2016. Spatial and bulk reactivity systems design and optimization for the Canadian supercritical water reactor. CNL Nucl. Rev. 5 (2), 285–298. http://dx.doi.org/10.12943/CNR.2016.00037.

Salaun, F., Hummel, D.W., Novog, D.R., 2014. The impact of the radial reflector on the 8-group cell-averaged cross-sections for the SCWR 62-element lattice cell. In: 2014 Canada-China Conference on Advanced Reactor Development, Niagra Falls, ON, Canada. pp. 1–15.

Sharpe, J.R., Salaun, F., Hummel, D.W., Moghrabi, A., Nowak, M., Pencer, J., Novog, D. R., Buijs, A., 2015. A benchmark comparison of the canadian supercritical water-cooled reactor (SCWR) 64-element fuel lattice cell parameters using various computer codes. In: 35th Annual Conference of the Canadian Nuclear Society, Saint John, NB, Canada. pp. 1–20.

Sharpe, J.R., Buijs, A., Pencer, J., 2016. Methodology to design simulated irradiated fuel by maximizing similarity (ck, E, G). J. Nucl. Eng. Radiat. Sci. 2 (2), 1–7. http://dx.doi.org/10.1115/1.4031074.

Sharpe, J., Atfield, J., Chow, J., Yaraskavitch, L., Buijs, A., 2016. Sensitivity analysis of ZED-2 experiments using (Pu, Th)O2 fuel bundles to assess their applicability to the SCWR conceptual design. CNL Nucl. Rev. 5 (2), 299–308. http://dx.doi.org/10.12943/CNR.2016.00039.

Shen, W., 2012. Assessment of the traditional neutron-diffusion core-analysis method for the analysis of the Super Critical Water Reactor. Ann. Nucl. Energy 45, 1–7. http://dx.doi.org/10.1016/j.anucene.2012.02.009.

Smith, K., 1980. Spatial Homogenization Methods for Light Water Reactor Analysis (Ph.D. thesis). Massachusetts Institute of Technology.

Smith, K., 1986. Assembly homogenization techniques for light water reactor analysis. Prog. Nucl. Energy 17 (3), 303–335. http://dx.doi.org/10.1016/0149-1970(86)90035-1.

Stacey, W.M., 2007. Nuclear Reactor Physics. Wiley-VCH Verlag GmbH & Co. KGaA, Weinheim, Germany, ISBN 978-3-527-40679-1. http://dx.doi.org/10.1002/9783527611041.

Usalp, E., Nichita, E., 2015. Leakage-corrected discontinuity factors for PHWR lattices. In: 7th International Conference on Modelling and simulation in Nuclear Science and Engineering, Oshawa, Ontario, Canada. pp. 1–8.

Williams, M., Wiarda, D., Celik, C., Kim, K., Dunn, M., Rearden, B., 2016. Scale Cross Section Libraries, tech. Rep. ORNL/TM-2005/39 Version 6.2, April 2016.

Yetisir, M., Gaudet, M., Rhodes, D., Guzonas, D., Hamilton, H., Haque, Z., Pencer, J., Sartipi, A., 2014. Reactor core and plant design concepts of the canadian supercritical water-cooled reactor. In: Canada-China Conference on Advanced Reactor Development. 1–14, 2014.

Chapter 6

Discussion and Conclusion

This thesis describes three unique contributions to the field of reactor physics research, specifically related to quantification and reduction of uncertainty and error. The work offers a number of advancements that aid in the research, development, and analysis, of nuclear reactors and critical assemblies. Although the work presented herein was specifically applied in the SCWR context, the methodologies are also applicable to the general progression of reactor physics as a whole and are not limited to any single type of reactor.

The methodologies described in Chapters 3 and 5 contribute to both the experimental and theoretical frameworks of reactor physics analysis. The results in Chapter 4 used experimental results to show how a test reactor can be made relevant to the development of a new reactor design through simulation. This supports the design of the new reactor as well as the licence case that needs to be made for it.

Chapter 3 presents a methodology [23] which enables researchers to manufacture a safe-to-handle fuel bundle that neutronically mimics the behavior of an irradiated fuel bundle. Again, although the novel methodology was specifically developed in the SCWR setting, it can immediately be extended to any type of critical assembly. Researchers can now fabricate fuel bundles and assemblies that mimic irradiated fuel, based on a consistent

method, and test them in experimental facilities like ZED-2. The experimental results can be used to demonstrate, to the regulator, that the applicant's simulation codes can correctly predict neutronic behavior at various points throughout a burnup cycle.

From a public safety perspective, if additional tests and proofs are required as a part of the standard analysis process, such as those presented in Chapter 3, a more robust review and licensing process is achieved. Moreover, if proof of safe operation and accurate prediction is provided in advance to building a reactor, an economical safety net is added.

An analysis was done to determine how much dysprosia and zirconia need to be added to a fresh fuel for it to have the same properties as irradiated fuel. The former is called the simulated fuel (which may be manufactured and tested), and the latter is the irradiated fuel (which cannot be produced nor handled because of its activity). Zirconia and dysprosia are added because they are chemically and radioactively benign neutron absorbers. Three different similarity metrics, c_k, E and G, were employed to quantify the neutronic similarity of the two fuels. The concentrations of dysprosia and zirconia were optimized in order to maximize the similarity metrics, resulting in $c_k = 0.967$, $E = 0.992$, and $G = 0.891$. These high similarity values indicate that simulated irradiated fuel can be produced and used in experiments, and that those experiments can contribute to reducing the uncertainties of future simulation predictions through a nuclear data adjustment.

The importance of understanding uncertainties to safe reactor operation was discussed in Section 1.2.2. Moreover, today's reactors are developed through simulation to meet certain design criteria, such as exit burnup targets, core-wide power distributions, fuel cell flux profiles, and reactivity feedback coefficients. For added protection, beyond operating basis and beyond design basis scenarios must also be anticipated. Most importantly, simulation predictions have an associated uncertainty which must be considered throughout the design of a reactor. Finally, in order to convince the regulator the reactor is safe, a knowledge of simulation prediction uncertainties is required.

Chapter 4 presented the applicability of the ZED-2 reactor loaded with (Pu,Th)O_2

fuel to an SCWR nuclear data adjustment [24]. The results of this study show that ZED-2 with plutonia in thoria fuel can contribute to a nuclear data adjustment and bias determination. More specifically, it was found that certain isotopes provide a very high similarity and coverage of ZED-2 with the SCWR. If experiments, or nuclear data components (i.e., isotopes, reactions, energy groups) of an experiment, have a high similarity to the reactor to be licensed, and simulation predictions match experiments to within experimental uncertainty, the regulator gains more confidence that simulations will correctly predict reactor behaviour.

The similarity metrics that were discussed above indicate how neutronically similar a single experiment's simulation is to an application's simulation (e.g., SCWR). The nuclear data adjustment procedure allows the use of many experiments in its calculation, as additional experimental data produces added constraints that the GLLS procedure must adhere to. The completeness parameter R is a measure of how many sensitivities are covered by a set of experiments as a whole. From the set of 39 experiments analyzed in [24] a value of $R = 0.24$ was found, which suggests the experimental set is not sufficient on its own to conduct a nuclear data adjustment. However, the work also found that many important sensitivities were covered due to the physical similarities of the ZED-2 reactor partially driven by (Pu,Th)O_2 fuel, and the SCWR.

The neutron diffusion method is applied in the final phase of reactor physics analysis where core-wide coupled neutronics and thermal-hydraulics simulations are executed. At this stage, very realistic time-dependant simulations can be performed. The simulations can range from regular operation, power maneuvers, extreme accident scenarios such as ejection of reactivity devices and loss-of-coolant accidents, to inlet or outlet plenum thermal-hydraulic changes which take place over a time scale of seconds up to weeks. This final portion of the analysis uses a combination of outputs from earlier stages, notably the homogenized parameters, which are the basis for diffusion calculations. Thus, in addition to approximations of its own, the diffusion method uses uncertain parameters from

previous analysis steps, and therefore has potentially the highest associated uncertainty.

Chapter 5 presentes and demonstrates a methodology that allows an improved prediction of fuel channel powers through the use of discontinuity factors [5] and reflector-adjacent fuel cell homogenization. an improved prediction of fuel channel powers offers two main advantages:

1. Economical - if channel power errors calculated by [5] are consistently smaller than those calculated by conventional methods, then the diffusion code can better predict reality, and the regulator may permit a smaller power operating margin. This allows the reactor to be operated at a higher power since channel powers are predicted to a higher degree of confidence.

2. Safety - if the average channel power error is reduced, the operator has, on average, a better understanding of the power shape within the core. In addition, if accidents are simulated, more accurate diffusion calculations result in more accurate power distributions which in turn affect thermal-hydraulic properties that amplify or weaken power transients.

The new type of discontinuity factor is generated through a large multi-cell neutron transport calculation, which calculates interface-averaged currents and fluxes, along with node-averaged fluxes. These values can be later used to generate mean reference discontinuity factors that account for node-to-node flux discontinuities as a function of burnup as well as the difference in burnup between nodes.

Additionally, [5] demonstrated the effect of using specially homogenized reflector-adjacent fuel cells. These fuel cells were homogenized in an approximate environment consisting of four reflector cells and four identical fuel cells. The technique, along with the introduction of mean reference discontinuity factors yielded significant improvements over conventional homogenization and diffusion solution techniques as listed in Table 6.1.

Unfortunately, the use of the diffusion method introduces significant channel power

Table 6.1: Simulated improvements in channel power predictions over conventional methods in the inner core and outer core [5] through the use of mean reference discontinuity factors and strip reflector-adjacent fuel cell homogenization.

Core Region	Discontinuity Factor			Cross section	$\Delta\rho$	P_{RMS}	$P_{\text{Max}}^{\text{Channel}}$	$P_{\text{Max}}^{\text{Model}}$
	Refl.	Side	Inner	Side/Inner	(mk)	(% Err.)	(% Err.)	(% Err.)
Inner	-	-	U	A	0.9	1.0	2.9	2.9
	-	-	A	A	0.8	0.9	2.8	2.8
Outer	U	U	U	A/A	0.3	2.9	6.7	6.7
	U	U	A	A/A	0.3	2.9	6.5	6.5
	U	U	U	Side/A	2.6	2.8	4.6	(-1.7)
	U	U	A	Side/A	2.6	2.5	3.8	(-1.8)

U, A, Side: Unitary, Assembly, and Side discontinuity factors or cross sections.

errors when compared to a reference, because of its inherently approximate nature. Until sweeping changes come to standard analysis techniques, any improvement is welcomed. Rather than introducing an entirely new calculation technique, the work described in [5] built on existing understanding of the proven diffusion method, and introduced a formalism which can easily be used by any research group with minimal to no code alterations.

In conclusion, this thesis presents two methodologies [5, 23] that significantly advance the experimental and theoretical framework for reactor physics development, specifically through the reduction of uncertainties and errors. In addition, another paper was contributed which assesses the applicability of the Canadian ZED-2 experimental critical assembly to reactor development [24]. This paper supports the continued valuable contribution of ZED-2 to nuclear science.

Bibliography

[1] M. Yetisir, M. Gaudet, D. Rhodes, D. Guzonas, H. Hamilton, Z. Haque, J. Pencer, and A. Sartipi, "Reactor core and plant design concepts of the Canadian supercritical water-cooled reactor," in *Canada-China Conf. Advanced Reactor Development*, April 2014.

[2] J. Sharpe, A. Buijs, and J. Pencer, "Methodology to design simulated irradiated fuel by maximizing similarity (c_k, E, G)," *ASME J. Nucl. Eng. and Rad. Sci.*, vol. 2, no. 2, April 2016.

[3] Oak Ridge National Laboratory, "SCALE 6.1: A comprehensive modeling and simulation suite for nuclear safety analysis and design," 2011.

[4] Data used from plots produced using the Online Service retrieval code package written by C. L. Dunford, National Nuclear Data Center, Brookhaven National Laboratory.

[5] J. Sharpe and A. Buijs, "Practical environment-corrected discontinuity factors and homogenized parameters for improved PT-SCWR diffusion solutions," *Ann. Nucl. Energy*, 2017, article submitted for publication April.

[6] T. Downar, Y. Xu, and V. Seker, "Theory manual for the parcs kinectics core simulator module," January 2012.

[7] W. M. Stacey, *Nuclear reactor physics*. Weinheim, Germany: Wiley-VCH Verlag GmbH & Co. KGaA, February 2007.

[8] OECD, *International criticality safety benchmark evaluation project*, Nuclear Energy Agency, 2016.

[9] OECD, *Database for the international criticality safety benchmark evaluation project (DICE)*, Nuclear Energy Agency, 2001.

[10] Generation IV International Forum, "Charter of the Generation IV International Forum," https://www.gen-4.org/gif/jcms/c_40343/extended-gif-charter/ (accessed: May 12, 2015), 2014.

[11] F. Salaun and D. R. Novog, "Spatial and bulk reactivity systems design and optimization for the Canadian supercritical water reactor," *CNL Nucl. Rev.*, vol. 5, no. 2, pp. 285–298, December 2016.

[12] M. Yetisir, W. Diamond, L. Leung, D. Martin, R. Duffey *et al.*, "Conceptual mechanical design for a pressure-tube type supercritical water-cooled reactor," in *5th Int. Symp. Supercritical Water-Cooled Reactors*, Vancouver, BC, Canada, March 2011.

[13] J. Pencer, B. Bromley, and A. Nava-Dominquez, "Fuel channel assembly and fuel bundle for a nuclear reactor," 13 June 2012, canadian Patent CA 2881784 A1.

[14] C. Chow and H. Khartabil, "Conceptual fuel channel designs for CANDU-SCWR," *Nucl. Eng. Tech.*, vol. 40, no. 4, pp. 139–146, 2008.

[15] W. Shen, "Assessment of the traditional neutron-diffusion core-analysis method for the analysis of the super critical water reactor," *Ann. Nucl. Energy*, vol. 45, pp. 1–7, July 2012.

[16] G. Harrisson and G. Marleau, "Simulation strategy for the evaluation of neutronic properties of a Canadian SCWR fuel channel," *Sci. Tech. Nucl. Installations*, vol. 2013, 2013.

[17] J. Pencer and L. Blomeley, "A preliminary SCWR 2D lattice-level benchmark comparison of WIMS-AECL and MCNP," Atomic Energy of Canada Limited, Tech. Rep., 2013.

[18] K. Carisse, "Leakage-corrected discontinuity factors for a second-generation Th-Pu pressure-tube SCWR," Ph.D. dissertation, University of Ontario Institute of Technology, 2014.

[19] D. W. Hummel, D. R. Novog, S. E. Langton, A. Buijs, and M. R. Ball, "Description and preliminary results of a two-dimensional lattice physics code benchmark for the Canadian pressure tube supercritical water-cooled reactor (PT-SCWR)," in *6th Int. Symp. Supercritical Water-Cooled Reactors*, Shenzhen, China, 2013.

[20] S. Langton, "Experiment design for (Th,Pu)O_2 power reactors," Ph.D. dissertation, McMaster University, 2013.

[21] J. Pencer, A. Colton, D. Watts, L. Blomeley, X. Wang, V. Anghel, and S. Yue, "Core neutronics for the Canadian SCWR conceptual design," in *6th Int. Symp. Supercritical Water-Cooled Reactors*, Shenzen, China, 2013.

[22] A. Ahmad, L. Cao, and H. Wu, "Coupled analysis and improvements for Canadian-SCWR core design," *Nucl. Eng. and Design*, vol. 268, pp. 104–112, March 2014.

[23] J. Sharpe, A. Buijs, and J. Pencer, "Methodology to design simulated irradiated fuel by maximizing similarity (c_k, E, G)," in *7th Int. Symp. Supercritical Water-Cooled Reactors*, Helsinki, Finland, 2015.

[24] J. Sharpe, J. Atfield, J. Chow, L. Yaraskavitch, and A. Buijs, "Sensitivity analysis of ZED-2 experiments using (Pu,Th)O_2 fuel bundles to assess their applicability to the SCWR conceptual design," *CNL Nucl. Rev.*, vol. 5, no. 2, pp. 299–308, 2016.

[25] A. Colton and J. Pencer, "A solid moderator physics assessment for the Canadian SCWR," *CNL Nucl. Rev.*, vol. 5, no. 2, 2016.

[26] M. Mcdonald, A. Colton, and J. Pencer, "Power flattening and reactivity suppression strategies for the Canadian supercritical water reactor concept," in *35th Annu. Conf. of the Canadian Nucl. Society*, Saint John, NB, Canada, 2015.

[27] F. Salaun, D. Hummel, and D. Novog, "Preliminary study on the use of burnable neutron absorbers in the pressure tube type super critical water-cooled reactor," in *19th Annu. Pacific Basin Nucl. Conf.*, Vancouver, BC, Canada, 2014.

[28] H. Raouafi and G. Marleau, "Monte Carlo simulation of inclined reactivity control rod and boron poisoning for the Canadian-SCWR supercell," *ASME J. Nucl. Eng. and Rad. Sci.*, vol. 2, no. 2, 2016.

[29] H. Raouafi, "Simulation de mécanismes de contrôle de la réactivité du réacteur SCWR-canadien en utilisant les codes DRAGON-5 et DONJON-3," PhD Thesis, École Polytechnique de Montréal, Montreal, QC, April 2017.

[30] F. Salaun, J. Sharpe, D. Hummel, A. Buijs, and D. Novog, "Optimization of the PT-SCWR control blade sequence using PARCS and DAKOTA," in *7th Int. Symp. on Supercritical Water-Cooled Reactors*, no. March, Helsinki, Finland, 2015.

[31] World Nuclear Association, "Uranium Enrichment," http://www.world-nuclear.org/information-library/nuclear-fuel-cycle/conversion-enrichment-and-fabrication/uranium-enrichment.aspx, Accessed: May 29, 2017.

[32] S. Langton, A. Buijs, and J. Pencer, "Nuclear data sensitivity and uncertainty for the Canadian supercritical water-cooled reactor II: Full core analysis," *Ann. Nucl. Energy*, vol. 75, pp. 635–644, January 2015.

[33] L. Blomeley, J. Pencer, B. Hyland, and F. Adams, "Nuclear data sensitivity and uncertainty for the Canadian supercritical water-cooled reactor," *Ann. Nucl. Energy*, vol. 63, pp. 587–593, January 2014.

[34] J. Sharpe, F. Salaun, D. Hummel, A. Moghrabi, M. Nowak, J. Pencer, D. Novog, and A. Buijs, "A benchmark comparison of the Canadian supercritical water-cooled reactor (SCWR) 64-element fuel lattice cell parameters using various computer codes," in *35th Annu. Conf. of the Canadian Nuclear Society*, Saint John, NB, Canada, 2015.

[35] M. Williams, B. Broadhead, M. Jessee, J. Wagschal, and R. Lefebvre, *TSURFER: An adjustment code to determine biases and uncertainties in nuclear systems responses by consolidating differential data and benchmark integral experiments*, Oak Ridge National Laboratory, June 2011, Tech. Rep. ORNL/TM-2005/39 Version 6.1 Sect. M21.

[36] B. Rearden *et al.*, *SAMS: Sensitivity analysis module for SCALE*, Oak Ridge National Laboratory, June 2011, Tech. Rep. ORNL/TM-2005/39 Version 6.1 Sect. F22.

[37] C. Weisbin, J. Marable, J. Lucius, E. Oblow, F. Mynatt, R. Peelle, and F. Perey, "Application of FORSS sensitivity and uncertainty methodology to fast reactor benchmark analysis," Oak Ridge National Laboratory, Oak Ridge, TN, USA, Tech. Rep., December 1976.

[38] M. Williams, B. Broadhead, and C. Parks, "Eigenvalue sensitivity theory for resonance-shielded cross sections," *Nucl. Sci. Eng.*, vol. 138, pp. 177–191, 2001.

[39] M. Salvatores *et al.*, "Methods and issues for the combined use of integral experiments and covariance data. NEA/NSC/WPEC/DOC(2013)445," Nuclear Energy Agency, Tech. Rep. December, 2013.

[40] B. Rearden and M. Jessee, *TSUNAMI utility modules*, Oak Ridge National Laboratory, June 2011, Tech. Rep. ORNL/TM-2005/39 Version 6.1 Sect. M18.

[41] S. Golouglu, C. Hopper, and B. Rearden, "Extended interpretation of sensitivity data for benchmark areas of applicability," *Trans. Am. Nuc. Soc.*, vol. 88, pp. 77–79, 2003.

[42] COG, "CANDU," http://www.candu.org/candu_reactors.html, Accessed: June 3, 2017.

[43] M. Dehart, "A discrete ordinates approximation to the neutron transport equation applied to generalized geometries," Ph.D. dissertation, Texas A&M, 1992.

[44] K. Smith, "Assembly homogenization techniques for light water reactor analysis," *Prog. Nucl. Energy*, vol. 17, no. 3, pp. 303–335, 1986.

[45] K. Koebke, "A new approach to homogenization and group condensation," in *Specialists' Meeting on Homogenization Methods in Reactor Physics*. Lugano, Switzerland: International Atomic Energy Agency, 1978, pp. 303–322.

[46] L. Petrie, N. Landers, D. Hollenbach, B. Rearden, M. Dunn, and S. Goluoglu, *KENO V.a: An improved Monte Carlo criticality program*, Oak Ridge National Laboratory, June 2011, Tech. Rep. ORNL/TM-2005/39 Version 6.1 Sect. F11.

[47] X-5 Monte Carlo Team, "MCNP - Version 5, Vol. I: Overview and theory," Los Alamos National Laboratories, 2003, Tech. Rep. LA-UR-03-1987.

[48] A. Hebert, *Applied reactor physics*. Presses Internationales Polytechnique, 2009.

[49] J. Leppänen, "The SERPENT Monte Carlo code: Status, development and applications in 2013," *Ann. Nucl. Energy*, vol. 82, pp. 142–150, 2015.

[50] J. Stewart, *Calculus early trancendentals*, 5th ed. Thomson, Brooks/Cole, 2003.

[51] M. Jessee and M. DeHart, "NEWT: A new transport algorithm for two-dimensional discrete-ordinates analysis in non-orthogonal geometries," April 2016, Tech. Rep. ORNL/TM-2005/39 Version 6.2.

[52] B. Foad and T. Takeda, "Importance of self-shielding for improving sensitivity coefficients in light water nuclear reactors," *Ann. Nucl. Energy*, vol. 63, pp. 417–426, January 2014.

[53] H. Choi and G. Roh, "Benchmarking MCNP and WIMS/RFSP against measurement data - I: Deuterium critical assembly," *Nucl. Sci. Eng.*, vol. 146, no. 2, pp. 188–199, February 2004.

[54] M. Nagy, M. Aly, F. Gaber, and M. Dorrah, "Neutronic behavior of reactor moderated by mixtures of light and heavy waters at different ratios," *Ann. Nucl. Energy*, vol. 63, pp. 548–555, January 2014.

[55] K. Shiba, K. Iijima, A. Muramatsu, and N. Aihara, "Heavy-water critical experiment for FUGEN (I) void reactivity in plutonium lattice," in *ANS 21st Annu. Meeting*, 1975.

[56] G. Aliberti *et al.*, "Nuclear data sensitivity, uncertainty and target accuracy assessment for future nuclear systems," *Ann. Nucl. Energy*, vol. 33, no. 8, pp. 700–733, May 2006.

[57] OECD, *International handbook of evaluated reactor physics benchmark experiments*, Nuclear Energy Agency, March 2011.

[58] Q. Ao, "Uncertainty analysis in Monte Carlo criticality computations," *Nucl. Eng. Des.*, vol. 241, no. 12, pp. 4697–4703, December 2011.

[59] M. Williams, D. Wiarda, G. Arbanas, and B. Broadhead, *SCALE Nuclear Data Covariance Library*, Oak Ridge National Laboratory, June 2011, Tech. Rep. ORNL/TM-2005/39 Version 6.1 Sect. M19.

[60] A. Pazy, G. Rakavy, I. Reiss, J. Wagschal, A. Ya'ari, and Y. Yeivin, "The role of integral data in neutron cross section evaluation," *Nucl. Sci. Eng.*, vol. 55, pp. 280–295, November 1974.

[61] W. Poenitz and P. Collins, "Utilization of experimental integral data for the adjustment and uncertainty evaluation of reactor design quantities, applications of critical experiments and operating data to core design via formal methods of cross section data adjustment," Nuclear Energy Agency - Computational Reactor Physics, Jackson Hole, NY, NEACRP-L-307, September 1988.

[62] R. Maerker, J. Wagschal, and B. Broadhead, "Development and demonstration of an advanced methodology for LWR dosimetry applications," Electric Power Research Institute, EPRI NP-2188, December 1981.